國 立 交 通 大 學

光電工程研究所

博 士 論 文

飛秒雷射退火:
再結晶、控制佈植活化深度及薄膜電晶體製作的新技術

Femtosecond laser annealing:
a novel approach for recrystallization, dopant profile engineering and fabrication of Thin Film Transistors

研究生：王怡超

指導教授：潘犀靈 教授

中 華 民 國 九 十 六 年 十 二 月

飛秒雷射退火:
再結晶、控制佈植活化深度及薄膜電晶體製作的新技術

Femtosecond laser annealing:
a novel approach for recrystallization, dopant profile engineering and fabrication of Thin Film Transistors

研 究 生：王怡超　　Student：Yi-Chao Wang

指導教授：潘犀靈 教授　　Advisor：Prof. Ci-Ling Pan

國 立 交 通 大 學

光 電 工 程 研 究 所

博 士 論 文

A Thesis

Submitted to Department of Photonics &

Institute of Electro-Optical Engineering

College of Electrical Engineering

National Chiao Tung University

In partial Fulfillment of the Requirements

for the Degree of

Doctor of Philosophy

in

Electro-Optical Engineering

December 2007

Hsinchu, Taiwan, Republic of China

中華民國九十六年十二月

飛秒雷射退火:
再結晶、控制佈植活化深度及薄膜電晶體製作的新技術

學生：王怡超　　指導教授：潘犀靈 教授

國立交通大學光電工程研究所 博士班

摘　　要

本論文之主要內容可分為三個部分。首先是利用飛秒雷射進行非晶矽退火的研究並將此一新技術應用於複晶矽薄膜電晶體(TFT)的製作，其次是利用飛秒雷射在矽及鍺基板上進行超淺介面佈植活化的研究，最後則是利用兆赫波時域解析技術研究飛秒雷射退火非晶矽並藉此辨別退火後複晶矽的結晶特性。

傳統的非晶矽退火主要是利用爐管及準分子雷射進行。然而爐管退火必須在 550 ℃進行，因而限制其在玻璃基板上的應用。非晶矽在一般準分子雷射波段(λ=248-308 nm)的線性吸收係數雖然大約是近紅外飛秒雷射波段(λ=800 nm)的兩千倍，但是近紅外飛秒雷射退火所需要的能量密度卻更低(~50 mJ/cm^2)。研究中發現照射適當數量的飛秒雷射脈衝可以得到最大的晶粒尺寸約 800 nm，且退火樣品的表面平整度極佳(RMS roughness <10 nm)。將飛秒雷射退火複晶矽應用於TFT製作可以證實此一技術實際應用的可能性。飛秒雷射退火在小長寬比(2μm/2μm)TFT可得到最佳的載子遷移率約 160 cm^2/Vs，同時藉由field-effect-conductance的方式分析元件的缺陷密度。這兩項與準分子雷射退火複晶矽TFT極為接近的關鍵特性皆說明了飛秒雷射退火未來應用的潛力。

為了克服元件尺寸減小時造成的短通道效應，超淺介面佈植活

i

化在高速元件例如金氧半場效電晶體(MOSFET)的製作上極為重要。在快速升溫退火及準分子雷射活化技術逐漸成熟的同時，準分子雷射的熱致熔融與快速升溫退火活化在硼或磷原子活化時仍然會造成約數十奈米的擴散。藉由超短脈衝雷射活化所造成的非熱熔融，活化過程中僅造成佈植原子極微小的擴散(~ 10 nm)。不僅可將片電阻降低到100-400 Ω/□，且佈植原子的活化效率約可達到 28-35%，同時熱致熔融所常見的佈植原子散逸也得到避免。超短脈衝雷射活化應用在鍺基板上亦可得到極佳的活化效果。

複晶矽的晶粒尺寸是製作 TFT 時的重要參數，因為其與 TFT 載子遷移率有極大的關聯。但是觀察晶粒尺寸屬於破壞性的量測，因為必須先將退火後的複晶矽作蝕刻再以電子顯微鏡觀察晶粒。利用光激發-兆赫波探測的方式可以在不損壞樣品的前提之下觀察不同晶粒尺寸樣品的折射率以及導電率隨時間的變化，並藉由兆赫波時域解析的量測得到其光激載子的遷移率。

Femtosecond laser annealing:
a novel approach for recrystallization, dopant profile engineering and fabrication of Thin Film Transistors

Student：Yi-Chao Wang Advisors：Dr. Ci-Ling Pan

Institute of Electro-Optical Engineering
National Chiao Tung University

ABSTRACT

The main topics of this thesis can be divided into three categories; (1) near-infrared femtosecond laser-induced crystallization of amorphous silicon and the performance of thin film transistors (TFTs) annealed by this technique; (2) dopant profile engineering by near–infrared femtosecond laser activation (FLA) on Si and Ge substrates; (3) time-resloved THz spectroscopy of femtosecond-laser-annealed amorphous silicon for grain quality diagnosis.

Polycrystalline silicon (poly-Si) can be obtained by furnace annealing and excimer laser annealing (ELA) applied on amorphous silicon (a-Si). However, the process temperature of furnace annealing is 550 ℃, which may induce the melting of glass substrate. The linear absorption coefficient of a-Si at the wavelength from 248 to 308 nm is two thousand times higher than that at a wavelength of 800 nm. FLA is still able to anneal a-Si in a fluence about 50 mJ/cm^2, which is lower than ELA process. The largest average grain size obtained by irradiates a-Si with appropriate number of laser pulses is about 800 nm. This is accompanied with good surface roughness (RMS roughness < 10 nm). Polycrystalline silicon processed by FLA is applied on TFT fabrication and a highest mobility of 160 cm^2/Vs is obtained. The highest mobility and trap state density of FLA processed TFTs is similar to that of ELA processed TFTs. This also approved the potential of FLA on TFT fabrication.

As the scaling down of microelectronics devices continues, stringent control on

 iii

the lateral and vertical diffusion of the device's junction is necessary to prevent short channel effect. Thus ultrashallow and highly activated junctions are essential for metal-oxide-semiconductor field effect transistor production. Although rapid thermal activation and ELA already being studied and approved to be effective technique on dopant activation, dopant diffusion in several tens of nanometer is still observable. Irradiated by femtosecond pulses, structural change can occur while the electronic systems of the lattice are not in thermal equilibrium with each other. Such a non-thermal melting mechanism could minimize dopant diffusion (~ 10 nm) significantly by reducing the thermal budget of activation. The measured sheet resistance and activation efficiencies of ion-implanted samples were in the range of 100-400Ω/□ and 28-35% respectively. Dopant loss which is frequently observed in thermal activation is also improved quite substantially. Ultrafast laser activation on Ge substrate also shows good performances.

Grain size of poly-Si is very important because it correlates with the mobility of TFT. Traditionally, the grain size is examined by scanning electron microscopy. However, Secco etching is required for sample preparation of SEM, which may cause damages on the sample. By using optical-pump–THz-probe (OPTP) technique we can measure the temporal evolution of far-infrared conductivity and refractive index which is induced by the optical pump beam. We can also examine the carrier mobility of FLA-processed poly-Si by OPTP technique.

Acknowledgement (致 謝)

博士班的研究生涯終於告一段落。首先我要感謝潘老師這幾年來的耐心指導，讓我在研究的路上能排除困難達成目標。同時也感謝國家奈米元件實驗室的謝博士對於研究方向以及實驗設備的大力支持。我也要感謝安惠榮老師及冉曉雯老師在實驗上給我的指導及幫助。此外也感謝所有的好朋友們以及在實驗室中與我一起努力的夥伴們，你們的支持是我在遭遇挫折時的最大支柱。

感謝我的父母及家人們在我求學的這些年對我的支持以及包容，讓我能無後顧之憂的專注於研究。也感謝朋友們的支持及協助，希望能與你們一起分享完成這篇論文的喜悅。

怡超 2007/12/26

Table of Contents

List of Figures

Chapter 1

Chapter 2

Chapter 3

Chapter 4

List of Tables

Chapter 2

Chapter 3

Chapter 4

Chapter 1

Introduction

Low temperature polycrystalline silicon (LTPS) thin film transistors (TFTs) have received much attention in recent years because of their wide applications in active matrix liquid crystal displays (AMLCDs) and organic light-emitting displays (OLEDs) [1-2]. Low-thermal-budget techniques, such as plasma-assisted hydrogen-induced crystallization [3], metal-induced crystallization [4], and laser-induced crystallization are commonly employed to crystallize the channel regions of LTPS-TFTs [5-12]. Unlike annealing and activation using continuous-wave (CW) and long pulse lasers, nonlinear photo-energy absorption and non-equilibrium thermodynamics are expected to dominate the interactions between the intense femtosecond laser pulses and irradiated transparent materials [13-18]. Such a non-linear process provides precise and low-threshold fluence associated with femtosecond laser-ablation [15-18]. The goal of this work is to develop a new approach of ultrafast laser for recrystallization and dopant profile engineering. In this chapter, an overview of the laser crystallization and laser activation techniques which have been well studied is provided firstly. Next, time-resolved terahertz spectroscopy, which is a non-contact, non-destructive measurement and has been frequently applied to the study of materials, is introduced. Time-resolved terahertz spectroscopy is able to be applied to identify the crystallinity of polycrystalline silicon (poly-Si) in this work.

1.1 Introduction of Low Temperature Poly-Si TFTs

High-performance silicon devices on insulators have recently been incorporated in various new applications, such as AMLCDs and lightweight flat panel displays. However, the first generation of AMLCDs rely on a-Si:H TFTs as switching elements. Although

a-Si:H TFTs have the advantages of low processing temperature and low leakage current, the low electron field-effect mobility (typically below 1 $cm^2V^{-1}s^{-1}$) implies its limitation as switching device. Thus the panel size and resolution of LCD panel is also limited.

Polycrystalline silicon TFTs essentially have higher field effect mobility than a-Si:H TFTs. Thus poly-Si reasonably brings benefits of higher driving current, higher aperture ratio and low power consumption to TFT performance [19]. Besides, the peripheral driving circuits can be realized by integration of complementary metal-oxide-semiconductor (CMOS) circuits on the panel. Thus the cost of driver IC can be reduced and the reliability of driver IC can be improved [20]. In addition to crystallization techniques, implant activation is also one of the most important steps for TFT fabrication. Here we focused on the dopant profile engineering which is more crucial for activation of high speed devices.

In order to produce poly-Si TFTs with high performance, plenty of studies have been made to improve the crystallization and activation techniques. The details of crystallization and activation processes will be introduced in following sections.

1.2 Crystallization of Amorphous Silicon (a-Si) Thin Films

Crystallization of a-Si has been taken as the most important process in the fabrication of LTPS TFTs. This is because the crystallized poly-Si serves as the active layer in the TFTs. Thus the quality of crystallized poly-Si affects the performance of TFTs deeply. However, defects such as dangling bonds which mainly exist in grain boundary of poly-Si may deteriorate the performance of TFTs. To avoid the degeneration of performance caused by defects, reduction of grain boundaries in active region can essentially promote the quality of poly-Si. Many efforts therefore have been focused on the enlargement of grain size.

In last two decades, various techniques such as solid phase crystallization (SPC) and laser crystallization have been studied for crystallization of a-Si. Generally speaking, SPC requires a long processing duration to crystallize a-Si at low temperature. However, high

defect density in grain boundary still limits the improvement of TFT performances. In contrast to the solid crystallization process of SPC, laser crystallization process induces the melting of a-Si. Poly-Si will form after the recrystallization of melted a-Si. The details of these two crystallization techniques are introduced as below.

1.2.1 Solid Phase Crystallization

Solid phase crystallization of a-Si is a simple and effective method to acquire poly-Si thin film. Amorphous state is a thermodynamically metastable state; transformation to polycrystalline state can be achieved by given sufficient energy to overcome the energy barrier. To achieve a large grain size, it is important to suppress nucleation instead of grain growth. Therefore, SPC is typically processed at a low temperature. To achieve a larger grain size also implies a longer crystallization time. Thus SPC is generally processed in furnace at a temperature of 600 °C for 24 hours. However, the processing time of SPC is too long and suffers a trade-off between performance and throughput [21].

SPC has an advantage that it can be accomplished in a wide process window of annealing temperature and annealing time. Besides, SPC is a reliable technique due to its simplicity, low cost and excellent uniformity [22]. For practical applications, the average grain size of poly-Si should be about 0.5-1μm. However, high defect density always exists in crystallized poly-Si. These defects may result in a saturation of electrical performance of TFTs with a corresponding grain size of 0.3-0.5 μm. Thus the poly-Si TFTs processed by standard SPC can only show mediocre performance with mobilities in the range of 20-40 cm^2/Vs.

1.2.2 Excimer Laser Crystallization

Shtyrkov et al. initiated pulsed laser annealing and reported that the lattice damage induced by implantation into crystalline silicon could be repaired as well as activated by

laser annealing [23]. Plenty of works on the use of pulsed laser annealing were conducted in the 1980s. The first study of pulsed laser crystallization of a-Si film was published by Sussmann et al. in 1980 [24]. The crystallization of a-Si films on glass substrate was also published in this decade [25]. For excimer laser annealing (ELA), pulse to pulse repeatability, output energy and pulse duration may affect the film quality dramatically.

Laser annealing with low fluence describes a condition where the incident laser fluence is sufficient to melt the a-Si film, but it is also low enough that the un-melted a-Si film remains at the maximum extent of melted area. This condition is also referred to as "partial-melting regime", which corresponds to the microcrystallities of laser-annealed Si film [26]. The high laser fluence corresponds to the situation when the laser fluence is sufficient to melt the Si film completely. This condition is also referred to as "complete-melting regime". The nucleation in this regime occurs as a result of undercooling in the molten-Si. Therefore, the copious nucleation occurs and the grain size obtained in the regime is about ten nanometers in diameter.

Another regime, called super lateral grain growth (SLG), has been found within the process window between the previous two regimes (see Fig.1-1). The grain size in this regime is about several hundred nanometers in diameter. The transformation process associated with this regime has been modeled by Im et al., in terms of near-complete-melting of Si film [27-28]. The drawing picture of this model is that the unmelted islands provide seeds for solidification, thus the lateral grain growth can ensue from the propagating of the solid-liquid interface within the surrounded "undercooled molted Si". The SLG grain growth initiates from seeds located at the Si-SiO_2 interface is shown in Fig. 1-2 [29].

However, the drawbacks of conventional ELA process were related to difficulty in maintaining a proper balance between performance and grain uniformity. The grain

boundaries and small grains in channel may disturb the carrier transportation and deteriorate the TFT performance [30-31].

1.3 Dopant Profile Engineering of Ion –Implanted Semiconductors

Much effort has been focused on the formation of thin insulators, short channels, and shallow junctions for scaling of transistor-based silicon devices to ~100 nm [32]. This is crucial in achieving better performance for these devices in terms of speed, power consumption, and device packing density. Dopant profile engineering is potentially a promising approach for scaling of these devices [33-39]. State-of-the-art dopant profile engineering is established by integrating low-energy implantation [33-35], defect engineering [36-39], and fast solid-phase-epitaxial-regrowth [35, 37] or laser annealing [37-39]. To date, dopant profile control still suffers from boron-enhanced diffusion (BED) [33], transient-enhanced diffusion (TED) [34-35], boron-interstitial clustering [35], and uphill diffusion [36, 39-40], all of which are associated with thermal energy supply during dopant activation.

It has been demonstrated that TED can be eliminated by reducing the implantation energy to sub-keV energies [35]. However, Agarwal et al. have observed that a diffusivity enhancement of a factor of 4 still exists when the implantation energy is decreased to less than or equal to 1 keV [41]. In this regime, BED is thought to be responsible for diffusion enhancement of boron [42]. Besides reducing the energy of the ion implantation, TED and BED can also be minimized by employing a preamorphizing implant (PAI) and/or by reducing the thermal budget of the subsequent anneals. Recent developments of low thermal budget annealing techniques include spike rapid thermal annealing (RTA) and laser annealing.

1.3.1 Rapid Thermal Activation

Although a shallow junction can be formed by low-energy ion implantation and a RTA process, the production of an ultrashallow junction using a conventional process is difficult. Low-energy ion implantation has disadvantages, which include a low-beam current and a low throughput. RTA usually works at a temperature higher than 1000 °C and a short process time (several seconds) [37, 43-44]. Therefore the sheet resistance of implanted sample can be decreased dramatically after RTA processing and the throughput increase a lot in comparison with furnace annealing process. However, RTA cannot completely prevent TED, which increases the junction depth [37, 43-44]. Excimer laser activation, therefore, has been introduced for this application.

1.3.2 Excimer Laser Activation

Activation by excimer laser annealing [37-39, 45-46] (ELA) has been shown to outperform furnace annealing (FA) [37, 45] and even spike rapid thermal processing (RTP) [37, 40, 43-44] on minimizing dopant diffusion (see Fig. 1-3), due to fast thermal energy supply from nanosecond laser pulses. The ELA profile is shallower than the RTA one and, moreover, has a shape completely different from that obtained by the standard thermal process. This is a direct consequence of the melting process. There is also a clear indication that no significant movement of B occurs underneath the melted layer, due to the extremely fast process.

Based on the fact that amorphous/damaged Si should have a slightly lower melting point than crystalline Si, the preamorphized layer can be melted without melting the underlying Si [37]. Since the diffusivity of boron in the liquid phase is about eight orders of magnitude higher than that in the solid state, the boron atoms become nearly uniformly redistributed within the melt depth as shown in Fig. 1-3, thus forming an abrupt junction. Besides, Fig. 1-4 shows that the boron profile advances further into the Si as the number of

pulses increases due to the piling up of boron at the molten/solid interface after the preceding pulse. A highly activated, ultrashallow, and abrupt junction layer can be obtained by optimizing the laser fluence, irradiated pulse number and preamorphization depth.

Nevertheless, dopant diffusion during ELA-based activation is still observed due to the fact that both vacancy-mediated [36, 39-40] and interstitial-mediated diffusion [33-35] mechanisms are enhanced by photoexcited lattice systems like thermally heated lattice systems. Therefore further improvement of activation technique is still required for future applications.

1.4 Time-Resolved Terahertz Spectroscopy

Terahertz (THz= 10^{12} Hz) has been strongly studied for last two decades. The opening of THz era not only made significant contribution to ultrafast phenomena, but also opened wide applications to optoelectronics and biomedical fields. The THz field is roughly defined by the frequency range of 0.1 to 10 THz (see Fig. 1-5), which corresponds to the wavelength of 0.003 to 3 mm. In 1981, Mourou and Auston firstly demonstrated generation and detection THz radiation by a photoconducting switch [47-48]. It was followed by the study of photoconductor dipole antenna as the THz sensor in 1988 [49]. Afterward plenty of works were focused on the dipole antenna and semiconductor surface electric field for THz generation [50-51]. Free-space electro-optic sampling (FS-EOS) technique was further studied by X. C. Zhang et al. to improve signal to noise ratio and dynamic range [52].

THz has highly potential for many applications. In the bioscience, the photon energy of THz is much smaller than X-ray and therefore will not cause harmful photoionization in biological tissues. THz is also hot for chemical detection, mail or luggage inspection, gas spectroscopy, non-contact and non-destructive measurements. The spectroscopic technique using pulsed THz radiation, terahertz time-domain spectroscopy (THz-TDS), has been developed by taking advantage of short pulses of broadband THz emission. THz-TDS has a

time resolution of sub-picosecond and corresponds to a spectral resolution of 50 GHz. Since THz-TDS is a non-destructive measurement, it is suitable for the study of dielectric materials and semiconductors. For example, Grischkowsky et al. use THz-TDS for the study of carrier concentration and absorption characteristics of sapphire and silicon in THz frequency. Therefore we will also use THz-TDS for the non-destructive measurement of poly-Si annealed by Ti:Sapphire laser.

1.5 Motivation

Hydrogenated amorphous silicon (a-Si:H) is used extensively in Thin Film Transistors (TFTs) for Flat Panel Displays (FPDs) and large area imagers, and it is also a promising photovoltaic material. The a-Si:H TFTs have low off-current and sufficient on-current for most applications. However, a-Si:H shows poor carrier mobility due to its disordered crystal structure. The poor mobility will result in the limitation on the pixel sizes for display and other imaging applications. Therefore, poly-Si with higher mobility up to 300cm^2/Vs has been suggested as an alternative of a-Si:H. Recently, high performance poly-Si devices have been applied in many applications such as flat panel displays.

Poly-Si can be obtained by furnace annealing and ELA applied on a-Si. However, the process temperature of furnace annealing is 550 °C, which may induce the melting of glass substrate. Considering of the long pulse duration (~10 ns) of excimer laser, the melting process of a-Si layer is still thermal melting, which starts via the lattice vibration. Therefore, we try to induce nonthermal melting by irradiate the a-Si layer with ultrafast laser pulses (~50 fs) for comparison. The laser pulse promotes electrons from valance (bonding) states to conduction states, resulting in destabilization of the bands and softening of phonon modes. The semiconductor may lose its lattice structure when the phonon modes soften to certain point and undergo a phase transition [13-15]. The effect was observed in semiconductors under intense femtosecond laser excitation in a time scale of subpicosecond.

This subpicosecond time scale is too fast for carrier to transfer energy to lattice, ruling out the possibility of lattice heating via phonon emission. Therefore, the melting in subpicosecond time scale is named as nonthermal melting. Besides, the linear absorption coefficient of silicon at 250 nm (ELA) is 200 times higher than that at 800 nm (FLA) as shown in Fig. 1-6. The nonlinear absorption may play an important role in FLA. After the laser crystallization process, it is also important to put the poly-Si on TFT fabrication. Thus we can analyze the electrical characteristics and the defect state density of femtosecond laser annealed (FLA) TFT.

Dopant profile engineering is potentially a promising approach for the formation of thin insulators, short channels, and shallow junctions for scaling of transistor-based silicon devices to ~100 nm. Activation by ELA has been shown to outperform FA and even RTP (or RTA) on minimizing dopant diffusion. However, dopant diffusion during ELA-based activation is still observed by photoexcited lattice systems like thermally heated lattice systems. Therefore, FLA seems to have a high potential to reduce the lattice heating by reducing the activation duration with ultrashort laser pulses. After activation process, we can analyze the dopant profile and sheet resistance of FLA-processed sample to ensure the activation efficiency.

Since the grain size of poly-Si is one of the key features to affect electrical characteristics of TFTs such as mobility, it is important to examine the grain size of poly-Si before TFT-fabrication. Traditionally, the grain size is examined by scanning electron microscopy (SEM). However, a destructive sample preparation, such as Secco etching is required for SEM. The Secco etch, using ($HF + K_2Cr_2O_7 + H_2O$ in a ratio of $HF : H_2O = 2 : 1$ with 44 g $K_2Cr_2O_7$ dissolved in 1 L of the H_2O has been frequently used to delineate the grain boundary of poly-Si. Besides, SEM picture is limited with a tiny observation area, which can not offer the information about the grain quality in a large area. In this study, the carrier mobility of FLA poly-Si is measured by optical-pump–THz-probe (OPTP) technique.

We also measured the temporal evolution of far-infrared conductivity and refractive index of FLA poly-Si. This technique is contact-free, therefore, damage-free. The quality of poly-Si samples annealed at various pump fluence can be directly identified by OPTP technique.

1.6 Organization of thesis

In Chap. 2, the grain size of FLA-processed poly-Si is firstly analyzed in order to obtain the annealing parameter of FLA. The characteristics of FLA-processed poly-Si are also analyzed by various techniques. The electrical characteristics of FLA-processed TFTs are also measured and applied for the calculation of defect state density.

In Chap. 3, the results of dopant profile engineering by FLA will be shown. The activation parameter which is affected by various sample preparation parameters will also be shown. We will discuss the mechanisms of dopant diffusion due to ion implantation with different ions and different activation parameters. Our results show that FLA has a high potential for future application on ultra-shallow junction activation. Not only the ultra-shallow formation in silicon substrate is important, bulk germanium (Ge) gains the attention for its significantly high carrier mobility. Our preliminary results will be shown in this chapter.

The results of FLA-processed poly-Si analyzed by THz-TDS will be shown in chapter 4. Poly-Si in two different grain sizes can be easily distinguished by OPTP technique. The mobility can also be obtained by fitting the results of THz-TDS measurements with the Drude model. The reason that the increase of mobility for large grain size poly-Si measured by OPTP will be discussed.

References

[1] K. Sera, F. okumura, H. Uchida, S. Itoh, S. Kaneko and K. Hotta, “High-performance TFTs fabricated by XeCl excimer laser annealing of hydrogenated amorphous-silicon film,” IEEE Trans. Electron Devices, vol. 36, pp. 2868-2872, 1989.

[2] J. G. Blake, J. D. Stevens, and R. Young, “Impact of low temperature polysilicon on the AMLCD market,” Solid State Tech., vol. 41, pp. 56-62, 1998.

[3] S. Sriraman, S. Agarwal, E. S. Aydil, and D. Maroudas, “Mechanism of hydrogen-induced crystallization of amorphous silicon,” Nature, vol. 418, pp. 62-65, 2002.

[4] G. A. Bhat, Z. Jin, H. S. Kwok, and M. Wong, “Effects of Longitudinal Grain Boundaries on the Performance of MILC-TFT’s,” IEEE Electron Device Lett. vol. 20, pp. 97-99, 1999.

[5] J. S. Im, H. J. Kim, and M. O. Thompson, “Phase transformation mechanisms involved in excimer laser crystallization of amorphous silicon films,” Appl. Phys. Lett., vol. 63, pp. 1969-1971, 1993.

[6] G. K. Giust, and T. W. Sigmon, “Microstructural characterization of solid-phase crystallized amorphous silicon films recrystallized using an excimer laser,” Appl. Phys. Lett., vol. 70, pp. 767-769, 1997.

[7] S. D. Brotherton, D. J. McCulloch, J. P. Gowers, J. R. Ayres, and M. J. Trainor, “Influence of melt depth in laser crystallized poly-Si thin film transistors,” J. Appl. Phys., vol. 82, pp. 4086-4094, 1997.

[8] J. S. Im, M.A. Crowder, R. S. Sposili, J. P. Leonard, H. J. Kim, J. H. Yoon, V. V. Gupta, H. J. Song, and H. S.Cho, “Controlled Super-Lateral Growth of Si Films for Microstructural Manipulation and Optimization,” Phys. Stat. Sol. A. vol. 166, pp. 603-617, 1998.

[9] A. T. Voutsas, “A new era of crystallization: advances in polysilicon crystallization

and crystal engineering," Applied Surface Science, vol. 208, pp. 250-262, 2003.

[10] M. A. Crowder, P. G. Carey, P. M. Smith, R. S. Sposili, H. S. Cho, and J. S. Im, "Low-Temperature Single-Crystal Si TFT's Fabricated on Si Films Processed via Sequential Lateral Solidification ," IEEE Electron Device Lett., vol. 19, pp. 306-308, 1998.

[11] R. Dassow, J. R. Köhler, Melanie Nerding, M. Grouvogl, R. B. Bergmann, and J. H. Werner, "Laser-crystallized polycrystalline silicon on glass for photovoltaic applications," Solid State Phen. vol. **67-68**, 193-198, 1999.

[12] A. Hara, F. Takeuchi, and N. Sasaki, "Selective single-crystalline-silicon growth at the pre-defined active regions of TFTs on a glass by a scanning CW laser irradiation," IEEE Electron Devices Society, Proc. of International Electron Device Meeting, pp. 209-212, 2000.

[13] S. K. Sundaram, and E. Mazur, "Inducing and probing non-thermal transitions in semiconductors using femtosecond laser pulses," Nature Materials, vol. 1, pp. 217-224, 2002.

[14] A. Rousse, C. Rischel, S. Fourmaux, I. Uschmann, S. Sebban, G. Grillon, Ph. Balcou, E. Förster, J. P. Geindre, P. Audebert, J. C. Gauthier, and D. Hulin, "Non-thermal melting in semiconductors measured at femtosecond resolution," Nature, vol. 410, pp. 65-68, 2001.

[15] K. Sokolowski-Tinten, J. Biakowski, and D. von der Linde, "Ultrafast laser-induced order-disorder transitions in semiconductors," Phys. Rev. B, vol. 51, pp. 14186-14198, 1995.

[16] T. Y. Choi, and C. P. Grigoropoulos, "Plasma and ablation dynamics in ultrafast laser processing of crystalline Silicon," J. Appl. Phys., vol. 92, pp. 4918-4925, 2002.

[17] X. Liu, D. Du, and G. Mourou, "Laser Ablation and Micromachining with Ultrashort Laser Pulses," IEEE Journal of Quantum Electronics, vol. 33, pp. 1706-1716, 1997.

[18] T. Q. Jia, Z. Z. Xu, X. X. Li, R. X. Li, B. Shuai, and F. L. Zhao, "Microscopic mechanisms of ablation and micromachining of dielectrics by using femtosecond lasers," Appl. Phys. Lett., vol. 82, pp. 4382-4384, 2003.

[19] W. G. Hawkins, "Polycrystalline-silicon device technology for large-area electronics," IEEE Trans. Electron Devices, vol. 33, pp. 477-481, 1986.

[20] M. Takabatake, J. Ohwada, Y. A. Ono, K. Ono, A. Mimura and N. Konishi, "CMOS circuits for peripheral circuit integrated poly-Si TFT LCD fabricated at low temperature below 600 °C," IEEE, Trans. Electron Devices, vol. 38, pp. 1303-1309, 1991.

[21] N. Yamauchi and R. Reif, " Polycrystalline silicon thin films processed with silicon ion implantation and subsequent solid-phase crystallization : Theory, experiments and thin-film transistor applications," J. Appl. Phys., vol. 75, pp. 3235-3257, 1994.

[22] M. K. Hatalis and D. W. Greve, "Large grain polycrystalline silicon by low-temperature annealing of low-pressure chemical vapor deposited amorphous silicon films," J. Appl. Phys., vol. 63, pp. 2260-2266, 1988.

[23] E. I. Shtyrkov, I. B. Khaibullin, M. M. Zaripov, M. F. Galyatudinoov and R. M. Bayasitov, Sov. Phys., vol. 9, pp. 1309, 1975.

[24] R. S. Sussmann, A. J. Harris and R. Ogden, J. Nanocrystalline. Solid. vol. 35-36, pp. 249, 1980.

[25] T. Sameshima and S. Usui, Mat. Res. Soc. Symp. Proc., vol. 71, pp. 435, 1986.

[26] W. Sinke, F. W. Saris, Phys. Rev. Lett., vol. 53, pp. 2121, 1984.

[27] J. S. Im, H. J. Kim, M. O. Thompson, Appl. Phys. Lett., vol. 63, pp 2969 1993.

[28] J. S. Im and H. J. Kim, Appl. Phys. Lett., vol. 64, pp. 2303, 1994.

[29] A. T. Voutsas, Applied Surface Science, vol. **208**, pp. 250, 2003.

[30] T. Sameshima, S. Usui and M. Sekiya, IEEE Electron Device Lett., vol 7, pp. 276, 1986.

[31] H. Kuriyama, Jpn. J. Appl. Phys., Part 1, vol. 30, pp. 3700, 1991.

[32] S. M. Sze, Semiconductor Devices physics and Technology.

[33] A. Agarwal, H. J. Gossmann, D. J.Eaglesham, S. B.Herner, A. T. Fiory, and T. E. Haynes, Appl. Phys. Lett., vol. 74, pp. 2435, 1999.

[34] L. S. Robertson, M. E. Law, K. S. Jones, L. M. Rubin, J. Jackson, P. Chi and D. S. Simons, Appl. Phys. Lett., vol. 75, pp. 3844, 1999.

[35] A. Agarwal, H. J. Gossmann, D. J.Eaglesham, L. Pelaz, D. C. Jacobson, T. E. Haynes and Y. Erokhin, Appl. Phys. Lett., vol. 71, pp. 3141 1997.

[36] R. Duffy, V. C. Venezia, A. Heringa, T. W. T. Husken, M. J. P. Hopstaken, N. E. B. Cowern, P. B. Griffin, and C. C. Wang, Appl. Phys. Lett., vol. 82, pp. 3647, 2003.

[37] Y. F. Chong, K. L. Pey, A.T. S. Wee, A. See, L. Chan, Y. F. Lu, W. D. Song and L. H. Chua, Appl. Phys. Lett., vol. 76, pp. 3197, 2000.

[38] C. H. Poon, B. J. Cho, Y. F. Lu, M. Bhat and Alex See, J. Vac. Sci. B, vol. 21(2), pp. 706, 2003.

[39] C. H. Poon, L. S. Tan, B. J. Cho, Alex See and M. Bhat, Journal of The Electrochamical Society, vol. 151(1), pp. G80, 2004.

[40] H. C. H. Wang, C. C. Wang, C. S. Chang, T. Wang, P. B. Griffin,and C. H. Diaz, IEEE Electron Device Lett., vol. 22, pp. 65, 2001.

[41] A. Agarwal, D. J. Eaglesham, H.-J. Gossmann, L. Pelaz, S. B. Herner, D. C. Jacobson, T. E. Haynes, Y. Erokhin, and R. Simonton, Tech. Dig. Int. Electron Devices Meet., pp. 467, 1997.

[42] S. T. Dunham, S. Chakravarthi, and A. H. Gencer, Tech. Dig. Int. Electron Devices Meet., pp. 501, 1998.

[43] V. Privitera, C. Spinella, G. Fortunato and L. Mariucci, Appl. Phys. Lett., vol. 77, pp. 552, 2000.

[44] L. Shao, X. Wang, I. Rusakova, H. Chen, J. Liu, J. Bennett, L. Larson, J. Jin, P. A. W.

van der Heide and W. K. Chu, J.Appl. Phys., vol. 92, pp. 5788, 2002.

[45] S. Baek, T. Jang and H. Hwang, Appl. Phys. Lett., vol. 80, pp. 2272, 2002.

[46] S. Whelan, A. L. Magna, V. Privitera, G. Mannino, M. Italia,C. Bongiorno, G. Fortunato and L. Mariucci, Phys. Rev. B, vol. 67, pp. 075201, 2003.

[47] Mourou G, Stancampiano C V, Antonetti A and Orszag A, "Picosecond microwave pulse generation," Appl. Phys. Lett., vol. 38, no. 6, pp. 470, 1981.

[48] Auston D H, Cheung K P and Smith P R, "Picosecond photoconducting Hertzian dipoles," Appl. Phys. Lett., vol. 45, no. 3, pp. 284, 1984.

[49] Ch. Fattinger, and D. Grischkowsky, "Point source terahertz optics," Appl. Phys. Lett., vol. 53, pp. 1480, 1988.

[50] N. Sarukura, H. Othtake, S. Izumida, and Z. Liu, "High average-power THz radiation from femtosecond laser-irradiated InAs in a magnetic field and its elliptical polarization characteristics," J. Appl. Phys., vol. 84, pp. 654, 1998.

[51] X.-C. Zhang, Perspectives in Optoelectronics, Ed. By Sudhanshu S. Jha, Would Scientific, chapter 3, 1995.

[52] Q. Wu and X. C. Zhang, "Ultrafast electro-optic field sensors," Appl. Phys. Lett., vol. 68, no. 12, pp. 1604, 1996.

Figures

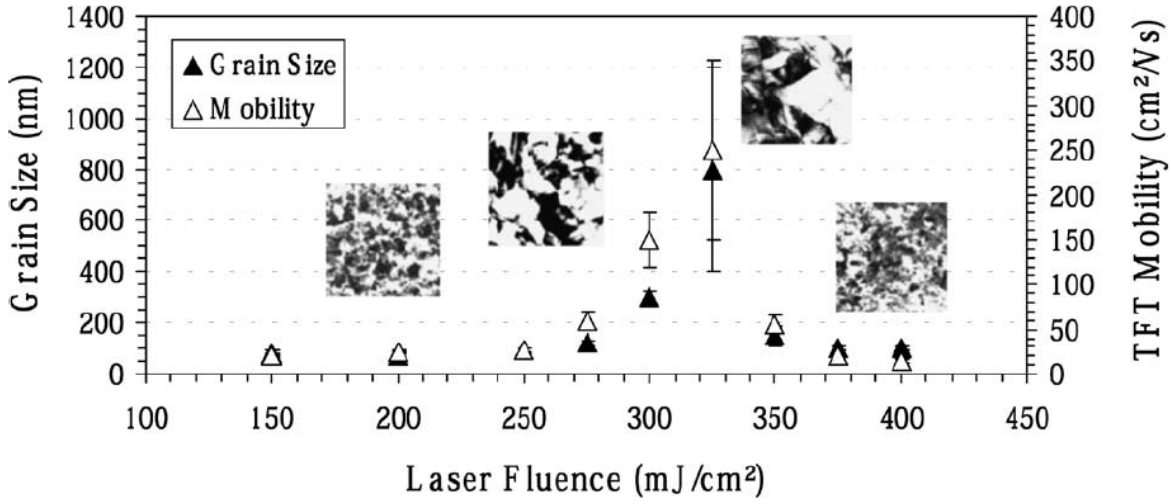

Fig. 1-1 Grain size and corresponding poly-Si TFT mobility vs. laser fluence for conventional ELA process [29].

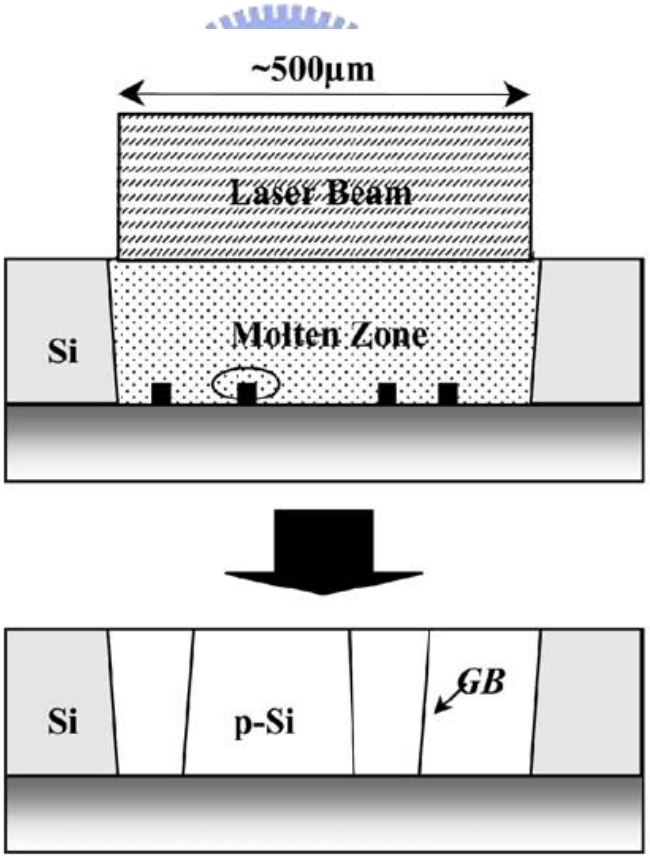

Fig. 1-2 SLG growth initiates from the seeds, which survived in the melting process, at the Si-SiO_2 interface [29].

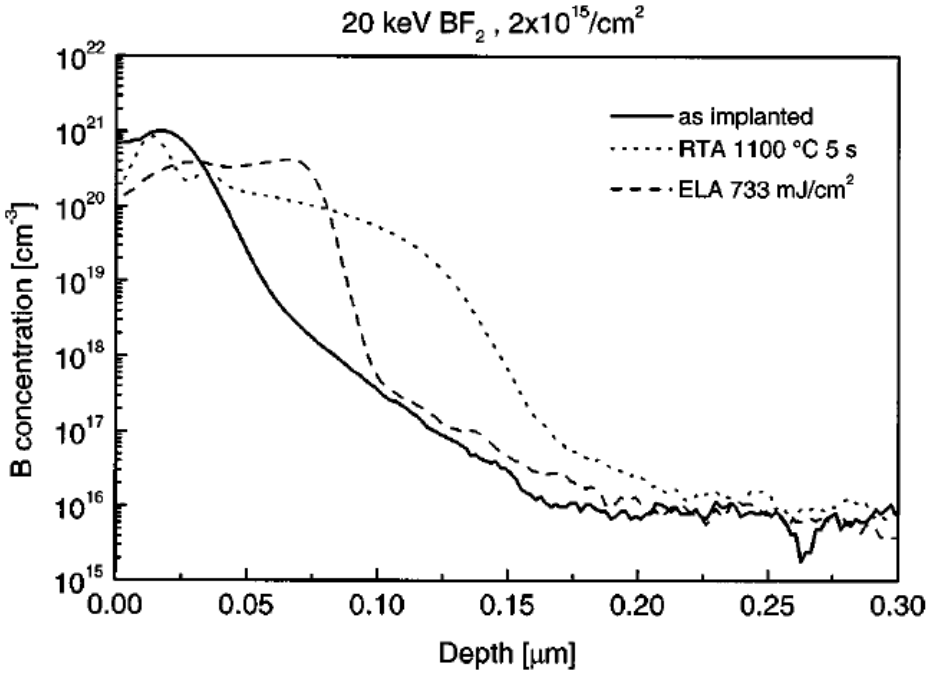

Fig. 1-3 SIMS profiles of a 20 keV BF_2 $2\times10^{15}/cm^2$ before and after annealing. The annealing process was performed by RTA or ELA [43].

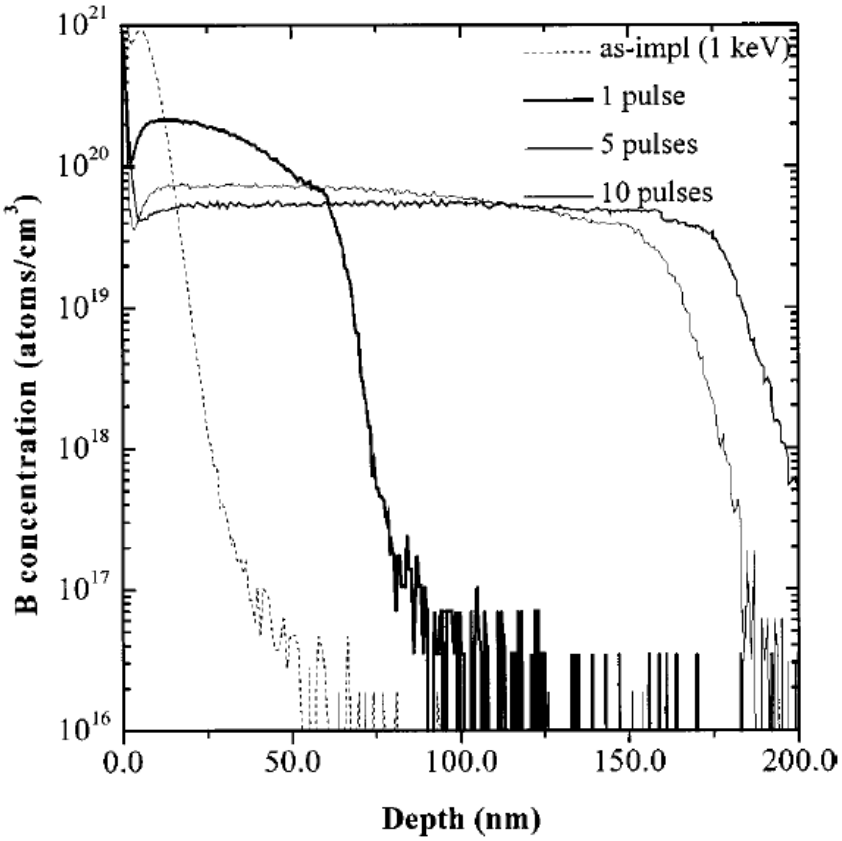

Fig. 1-4 Comparison of boron concentration profiles after laser annealing with successive pulses at 1 J/cm^2.

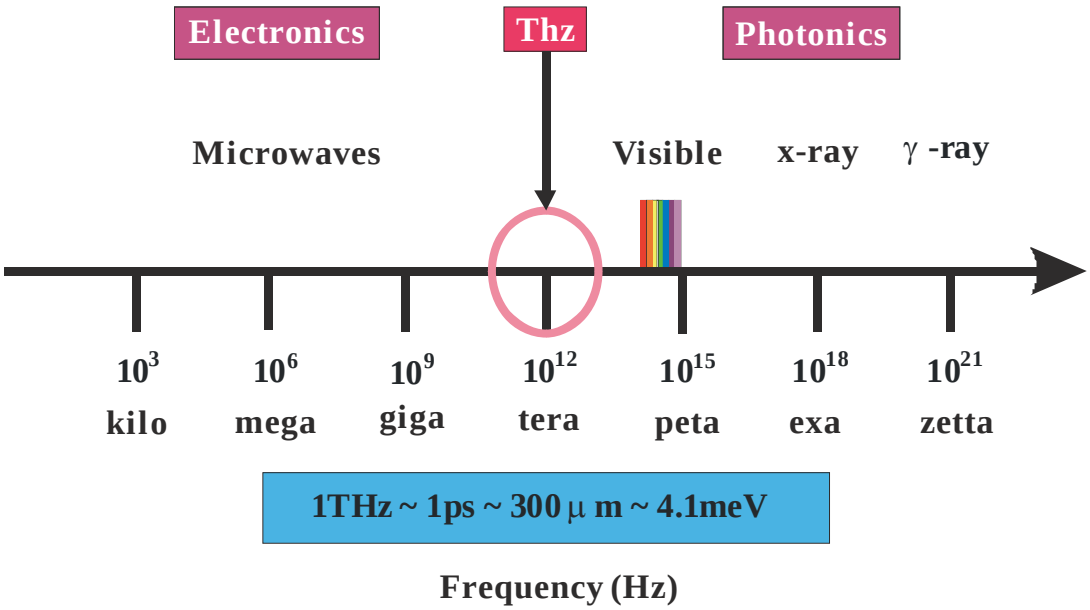

Fig. 1-5 Electromagnetic spectrum of THz.

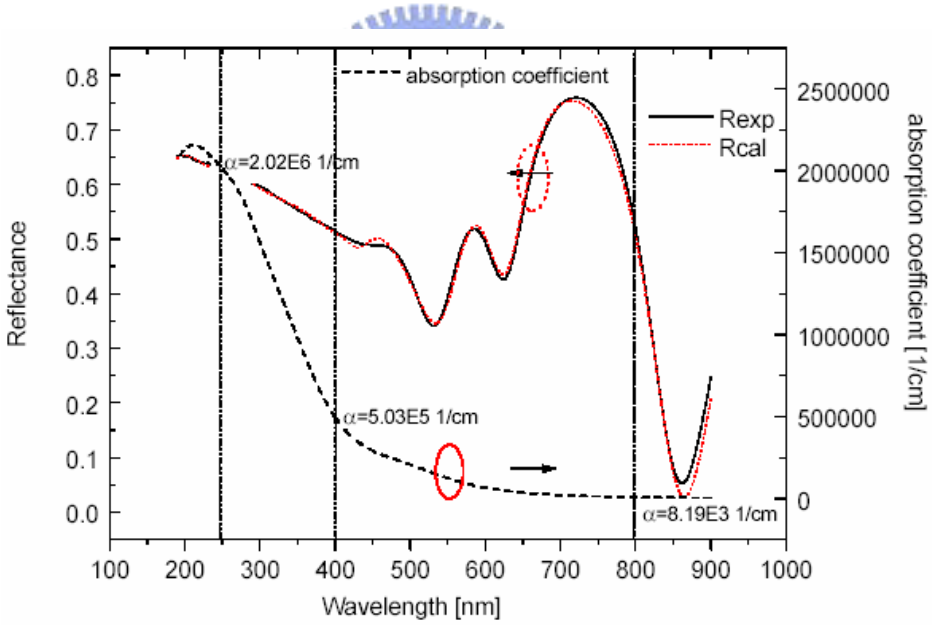

Fig. 1-6 The wavelength dependence of linear absorption coefficient for silicon.

Chapter 2

Femtosecond Laser Crystallization of Amorphous Silicon Thin Films and Characterizations of Crystallized Polycrystalline Silicon Thin Film Transistors

2.1 Introduction

With the demand of larger display area and pixel density of thin film transistor liquid crystal display (TFT-LCD), high mobility TFTs are required for pixel driver of TFT-LCD in order to shorten the charging time of pixel electrodes. Low temperature poly silicon (LTPS) technology has been studied for the purpose integration of drivers at the periphery of active matrix liquid crystal display [1]. Because of its better crystalline quality than amorphous silicon (a-Si), especially the grain size, poly-Si attracted a great attention for last two decades [2-5].

Unlike annealing and activation using continuous-wave (CW) and long pulse lasers, nonlinear photo-energy absorption and non-equilibrium thermodynamics are expected to dominate the interactions between the intense femtosecond laser pulses and irradiated transparent materials [6-11]. Such a non-linear process provides precise and low-threshold fluence associated with femtosecond laser-ablation [8-11]. Due to non-linear photon absorption, the melting of crystal silicon takes place in very short time scale, after 100-800 fs depending on fluence [8]. The purpose of this work is to develop a new approach of using ultrafast laser for recrystallization of a-Si. The quality of poly-Si will be analyzed by SEM and AFM et al. and further examined by measuring the electrical characteristics of FLA-processed TFTs. Good transistor characteristics, as confirmed by measurements of

electrical parameters and grain trap-state densities were obtained for a wide process window of annealing laser fluences.

Firstly, general features of femtosecond laser will be discussed in this chapter. Secondly, the experimental setup of laser annealing will be shown. This will be followed by sample preparation of a-Si and TFT processing for poly-Si. The analyzing results of poly-Si annealed by FLA by several different instruments will be shown in Sec. 2.4.1. The electrical characteristics of FLA-processed TFTs will be shown in Sec. 2.4.2.

2.2 General Features of Femtosecond Lasers

The invention of the laser in 1960 stimulated the development of optical physics and gave rise to many rising research fields. One of these rising research fields was ultrafast optics, which was raised and developed in mid-1960s with the production of nanosecond (10^{-9} s) pulses by the first mode-locked laser. Nowadays, a lot of progresses of ultrafast optics lead to some practical lasers which can produce pulses in the femtosecond (10^{-15} s) time scale. Early in the 1990s, Ti:Sapphire femtosecond lasers became commercially available and ultrafast optoelectronics began to spread all over the world. In this section, our femtosecond laser system will be briefly introduced.

Our femtosecond later system is shown as the block diagram in Fig. 2-1. We use the Ti:Sapphire laser as the seeding laser which is then injected into the Ti:Sapphire regenerative amplifier (Spitfire, Spectra-Physics) for amplification.

The pump laser for the Ti:Sapphire laser (Spectra Physics Tsunami) is a 5W frequency doubled diode-pumped Nd:YVO_4 laser (Millennia Vs, Spectra-Physics) with a wavelength λ=532 nm. The Ti:Sapphire laser provides an output train of intense 35 fs pulses with wavelengths ranging from 770nm to 830 nm. The pulse repetition rate is ~82 MHz and the output power can reach 0.5 W.

The pump laser for the amplification process in Spitfire is a Q-switched Nd:YVO_4 laser. This Nd:YVO_4 laser delivers a high average power output of 20 W at 527 nm. The chirped-pulse amplification diagram of Spitfire is shown in Fig. 2-2. The Spitfire amplifies the seeding pulses by a million times from pulse energy of 6 nJ to 2 mJ. The repetition rate is 1 kHz and the output average power is 2 W. The properties of the Ti:Sapphire regenerative amplifier are shown in Table 2-1.

2.3 Experiment setup and procedures

2.3.1 The Setup of Femtosecond Laser Crystallization and Sample Preparation

Silane-based a-Si films (100 nm) were deposited on oxidized (500 nm) silicon wafers by low-pressure chemical vapor deposition (**LPCVD**) at 550 °C. An infrared femtosecond Ti:Sapphire laser system (TSUNAMI, and SPIT FIRE, from Spectra-Physics company) with a wavelength of 800 nm, a repetition rate of 1 kHz, a pulse duration in the range of 50-125 fs, and an output energy per pulse of ~0.5 mJ, was guided to crystallize amorphous silicon as shown in Fig. 2-3. All samples were placed in a vacuum chamber, and a heater increased the substrate temperature up to 400 °C (see Fig. 2-4). A two-axis transition stage was used for the line-scan FLA as shown in Fig. 2-5.

First, we made a steady-state multiple shots FLA experiment (overlapping 100% with 20 laser shots). The pulse train from the mentioned laser system was focused in the strip spot (3 mm×250 μm). We changed the fluence (38-63 mJ/cm^2) and the number of shots (5-100). For comparison, we also processed the line-scan FLA with different laser fluence (28-70 mJ/cm^2) and interpulse overlapping (10-99%), which corresponds to the number of laser shots from 10-99.

2.3.2 Fabrication of Femtosecond Laser Crystallized Poly-Si TFTs

Amorphous Si layers of 100 nm were deposited by low pressure chemical vapor deposition (**LPCVD**) at 550 °C on 500 nm-SiO_2-coated silicon wafers. The active layers for the TFTs were crystallized by line-scanning irradiation of twenty ultrafast (~ 50 fs) near-infrared (λ = 800 nm) laser pulses with fluences of 34-50 mJ/cm^2 (or total fluences of 20 laser pulses about 0.68-1.0 J/cm^2). The beam spot size was 8 mm ×110 μm. During the scanning process, the overlapping of neighboring pulses was fixed at 95%. FLA was conducted on a substrate heated at 400 °C in a vacuum chamber. FLA-crystallized layers were then defined into active regions for transistors with channel length (L)/ channel width (W) of 2μm/2μm, 3μm/3μm, 5μm/5μm, and 10μm/10μm. A SiO_2 gate dielectric layer of 50 nm and polycrystalline silicon gate layer of 150 nm were then grown by LPCVD and patterned for self-aligned phosphorous implantation with dosage of 5×10^{15} cm^{-2}, and energy of 53 keV. After thermal activation and metal connection were performed, n-type transistors were completed.

For comparison, TFTs with channels crystallized by furnace annealing (solid phase crystallization, SPC) in nitrogen ambient at 600 °C for 24 hours were also processed on the same run. The transfer characteristics (drain current $\boldsymbol{I_d}$ versus gate voltage $\boldsymbol{V_g}$) of the devices were measured at a drain voltage $\boldsymbol{V_d}$ = 0.1 V, to extract electrical parameters. Grain trap-state densities, $\boldsymbol{n_{GT}}$, for all TFTs were also examined using the field-effect conductance method [12].

2.4 Results and Discussions

2.4.1 Material Characterization of Femtosecond Laser Crystallized Poly-Si Thin Films

Scanning electron microscopy (SEM) pictures of annealed areas (Fig. 2-6) with obvious grain boundaries, obtained by delineating defects using Secco etching, show the high

uniformity of poly-Si grains. Pictures from (a) to (d) in Fig. 2-6 represent steady-state multi-shot samples irradiated with 20 laser pulses of 50 fs with different energy densities. The average grain size is relatively small (smaller than 50 nm) and almost independent on the energy density. It should be mentioned that in comparison to linear ELA for non-linear steady-state FLA, small grains (<50 nm) might probably be due to the fact that fast cooling (or laser-energy turn-off) associated with short pulses causes random recrystallization from more nucleation sites [5].

The situation is dramatically changed when we introduce scanning. In our second experiment we scan the laser beam along the sample with the speed of 2.5-25 mm/sec (10-100 laser-shots per unit area, or, equivalently, an overlapping of 90-99%). Pictures from (e) to (h) in Fig.2-6 represent line-scan FLA samples irradiated with 95% interpulse overlapping of 50 fs laser pulses with different energy densities. As shown in Fig. 2-7, the average grain sizes of FLA pc-Si films are plotted as a function of laser energy density (denoted as E_L) and pulse duration for both steady-state and line-scan FLA. Herein, annealing parameters for line-scan (steady-state) FLA were overlapping ~95 % (20 laser-shots).

For line-scan FLA using 125 fs pulses, the grain sizes of the crystallized a-Si films initially increased, and then saturates, before finally declining as the laser fluence was increased from 35 mJ/cm^2 to 61 mJ/cm^2. The maximum average grain size was around 200 nm when a-Si films were irradiated at 50 mJ/cm^2. Despite the difference between the mechanism of photoexcitation-melting using FLA (non-linear annealing) [6-10] and that using nanosecond or longer pulse laser annealing (linear annealing), such as ELA, lateral elongating still dominates the growth of grains in FLA pc-Si films.

With reference to SLG phenomena [5, 13-14], laser fluence (grain sizes) in line-scan FLA can be reasonably divided into three major regimes of partial-melting (small grains), near-complete-melting (largest grains), and complete-melting (fine grains), which fit well

the trends plotted in Fig. 2-7. For line-scan FLA using short pulses with 50 fs duration, the trend in average grain sizes of FLA pc-Si films versus E_L is similar to that obtained with 125 fs pulses, but the maximum average grain size (800 nm) of crystallized films, and the optimal E_L of crystallization (47 mJ/cm^2) for FLA using 50 fs pulses are markly better than those for FLA using 125 fs pulses. The increase in the efficiency of nonlinear photo-energy absorption [15-16] with the peak power of the laser pulses during infrared FLA, is responsible for the dependence of the grain sizes of line-scan FLA pc-Si films on the duration of pulses, and the laser fluence.

It is remarkable that the maximum of average grain size (~800 nm) equals the wavelength used. This phenomenon is also observed in ELA: in multiple pulse irradiations [15]. Typically, this is related to the interference effects at the surface due to reflection of the hillocks that are formed at the grain boundaries. But in FLA we do not observed such kind of phenomena in the steady-state multiple shots experiment. Only scanning leads to grain elongating. Therefore, we may conclude that we observed the SLS(sequential lateral solidification)-like mechanism (will be discussed later).

The examination of grain sizes of line-scan FLA pc-Si films crystallized at various overlapping, at E_L values of 47 mJ/cm^2 and 38 mJ/cm^2 for 50 fs pulses, and 50 mJ/cm^2 for 125 fs pulses, is shown in Fig. 2-8. The required laser-shots is lower for FLA using shorter pulses and higher E_L. Typically, 10 to 100 laser-shots are required to perform laser linear annealing [5, 13, 17]. But again we should mention that increasing of the pulse numbers or shots in the steady-state FLA does not result in enlarging of crystallized grains (Fig. 2-8).

On the other hand, the data in Fig. 2-7 and 2-8 for line-scan FLA clearly demonstrates the high effectiveness of scanning and non-linear photo-absorption in crystallizing amorphous silicon. Assuming a Gaussian shape of the laser beam, for the steady-state mode, each illuminated point is repeatedly shined by the same energy. The first few laser pulses

transform the amorphous material into the poly-phase with large grain distribution. The last pulses (with the same energy) cannot significantly change that distribution.

In the line-scan mode, each illuminated point is also repeatedly shined. But the shined energy for the considered area is not the same from pulse to pulse. It follows a Gaussian sequence. That is possible reason why smaller grains have possibilities in gaining larger energy, therefore, resulting in grain-re-growing into larger grains. Thus, suggested SLS-like mechanism, assisted with the feature of low melting-energy for small grains obtained with the steady-state FLA, significantly enlarges the grain-size of line-scan FLA pc-Si films. Moreover, for ultra-short laser pulses the melting thickness is determined by non-linear absorption skin depth rather than heat penetration length due to thermal conduction [10], and thus more insensitive to laser-fluence in comparison with that for linear annealing. Besides the proposed SLS-like mechanism, this melting-depth thinning mechanism during FLA is also responsible for the significant process window in laser fluence (45-60 mJ/cm^2) for line-scan FLA using 50 fs pulses.

The RMS roughness measured by the atomic force microscopy (AFM) of all FLA pc-Si films is below 4.5 nm. The peak-to-peak roughness is about 26 nm for line-scan FLA samples. Figures 2-9 (b) and (c) represent the AFM images of line-scan and steady-state FLA pc-Si films respectively. The crystalline fraction in such films exceeds 98 %, as calculated from their Raman spectra in Fig. 2-9 (a), in which a sharp peak at 519.5 cm^{-1}, and the absence of a broad peak at 480 cm^{-1} associated with amorphous phase, implies the high crystallinity of the FLA pc-Si films [16]. Diffraction spots on the TEM selected area diffraction patterns of FLA pc-Si irradiated with 50 fs pulses, presented in Fig. 2-10, reveal that those films are highly crystalline. The corresponding XRD spectrum in Fig. 2-11 shows that the preferred orientation of FLA pc-Si is <111>, same as the orientation of those annealed by other types of lasers [21, 22].

The maximum grain size of FLA pc-Si films increases twice (400 to 800 nm) as the substrate temperature increases from room temperature to 400 °C (see Fig. 2-12). James S. Im et al. observed similar results in ELA pc-Si films, explaining them by a longer time for lateral growth (larger grains) due to higher substrate temperatures (or lower quenching rates [18]). Conventional laser thermal annealing makes the grain sizes of annealed films relatively insensitive to the thermal energy from the substrate temperature, because laser thermal annealing "heats" the lattice to a melting temperature far above the substrate temperature. This implies that the substrate temperature more strongly influences grain growth in films crystallized by FLA using shorter pulses than by ELA using longer pulses, and by laser thermal annealing, thus explaining the trend observed on Fig. 2-12.

2.4.2 Electrical Characterization of TFTs Fabricated by Femtosecond Laser Crystallization

In Fig. 2-13, we have plotted logarithmic transfer characteristics and linear transconductance (G_m) curves for some representative TFTs fabricated by FLA and SPC. For TFTs with channel dimensions of W = L = 10 μm and W = L = 2 μm, the on/off current ratio was better than 10^7. As the laser fluence decreased from 51 to 34 mJ/cm^2, significant decrease of G_m was observed due to the deterioration of crystallinity.

The maximum G_m of TFTs fabricated by SPC was lower than that of TFTs annealed by FLA even at the lowest fluence we employed. The maximum values of G_m were analyzed to yield the field-effect electron mobility (μ_{FE}). The threshold voltage (V_{th}) and the subthreshold slope (S) were then extracted using the procedure described in reference 23. Electrical parameters of FLA-processed TFTs are presented as functions of channel sizes and laser energy in Fig. 2-14.

The I_d-V_g curves of TFT with channel dimensions of W = L = 5 μm measured at different temperatures (Fig. 2-15) were required to extract the grain-trap-state densities. The

I_d-V_g curves of TFT with different channel dimensions are not shown here. It is well-known that the tail-state density of grain traps, N_G, closely correlates with channel crystallinity [24]. We find that the values of N_G at an energy (E) ~ 0.5 eV above the Fermi level (E_F), for transistors with channels of 5μm/5μm, decrease from ~3.5×10^{21} to 1.5×10^{21} $eV^{-1}cm^{-3}$ as the laser fluence increases from 37mJ/cm^2 to 50mJ/cm^2. This is shown in Fig. 2-16. Clearly, larger grains with fewer associated defects were obtained at increasing laser fluence up to 50mJ/cm^2. This reduces considerably the height of the barrier to carrier transportation in the channels. As a result, higher G_m values are obtained (see Fig. 2-13). Similar trend for μ_{FE} can be observed in Fig. 2-14, regardless of channel sizes.

Increasing channel crystallinity normally reduces the density of the grain defects, including deep-states defects. For example, increasing laser fluences decreases deep-state and midgap-state densities of grain traps for the device with channels of 5μm/5μm, to 4×10^{18} cm^{-3} (at $E-E_f = \Delta E = 0.25$ eV), and 1×10^{18} $eV^{-1}cm^{-3}$ (at $\Delta E \sim 0$ eV), respectively (See Fig. 2-16).

Area densities of grain trap-states, N_G, at $\Delta E = 0$ eV for devices in Fig. 2-16, are estimated from $N_G \approx n_{GT}.t_{CLC}$ where t_{CLC} represents the thickness of FLA-crystallized polycrystalline silicon. For the same TFT, we find that the values of N_G are in good agreement with those of the effective trap state densities N_t calculated from subthreshold slope. Previous workers have shown that the values of N_G were more affected by interface defects associated with channel roughness in the ELA processed TFTs [25]. The fact that $N_G \approx N_t$ implies that channel crystallinity rather than channel roughness in such FLA-crystallized polycrystalline silicon layers, which exhibit sub-micro grains and smooth surfaces with roughness of ~ 4-9 nm, dominates electrical characteristics of fabricated transistors (See Figs. 2-14 and 2-16). The deep-state dominated subthreshold slope and threshold voltage both follow the trend of reduction in grain deep-states densities with laser fluence (See also Figs. 2-14 and 2-16) [24]. The grain trap-state densities in Fig. 2-16 also

show that the FLA-annealed TFTs are superior to SPC-annealed TFTs, consistent with that of the electrical parameters presented in Fig. 2-14.

In the range of laser fluences of 37-50 mJ/cm^2, the electrical characteristics of TFTs crystallized by FLA vary by at most 30%, regardless of channel sizes. The relatively small variations of electrical parameters for fractional change of fluence ($\Delta E/E$) in FLA is lower than that reported (80%) of TFTs fabricated by ELA [26]. Such a wide FLA-crystallization window as determined by transistor characteristics agrees with our studies of structural characteristics of poly-Si crystallized by FLA and grain trap-state densities associated with channel crystallinity as presented herein.

The tail-state densities (at ΔE= 0.5 eV) of FLA-fabricated transistors with different channel sizes were in the range of 6×10^{20} to 1×10^{21} eV^{-1}cm^{-3}. The values are of the same order of magnitude as those obtained from ELA-crystallized polycrystalline silicon layers [25]. As a result, mobilities of FLA-fabricated transistors, μ_{FE} ≈ 80-160 cm^2/Vs, are also comparable to those for ELA-fabricated transistors. We also note that grain trap-state densities for those channels with different sizes but the same crystallinity decline as channel size decreases. Fewer numbers of grain defects in smaller channels will surely result in better electrical characteristics in TFTs as seen in results for FLA-fabricated TFTs (Fig. 2-14) [27].

2.5 Summary

The characteristics and annealing parameters for silicon films crystallized by FLA herein are compared with those obtained by other annealing methods [13, 17-20] and summarized in Table 2-2. The intense ultrashort laser pulses lead to efficient non-linear photo-energy absorption and the generation of dense photoexcited plasma in irradiated materials, enabling melting of a-Si films that are nearly transparent at 800 nm. FLA assisted by spatial scanning of laser strip spot efficiently crystallizes a-Si films with large average

grains of 800 nm, using laser fluence as low as ~45 mJ/cm^2, and low number of laser shots (20 shots). Moreover, FLA exhibits a significantly wide operating window for laser-fluence (45-60 mJ/cm^2, or, equivalently, ~30% variations), which makes it possible to implement suggested method in the TFT industry.

Polycrystalline silicon transistors fabricated by near-infrared femtosecond laser annealing were demonstrated for the first time. The FLA-annealed poly-Si channels exhibit low tail-state, deep-state, and midgap-state densities of grain traps of ~1×10^{21}, ~5×10^{18}, and ~9×10^{17} eV^{-1}cm^{-3}. Field-effect mobility, threshold voltage, and subthreshold slope for transistors fabricated on poly-Si annealed with a total fluence of 0.9 J/cm^2 in a line-scan mode were measured to be 80-160 cm^2/Vs, 1-3 V, and 0.4-0.8 V/dec, respectively. A wide process window for annealing laser fluences, 37-50 mJ/cm^2, was confirmed by examining the changes in electrical parameters for transistors with various channel dimensions. Thus the performance of FLA-fabricated transistors is comparable to that of ELA-fabricated transistors.

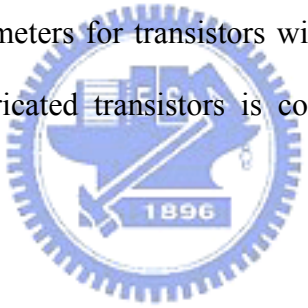

References

[1] K. Sera, F. okumura, H. Uchida, S. Itoh, S. Kaneko and K. Hotta, "High-performance TFT's fabricated by XeCl excimer laser annealing of hydrogenated amorphous-silicon film," IEEE Trans. Electron Devices, vol. 36, pp. 2868, 1989.

[2] E. Ibok and S. Garg, "A characterization of the effect of deposition temperature on polysilicon properties," J. Electrochem. Soc., vol. 140, pp. 2927, 1993.

[3] R. Kakkad, J. Smith, W. S. Lau, S. J. Fonash, and R. Kerns, "Crystallized Si films by low-temperature rapid thermal annealing of amorphous silicon," J. Appl. Phys., vol. 65, pp. 2069, 1989.

[4] N. Kubo, N. Kusumoto, T. Inushima, and S. Yamazaki, "Characterization of polycrystalline-Si thin-film transistors fabricated by excimer laser annealing method," IEEE Trans. Electron Devices, vol. 40, pp. 1876, 1994.

[5] A. T. Voutsas, "A new era of crystallization: advances in polysilicon crystallization and crystal engineering," Appl. Surf. Sci., vol. 208, pp. 250, 2003.

[6] S. K. Sundaram, and E. Mazur, "Inducing and probing non-thermal transitions in semiconductors using femtosecond laser pulses," Nature Materials, vol. 1, pp. 217-224, 2002.

[7] A. Rousse, C. Rischel, S. Fourmaux, I. Uschmann, S. Sebban, G. Grillon, Ph. Balcou, E. Förster, J. P. Geindre, P. Audebert, J. C. Gauthier, and D. Hulin, "Non-thermal melting in semiconductors measured at femtosecond resolution," Nature, vol. 410, pp. 65-68, 2001.

[8] K. Sokolowski-Tinten, J. Biakowski, and D. von der Linde, "Ultrafast laser-induced order-disorder transitions in semiconductors," Phys. Rev. B, vol. 51, pp. 14186-14198, 1995.

[9] T. Y. Choi, and C. P. Grigoropoulos, "Plasma and ablation dynamics in ultrafast laser processing of crystalline Silicon," J. Appl. Phys., vol. 92, pp. 4918-4925, 2002.

[10] X. Liu, D. Du, and G. Mourou, “Laser Ablation and Micromachining with Ultrashort Laser Pulses,” IEEE Journal of Quantum Electronics, vol. 33, pp. 1706-1716, 1997.

[11] T. Q. Jia, Z. Z. Xu, X. X. Li, R. X. Li, B. Shuai, and F. L. Zhao, “Microscopic mechanisms of ablation and micromachining of dielectrics by using femtosecond lasers,” Appl. Phys. Lett., vol. 82, pp. 4382-4384, 2003.

[12] G. Fortunato and P. Migliorato, “Determination of gap state density in polycrystalline silicon by field-effect conductance,” Appl. Phys. Lett., vol. 49, pp. 1025-1027, 1986.

[13] S. D. Brotherton, D. J. McCulloch, J. P. Gowers, J. R. Ayres, and M. J. Trainor, “Influence of melt depth in laser crystallized poly-Si thin film transistors,” J. Appl. Phys., vol. 82, pp. 4086-4094, 1997.

[14] J. S. Im, M.A. Crowder, R. S. Sposili, J. P. Leonard, H. J. Kim, J. H. Yoon, V. V. Gupta, H. J. Song, and H. S. Cho, “Controlled Super-Lateral Growth of Si Films for Microstructural Manipulation and Optimization,” Phys. Stat. Sol. A., vol. 166, pp. 603-617, 1998.

[15] S. Horita, Y. Nakata, and A. Shimoyama, “Alignment of grain boundary in a Si film crystallized by a linearly polarized laser beam on a glass substrate,” Appl. Phys. Lett., vol. 78, pp. 2250-2252, 2001.

[16] J. E. Gerbi, and J. R. Abelson, “Deposition of microcrystalline silicon: Direct evidence for hydrogen-induced surface mobility of Si adspecies ,” J. Appl. Phys., vol. 89, pp. 1463-1469, 2001.

[17] R. Dassow, J.R. Köhler, Melanie Nerding, M. Grouvogl, R.B. Bergmann, and J.H. Werner, “Laser-Crystallized Polycrystalline Silicon on Glass for Photovoltaic Applications , ” Solid State Phen., vol. 67-68, pp. 193-198, 1999.

[18] J. S. Im, H. J. Kim, and M. O. Thompson, “Phase transformation mechanisms involved in excimer laser crystallization of amorphous silicon films,” Appl. Phys. Lett., vol. 63, pp. 1969-1971, 1993.

[19] A. Hara, F. Takeuchi, and N. Sasaki, IEEE Electron Devices Society, "Selective single-crystalline-silicon growth at the pre-defined active regions of TFTs on a glass by a scanning CW laser irradiation," Proc. of 2000 International Electron Device Meeting, pp. 209-212, 2000.

[20] J. S. Im, R. S. Sposili, and M. A. Crowder, "Single-crystal Si films for thin-film transistor devices," Appl. Phys. Lett., vol. 70, pp. 3434-3436, 1997.

[21] M. Nerding, R. Dassow, S. Christiansen, J. R. Kohler, J. Krinke, J. H. Werner, H. P. Strunk, "Microstructure of laser-crystallized silicon thin films on glass substrate," J. Appl. Phys., vol. 91, pp. 4125-4130, 2002.

[22] S. Christiansen, P. Lengsfeld, J. Krinke, M. Nerding, N. H. Nickel, and H. P. Strunk, "Nature of grain boundaries in laser crystallized polycrystalline silicon thin films," J. Appl. Phys., vol. 89, pp. 5348-5354, 2001.

[23] S. M. Sze, Semiconductor Devices physics and Technology (Academic, 1985).

[24] M. Miyasaka and J. Stoemenos, "Excimer laser annealing of amorphous and solid-phase-crystallized silicon films," J. Appl. Phys., vol. 86, pp. 5556-5565, 1999.

[25] S. D. Wang, W. H. Lo, T. Y. Chang, and T. F. Lei, "A novel process-compatible fluorination technique with electrical characteristic improvements of poly-Si TFTs," IEEE Electron Devices Lett., vol. 26, pp. 372-374, 2005.

[26] Y. F. Tang, S.R.P. Silva and M. J. Rose, "Super sequential lateral growth of Nd:YAG laser crystallized hydrogenated amorphous silicon," Appl. Phys. Lett., vol. 78, pp. 186-188, 2001.

[27] N. Yamauchi, J. J. Hajjar and R. Reif, "Polysilicon thin-film transistors with channel length and width comparable to or smaller than the grain size of the thin film," IEEE Trans. Electron Devices, vol. 38, pp. 55-60, 1991.

Figures

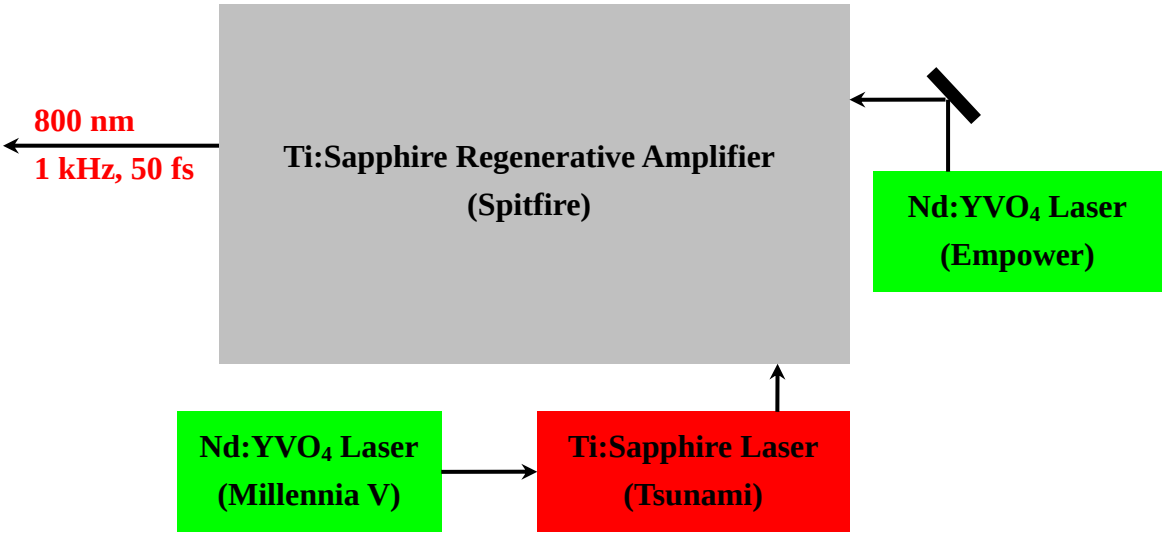

Fig. 2-1 Block diagram of the laser system for FLA experiment.

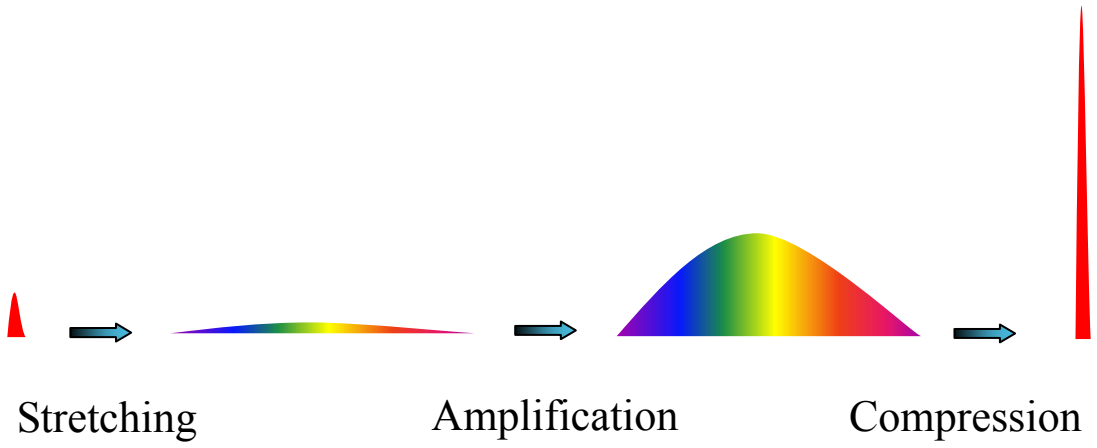

Fig. 2-2 The chirped amplification process of regenerative Ti:Sapphire amplifier system..

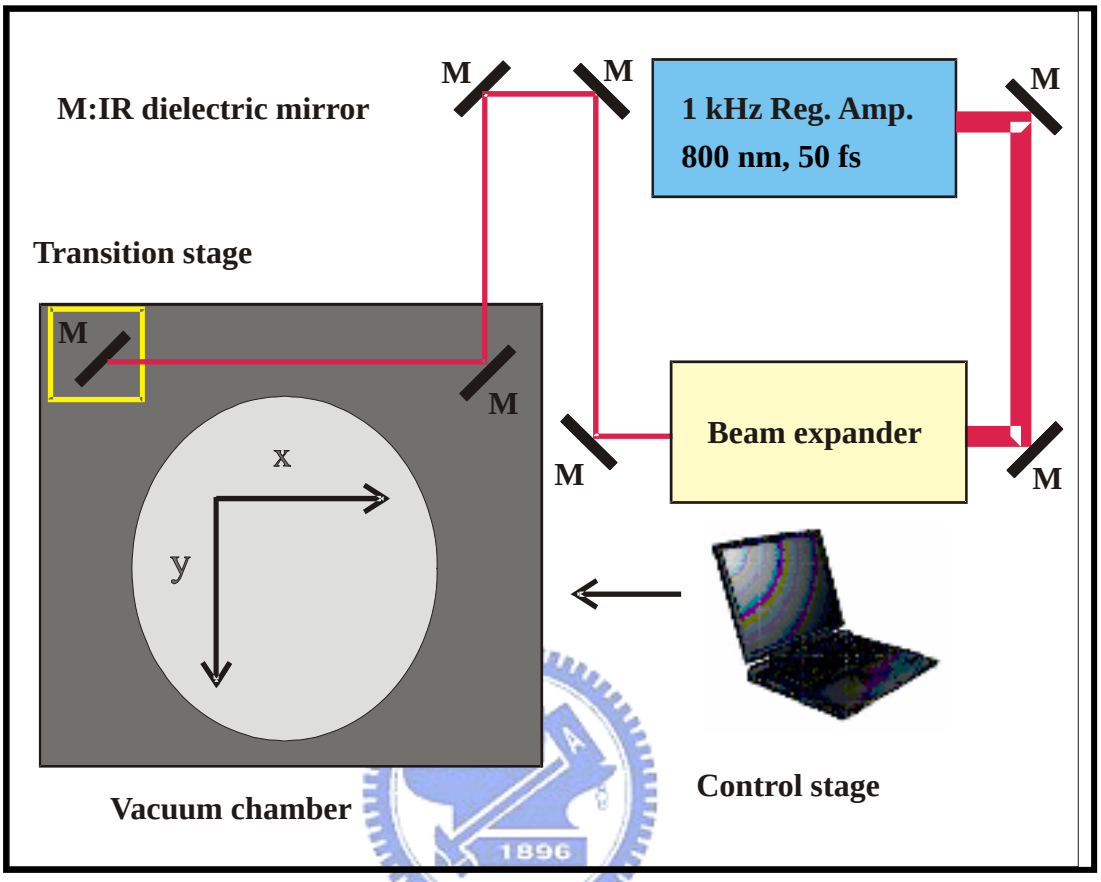

Fig. 2-3 Experimental setup of FLA.

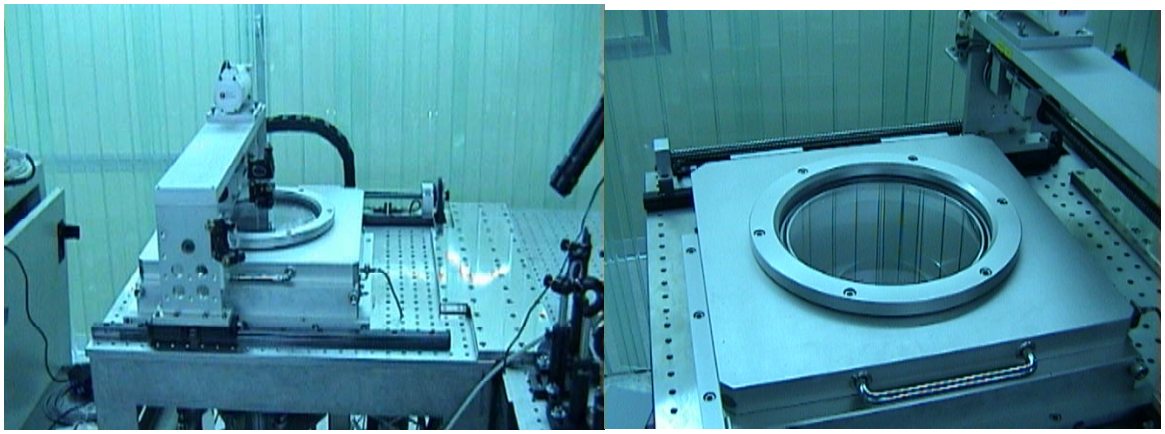

Fig. 2-4 Vacuum chamber and two axis transition stage of FLA experiment.

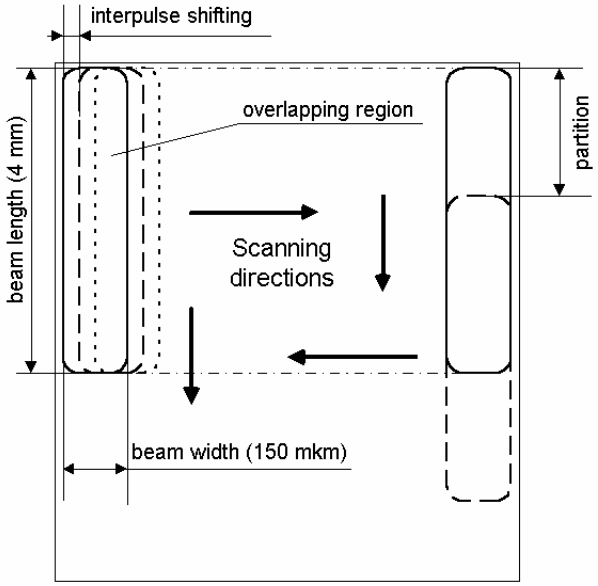

Fig. 2-5 Sketch map of line-scan FLA.

	(a) 38 mJ/cm^2	(b) 44 mJ/cm^2	(c) 50 mJ/cm^2	(d) 56 mJ/cm^2
Overlap 100 % (20 laser shots)	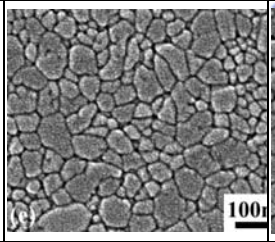	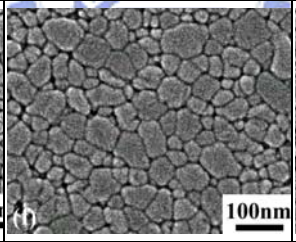	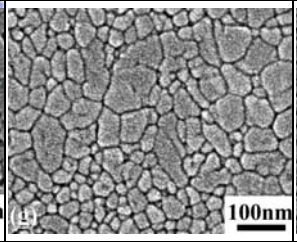	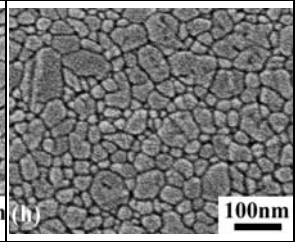
	(e) 28 mJ/cm^2	**(f) 41 mJ/cm^2**	**(g) 46 mJ/cm^2**	**(h) 70 mJ/cm^2**
Overlap 95 % (20 laser shots)	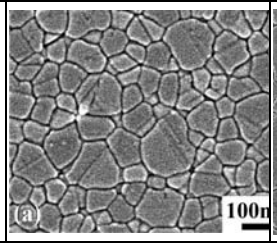	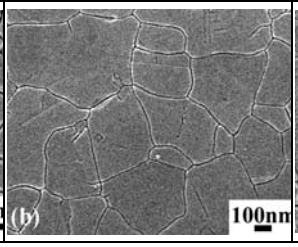	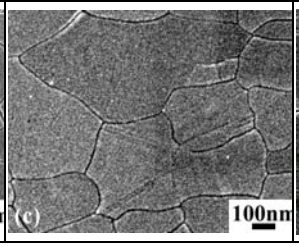	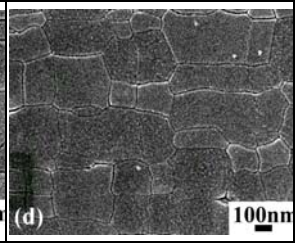

Fig. 2-6 SEM pictures of FLA pc-Si samples after Secco etching for steady-state (a, b, c, d) and line-scanned FLA (e, f, g, h).

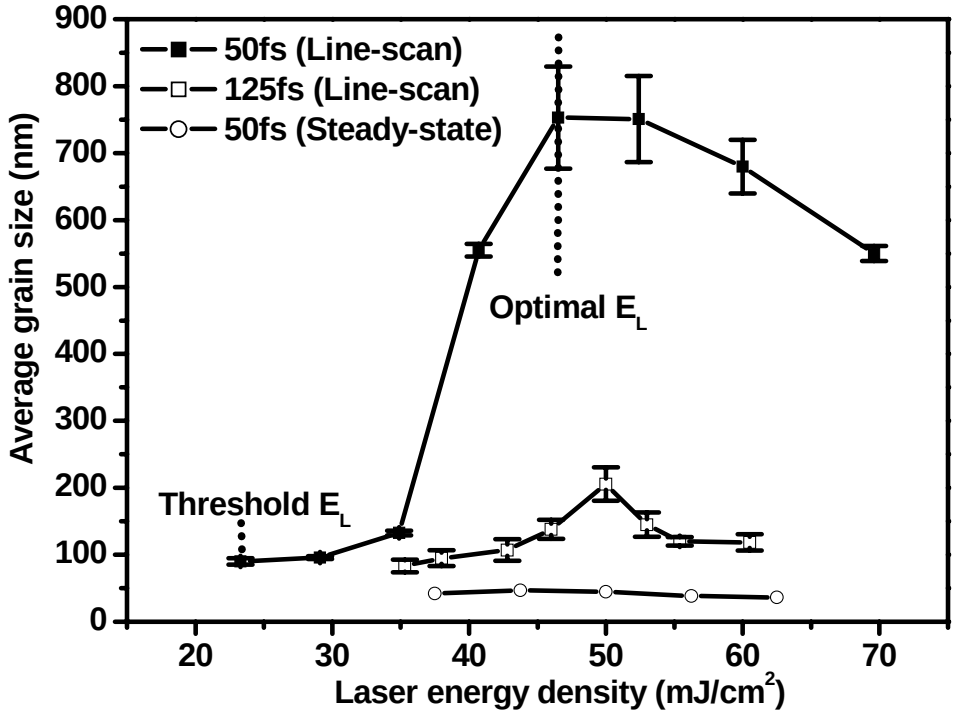

Fig. 2-7 Average grain sizes of FLA pc-Si films, irradiated with pulses of different durations, as a function of laser fluence for steady-state FLA and scanned FLA.

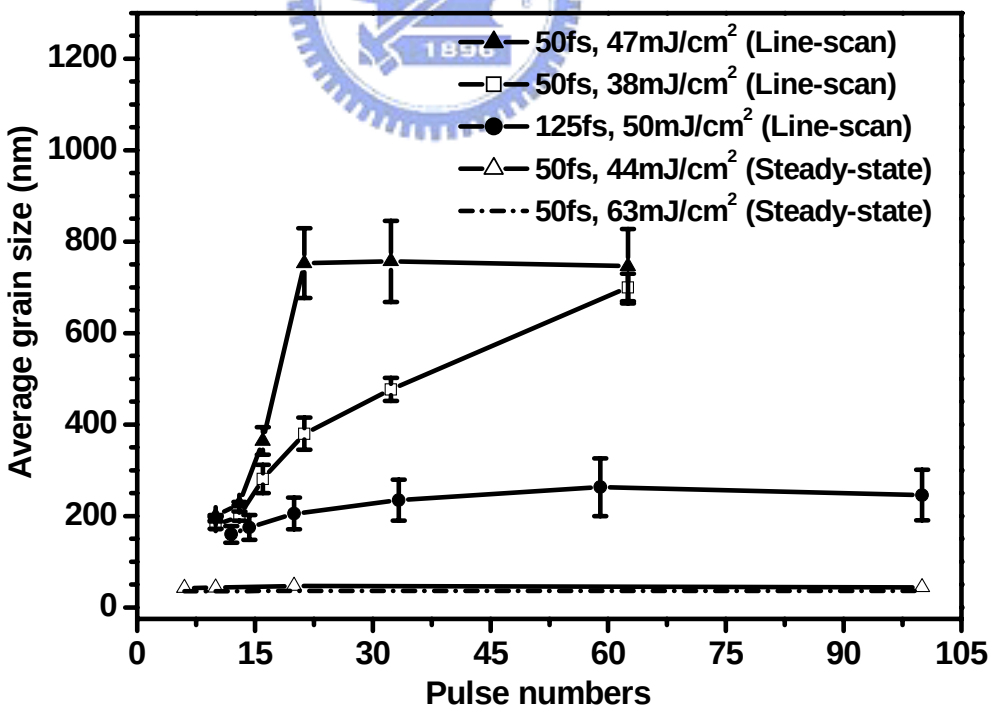

Fig. 2-8 Average grain sizes of FLA pc-Si films, irradiated with pulses of different durations, as a function of interpulse overlapping for steady-state FLA and scanned FLA.

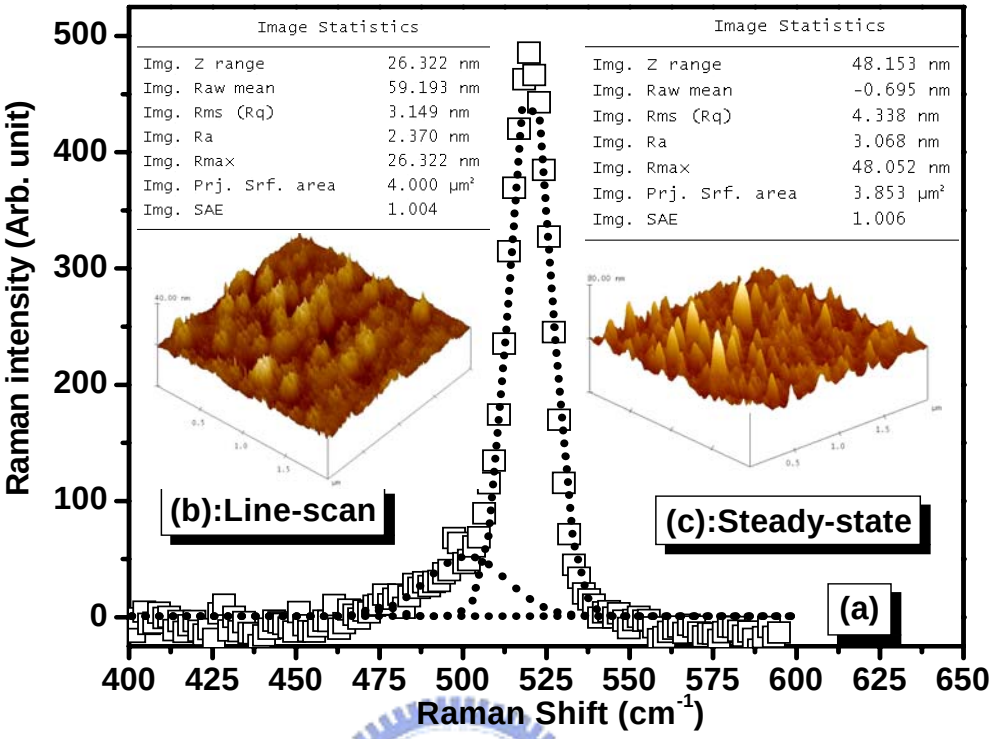

Fig. 2-9 (a): Raman spectra, and (b, c): AFM images, of FLA pc-Si films irradiated with 50 fs pulses. Line-scan (steady-state) mode is performed using E_L of 46 mJ/cm^2 (60 mJ/cm^2) and overlapping of 95 % (20 laser-shots).

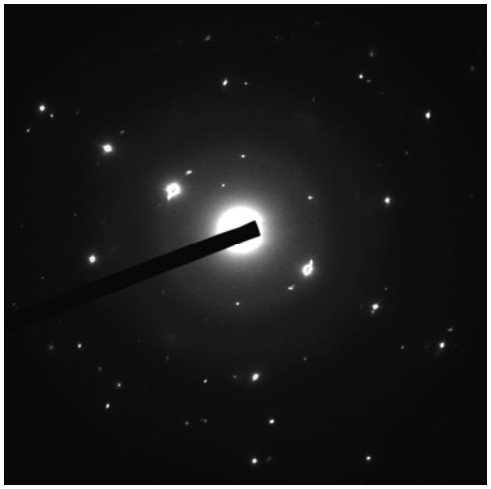

Fig. 2-10 TEM diffraction patterns of FLA-processed poly-Si films irradiated with 50 fs pulses.

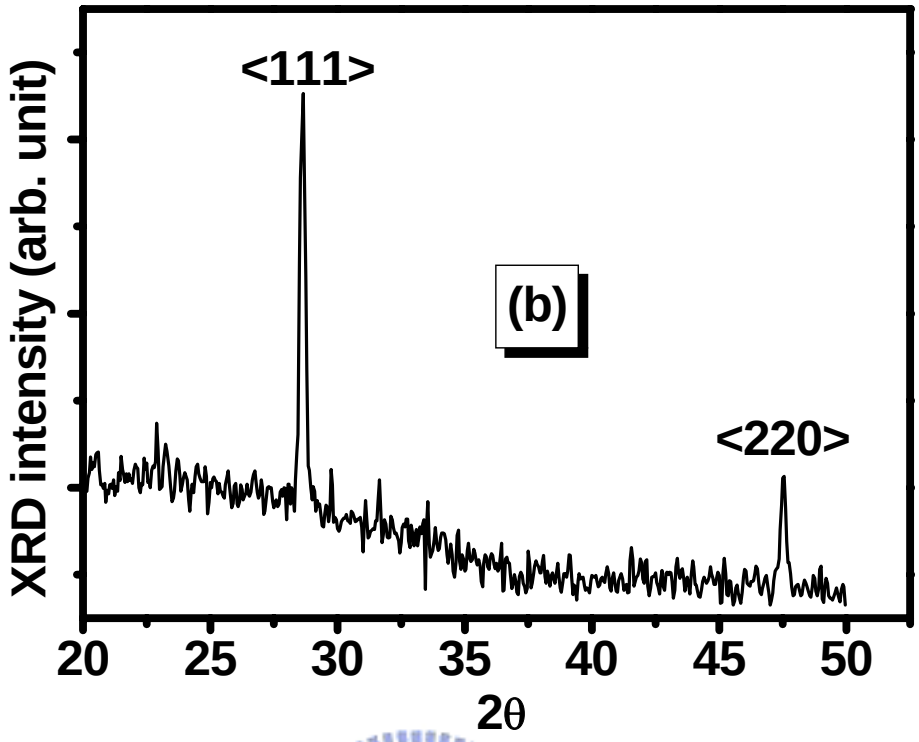

Fig. 2-11 XRD spectra of FLA-processed poly-Si films irradiated with 50 fs pulses.

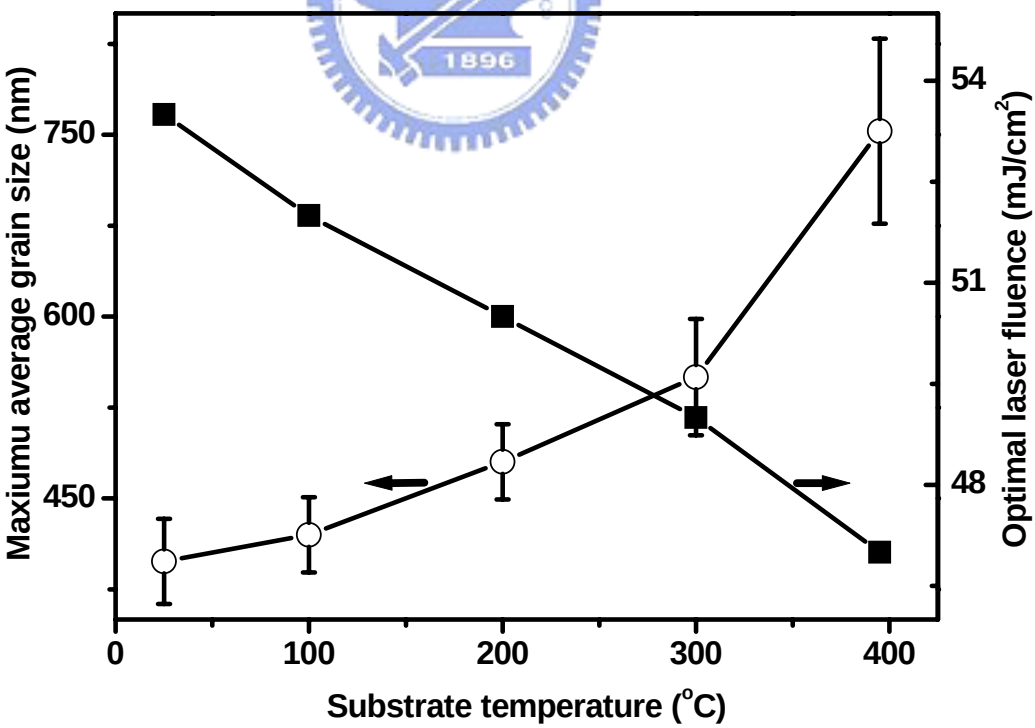

Fig.2-12 Maximum average grain size of FLA pc-Si films, and corresponding optimal laser fluence, as a function of substrate temperature.

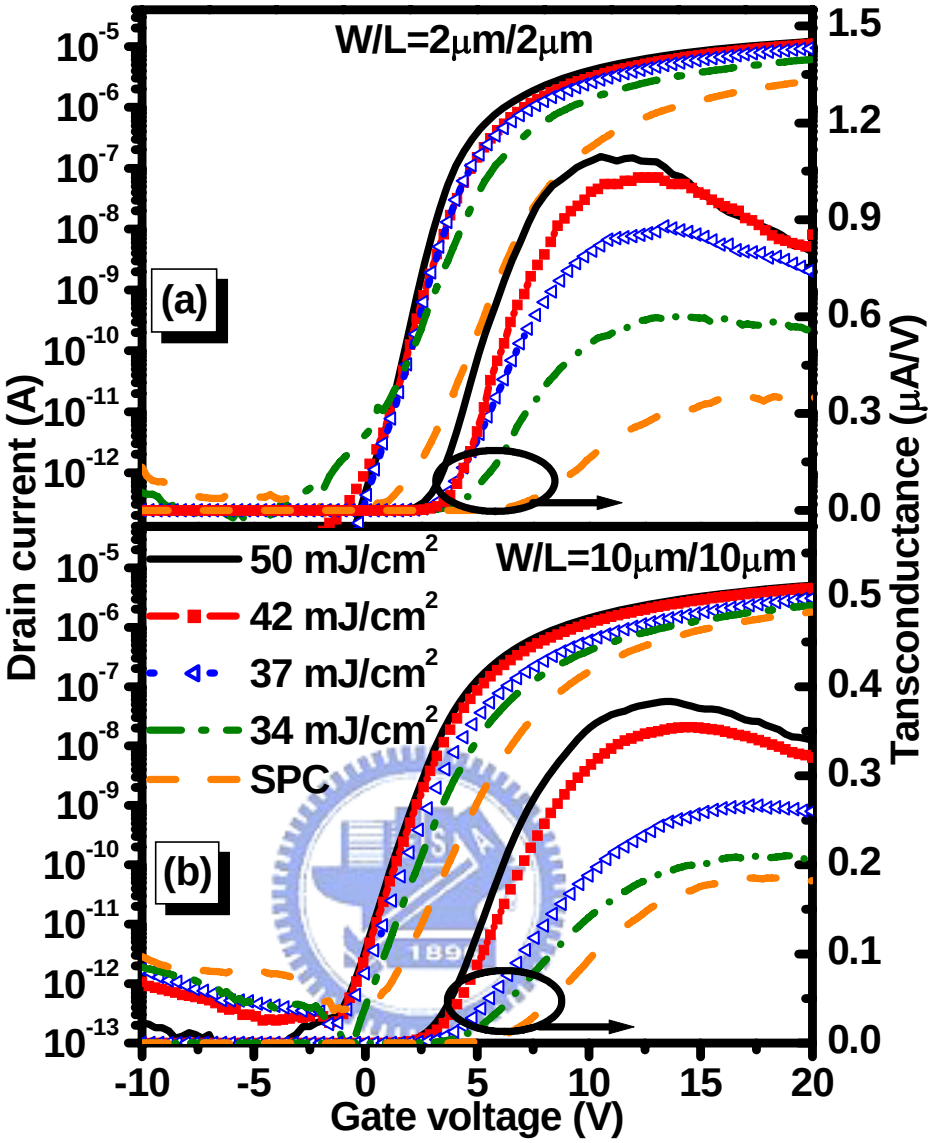

Fig. 2-13 Transfer characteristics and transconductance versus gate voltage for FLA and SPC processed TFTs with channel dimensions of (a) W = L= 2 μm and (b) W = L= 10 μm.

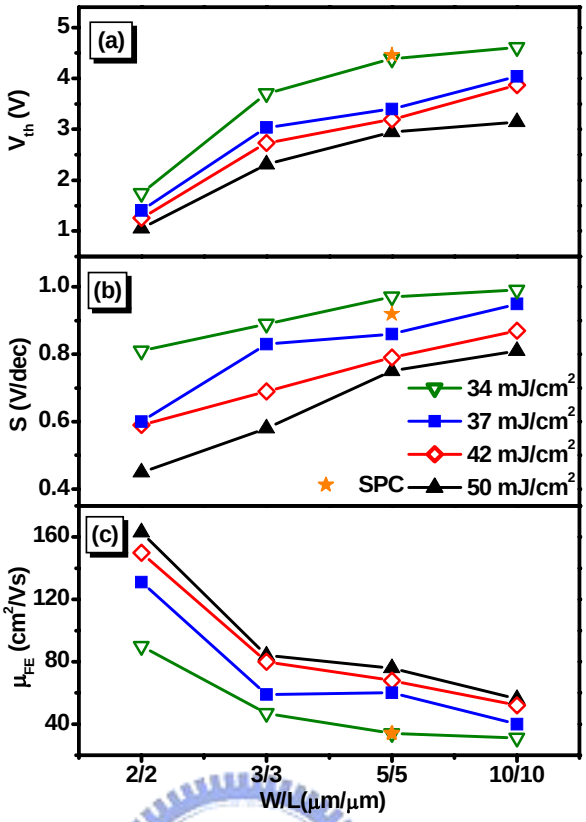

Fig. 2-14 (a) Threshold voltages, (b) subthreshold slopes and (c) mobilities for TFTs annealed by FLA with different fluences and SPC process.

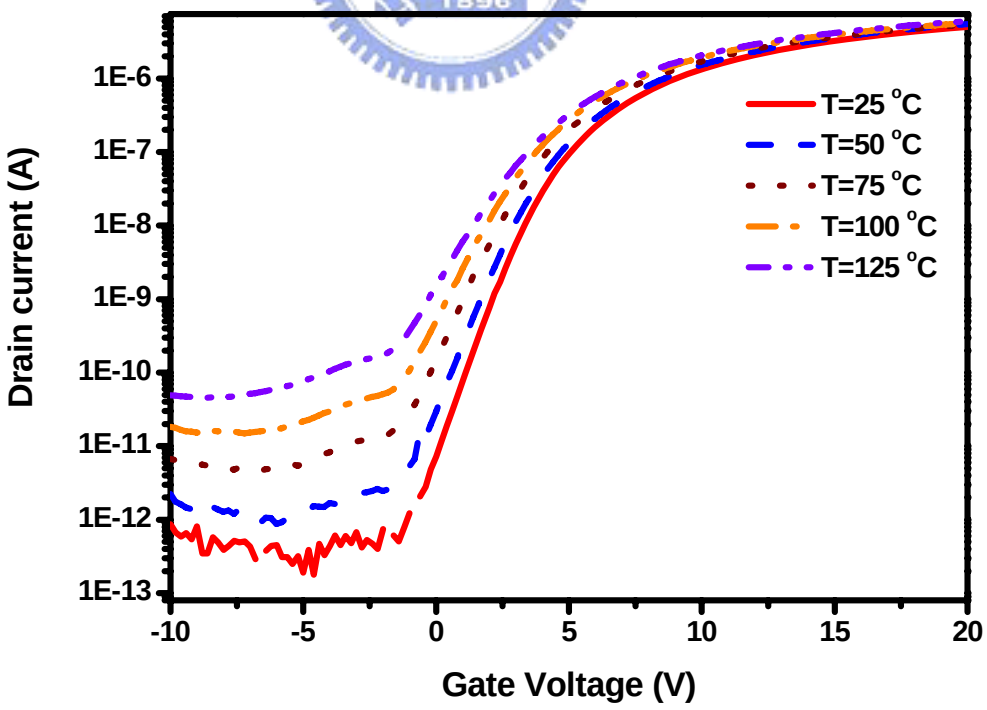

Fig. 2-15 Transfer characteristics of the sample (W = L = 5 μm) measured at different temperatures.

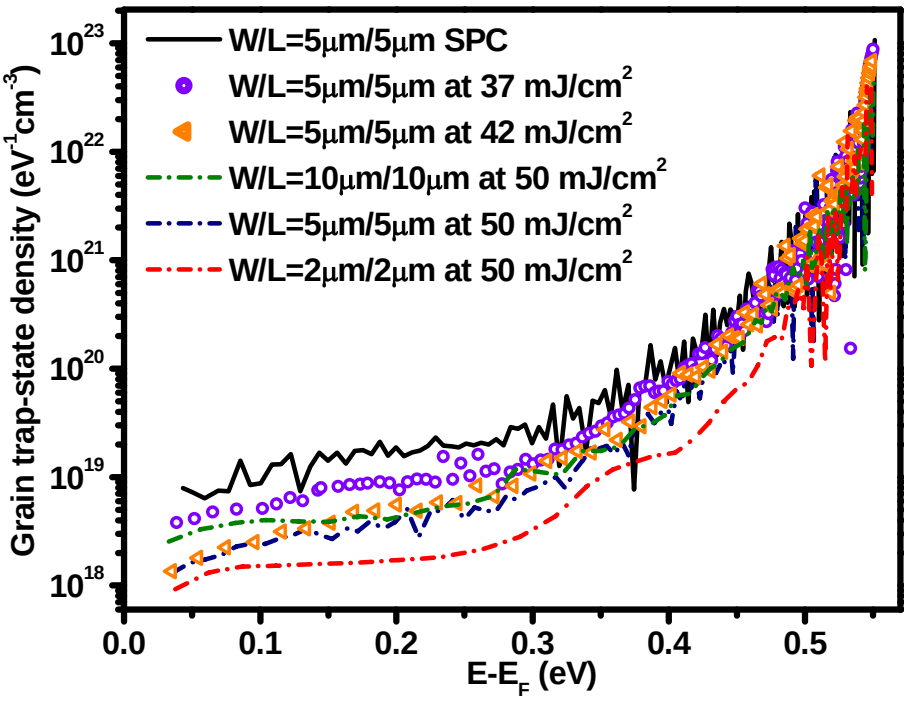

Fig. 2-16 Grain trap-state density in the energy bandgap of the FLA and SPC processed TFT with different channel dimensions and fluences in compare with furnace annealed TFT.

Tables

Wavelength	800nm
Pulse width	50fs
Repetition rate	1kHz
Beam diameter	15mm
Pulse Energy	2mJ
Polarization	Horizontal, linear

Table. 2-1 Output characteristics of Ti:Sapphire regenerative amplifier.

	FLA	Single shot ELA	Multi-shots ELA	SLS ELA	Green pulse laser annealing ($Nd:YVO_4$)	Green CW laser annealing
Crystallization mode	SLS-like	SLG	SLG	SLS	SLS	CW-lateral crystallization
Optimal E_L (mJ/cm^2)	~45	150-250	150-450	~900	>1500	
Maximum of average grain sizes (μm)	~0.8	~1	~0.3	~10	~100x0.5	~20x3
Numbers of laser-shots	>20	1	10-100	~70	~20	
Total input energy (J/cm^2)	~0.9	>0.15	~10	~60	>30	>10

Table. 2-2 Comparison of characteristics and performances for silicon films crystallized by FLA herein with those obtained by other annealing methods.

Chapter 3

Dopant Profile Engineering by Near-Infrared Femtosecond Laser Activation

3.1 Introduction

Much effort has been focused on the formation of thin insulators, short channels, and shallow junctions [1] by dopant profiling [2-8] for scaling of transistor-based silicon devices to ~100 nm. State-of-the-art dopant profile engineering has been achieved by integrating low-energy implantation [2-4], defect engineering [5-8] and fast solid-phase-epitaxial-regrowth [4, 6] or laser annealing [6-8]. To date, dopant profile engineering still faces challenges such as boron-enhanced diffusion (BED) [2], transient-enhanced diffusion (TED) [3-4], boron-interstitial clustering [4], and uphill diffusion [5, 8-9]. All of the above are associated with thermal energy supplied during dopant activation.

Due to fast delivery of thermal energy by absorption of nanosecond laser pulses, activation by excimer laser annealing [6-8, 10-12] (ELA) can more effectively minimize dopant diffusion than furnace annealing (FA) [6, 11] and spiked rapid thermal processing (RTP) [6, 9, 10, 13]. Nevertheless, dopant diffusion during ELA-based activation is not eliminated altogether. This is generally attributed to both vacancy-mediated [5, 8-9] and interstitial-mediated diffusion [2-4] mechanisms that are enhanced by a rapid melting and solidification process.

In the last chapter, we reported femtosecond laser annealing (FLA) of amorphous silicon [14] (a-Si) using sub-100 fs pulses at 800 nm, at which wavelength a-Si is nearly transparent. Grain sizes as large as ~800 nm were obtained with a laser fluence as low as ~

45 mJ/cm^2. The annealing mechanisms were thought to be nonlinear absorption and ultrafast or non-thermal melting [15, 16] due to lattice weakening by photoexcited electronic systems. As a result, the thermal budget of FLA is greatly reduced with respect to that of conventional annealing schemes. This suggests that FLA could provide a new means of dopant profile engineering. In this work, we report the results of FLA-activated n-type (phosphorous or P) and p-type (boron or B) dopants confined in ultra shallow junction regions. Preamorphization by implantation is not required.

Not only the ultra-shallow formation in the silicon substrate was important, bulk germanium (Ge) gains attention since it offers significantly higher carrier mobility of both electron (~ 3900 cm^2/Vs) and hole (1900 cm^2/Vs) in comparison with silicon. High temperature (400-500 °C) activation by RTP has been applied on the fabrication of both n- and p-channel Ge MOSFETs [17]. However, the dopant loss and fast diffusion of dopant accompanied with activation of P-implanted Ge make it challenging to control both dopant concentration and dopant profile [17-19].

In order to reduce the dopant diffusion, dopant activation in Ge substrate by excimer laser annealing (ELA, pulse duration of 23 ns) was reported by Huang *et al* [20]. However, the step like dopant profiles of ELA-processed samples, which extend deeper as the laser fluence and number of laser pulses increased, suggest the limit of thermal activation process. Using femtosecond laser pulses, ultrafast or non-thermal melting of the sample surface rather than heat penetration due to thermal conduction is expected to lead to a thinner melting depth in FLA-annealed samples [15-16]. In this chapter, n-type (P) and p-type (B) dopants in Ge activated by FLA was firstly studied.

3.2 Experiment setup and procedures

We employed a 1-kHz Ti:sapphire regenerative amplifier (λ=800 nm), generating 50 fs pulses, and the line-scan FLA method which has been shown in the last chapter to activate

P- or B-implanted Si substrates. The beam spot size was 3mm×150μm. During the scanning process, the overlapping of neighboring pulses was fixed as 92.5-97.5 %. To compare, preamorphization implantation (PAI) by Si^+ as well as the use of BF_2^+ instead of B^+ for implantation were employed for some of the samples. ELA-activation experiments using a KrF laser (λ=238 nm) were also conducted. The samples and processing parameters studied are summarized in Table 3-1.

Dopant profiles for activated and as-implanted samples were analyzed by secondary ion mass spectrometry (SIMS) and spreading resistance profiling (SRP) for assessment of the active and retained dose. Sheet resistances of all samples were measured by using a four-point probe. Atomic force microscopy (AFM) was used to inspect the surface roughness.

For the activation of Ge in this study, the Ge wafer of p-type (100) and n-type (003) were used. Room-temperature implantations at a fixed dose of 5×10^{15} /cm^2 were carried out by ion implanter. BF_2 ions with 30 keV were used to form p^+ junctions in n-Ge, while 50 keV P ions were employed to make n^+ junctions in p- Ge. The chemical concentration profiles for activated and as-implanted samples were analyzed by SIMS. AFM was also used to inspect the surface roughness. Sheet resistances of all samples were measured by using a four-point probe. The electrically active dopant concentrations and carrier mobility were obtained by Hall measurements..

3.3 Results and Discussions

3.3.1 Material Characterization of Femtosecond Laser Activated Si

3.3.1.1 Secondary Ion Mass Spectroscopy Analysis

Figure 3-1 shows SIMS profiles of borons in B-implanted layers without (sample A) and with PAI (sample B) as well as BF_2^+-implanted layers (sample C). Junction depths for the three as-implanted samples were designed to be 270, 200, and 100 nm, respectively. The

SIMS and SRP profiles of boron in low-energy B-implanted layers (sample C) are shown in Fig. 3-2. In Fig. 3-3, we present SIMS and SRP profiles of phosphorus in low-energy P-implanted layers with a junction depth of 100 nm (sample D). Laser fluences required for activating all the samples were found to be 27-39 mJ/cm^2, versus ~ 45 mJ/cm^2 for FLA-crystallization of a-Si films. These data together with those of ELA–activated samples as well as reported values for RTP-activated [6] samples are also listed in Table 3-1 for comparison. The overlapping of neighboring pulses in Fig.3-1, 3-2, and 3-3 were 95%.

After FLA-activation at room temperature (24 °C), dopant profiles of all activated samples were found to be almost the same as those of as-implanted ones (See Figs 3-1 and 3-2). No flat-top profiles were observed in regions of highly-concentrated dopants, as opposed to the cases for activation by ELA [6-8, 10-12]. This likely implies the absence of dopant redistribution by FLA-activation. The total laser fluence (20 laser shots) required for FLA-activation is 0.5 J/cm^2, much lower than that for ELA-activation (~ 5-10 J/cm^2) [7, 10]. Either linear or nonlinear absorption of near-infrared laser photons by implanted samples is not expected to reduce the required activation fluence. The low fluence required for FLA-activation thus suggests that ultrafast or non-thermal melting of semiconductors is the dominant mechanisms [15-16].

Irradiated by femtosecond pulses that photoexcited a large enough fraction of the valance electrons in the semiconductor, the lattice is weakened and structural change can occur while the electronic systems of the lattice are not in thermal equilibrium with each other. Such a non-thermal melting mechanism could minimize dopant diffusion significantly by reducing the thermal budget of activation.

For FLA-activation of samples at room temperature, we show in Fig. 3-1 that dopant-diffusion after activation is negligible in samples A and B. The situation is dramatically different when we examine dopant profiles of B-doped samples with the shallowest implantation depth (sample C). The peak position in B-dopant profile of sample

C after FLA-activation shifts by about 10 nm with respect to that of as-implanted sample C. This is independent of the substrate temperature up to 200 °C.

We also observed uphill diffusion towards the surface by ~ 10 nm for sample C at profile depth beyond ~ 60 nm. Uphill diffusion is more apparent at elevated substrate temperatures. In samples A and B, on the other hand, no uphill diffusion was observed. We note that uphill diffusion in dopant profiles for silicon activated by other methods often occurs at a depth as shallow as 10 nm [5, 8, 22]. For P dopant profiles in sample D without substrates heating (see Fig. 3-3), uphill diffusion at a depth of 60 nm is barely observable, whereas P atoms diffuse away from the surface by ~ 10 nm at elevated temperatures.

In Fig. 3-2, we show the flat-top profiles of ELA-activation for sample C at 24 and 200 °C. Uphill diffusion phenomena in ELA-activated samples C and D are not observed as shown in Figs. 3-2 and 3-3. It is obvious that in the melting regime ELA delete any effect of temperature difference.

Using femtosecond laser pulses, ultrafast or non-thermal melting of the sample surface rather than heat penetration due to thermal conduction [16] is expected to lead to a thinner melting depth in FLA-annealed samples. This limits the activation depth and thus prevents thermally-assisted diffusion of end-of-range (EOR) defects further away from the surfaces. As a result, trapped interstitials will remain within the EOR regions for FLA, accomplishing the functionality of PAI in ELA [5, 8].

Recently, Duffy et al. [5, 22] reported that uphill diffusion during low-temperature (700 °C) furnace annealing was driven by an interstitial gradient between the EOR region and high-concentration portion of the dopant profile [22]. This gradient is steeper when the distance between the two regions is reduced by PAI control or if the amorphous-crystalline (a/c) interface is shallow. As a result, a high concentration of boron interstitial pairs is likely to form during annealing [5]. Boron atoms move appreciably toward the surface consequently. The a/c interface for samples C and D with implanted depth of 100 nm is

much closer to the surface than that for samples A and B with implanted depth of 200-270 nm. The former two samples are thus expected to be influenced more by the FLA-induced PAI-like effects than the latter two samples. This picture is consistent with our experimental data.

Heating of the samples during activation is expected to render the interstitials more mobile [6]. For BF_2^+-doped layers, elevated substrate temperature likely facilitates the generation of more boron-interstitial pairs, thereby promoting B uphill diffusion [5]. Uphill diffusion of P atoms in shallow P-implanted layers FLA-activated at elevated substrate temperature was not observed (see Figs. 3-2 and 3-3). The diffusivity of P-atoms doped in Si is much higher than that of B-atoms [23] and plays a major role in the observation of different behavior for B and P. This picture is also consisted with observation that the dopant profile of the P-implanted layers is broader than that of the BF_2-implanted sample for ELA-activation.

Surface roughness is a key parameter of laser activated sample since it will affect the electrical characteristics of devices. The AFM results of FLA-activated Si (B- and P-implanted) are shown in Fig. 3-4 and 3-5. AFM analysis showed that the root-mean-square surface roughness of FLA-activated samples which varied from 2.1-6.8 nm is not exactly related to laser fluence or pulse number. This surface roughness is close to that of ELA-activated samples.

3.3.1.2 Electrical Characterization of Femtosecond Laser Activated Si

The sheet resistances of sample C and D irradiated with different number of laser shots are shown in Fig. 3-6 and 3-7. Sheet resistances for all FLA-activated samples were in the range of 10^2-10^5 Ω/□. For device applications, the sheet resistance should be lower than 500Ω/□. The lowest sheet resistance obtained by FLA is essentially the same as those reported for activation of B and P by other methods in the literature [6, 7, 11]. These results

confirmed that FLA has highly potential for application.

Electrical profiling (SRP) of active B and P in samples C and D were conducted and shown in Figs. 3-2 and 3-3. Increasing the substrate temperature from 24 to 200 °C, the activation efficiency (dose activated/dose implanted) of sample C (D) increases from 28 (31) to 33 (36) %. At the same time, the sheet resistance of sample C (D) decreases from 450 (325) to 225 (225) Ω/□. These values are similar to reported ELA results [10-11]. Uphill diffusion of boron atoms is also apparent in SRP curves for sample C FLA-activated at 24 and 200 °C (see Fig. 3-2).

One might consider comparing non-melting ELA performed at 200 °C with FLA at the same temperature. According to Poon *et al*. [7], for ELA without melting, boron exhibits negligible diffusion during each pulse and the sheet resistance values could not be measured by the four-point probe because the values were too high. That is, activation by non-melting ELA is ineffective, while we have shown FLA-activation is very successful.

Since the thin activation depth of FLA prevents thermally-assisted diffusion of end-of-range (EOR) defects further away from the surfaces, trapped interstitials will remain within the EOR regions for FLA. This model is corroborated by the observation of a steep slope around the depth of 50-70 nm for the observed SRP profiles.

3.3.2 Material Characterization of Femtosecond Laser Activated Ge

3.3.2.1 Secondary Ion Mass Spectroscopy Analysis

Figure 3-8 and 3-9 show SIMS profiles of phosphorous in P-implanted layers activated with different laser pulses and fluences. With a junction depth of 40 nm, the SIMS profiles of boron in BF_2-implanted layers activated with different laser pulses and fluences are shown in Fig. 3-10 and 3-11.

Figure 3-8 shows the phosphorus SIMS profiles in the substrate after laser irradiation at a fixed fluence (35 mJ/cm^2) with different number of laser pulses. No steplike profiles were

observed in regions of highly-concentrated dopants, as opposed to the cases for activation by ELA [20]. This implies the mainly difference of non-thermal melting by FLA-activation and thermal process by ELA [14-16]. For the FLA-activation with 5 laser pulses, the phosphorous profile is almost identical to that of as-implanted samples. Uphill diffusion outside the highly concentrated regions at a depth of 35-50 nm towards the surface is firstly observed in Ge activation.

However, P atoms of the samples activated with 10 and 20 pulses diffuse away from the surface by ~ 10 nm. Calculating from SIMS profiles, the phosphorous concentration of as-implanted sample (4.27×10^{15} atoms/cm^2) is close to that of FLA-activated samples (4.1×10^{15}-4.5×10^{15} atoms/cm^2). This implies the significant outdiffusion (~ 50%) which is frequently observed in both RTP and ELA process, can be eliminated in FLA-activation [17-20].

The phosphorous SIMS profiles of FLA activation by different fluences are shown in Fig. 3-9. The total laser fluence required for FLA-activation is 0.18 J/cm^2, slightly lower than that for ELA-activation (0.32 J/cm^2) [20]. As the laser fluence increased from 35 to 45.5 mJ/cm^2, diffusion of ~ 5 nm away from the surface was observed in the depth of 20-50 nm. It has been published by Satta et al. that the P atom diffusivity is strongly concentration dependent at high-concentration regions (above 2×10^{19} atoms/cm^3) [19]. This diffusion enhancement which is slightly observed at high-concentration regions in Fig. 3-9 may be related to the vacancy-assisted diffusion [24].

AFM analysis showed that the root-mean-square surface roughness of FLA-activated samples which varied from 2.8-5.4 nm is not exactly related to laser fluence or pulse number. This surface roughness of FLA-activated samples is slightly better than that of ELA activated samples [20].

Figure 3-10 and 3-11 depicts the boron dopant profiles of BF_2-implanted samples activated by FLA process. As opposite to silicon, boron exhibits as a very slow diffuser in

germanium [26]. Uphill diffusion which was previously observed in activation of dopants on Si substrate is not observed [5, 7]. B diffusion, which is proportional to the irradiated laser pulses, was observed in the area shallower than 10 nm (Fig. 3-10). Dopant diffusion manifested in the shallow area (<10 nm) of Fig. 3-11 is probably because implantation with heavy dopants (BF_2) will induce serious damage to the lattice in shallow area, however, light dopants (P) can penetrate and make damage to deeper area.

3.3.2.2 Electrical Characterization of Femtosecond Laser Activated Ge

In order to prove the electrical activity, the corresponding sheet resistances and hall mobility of the samples shown in the figures are also shown as the insets of Fig. 3-8 to 3-11. Here we are not going to measure the activated dopant profile by SRP. The resolution of SRP is about 7-8 nm, which is not precise enough for the shallow junction herein. The activation parameters and measurement results are summarized in Table 3-2.

The inset of Fig. 3-8 shows that the sheet resistance decreased because of irradiated with more laser pulses is identical to the improvement of hall mobility. As the irradiated laser pulses increased from 5 to 20, the corresponding activated dopant concentration slightly decreased from 3.01×10^{14} to 1.26×10^{14} atoms/cm^2 could be imputed to the dopant diffusion. Despite the reduced active concentration, one possible explanation for the improvement of sheet resistance and mobility could be the improvement in crystal quality. Here we measured a highest mobility of 993 cm^2/Vs.

As the laser fluence increased from 35 to 45.5 mJ/cm^2 (see Fig. 3-9), the activated dopant concentration slightly decreased from 3.01×10^{14} to 2.42×10^{14} atoms/cm^2 due to increased activation fluence. The corresponding huge improvement of electrical characteristics (815-1410 cm^2/Vs) may mainly attribute to the improvement of crystal quality [18].

The best activation rates which correspond to the lowest sheet resistance of the

samples in Fig. 3-9 are ~7%. The profile of P in Fig. 3-8 and 3-9 exhibits a concentration peat of about 2×10^{21} atoms/cm^2, which is already above the maximum equilibrium solubility of P in germanium and would not improve the sheet resistance [25]. The highest hall mobility is even higher than that of ion-implanted Ge samples activated by RTA (~ 920 cm^2/Vs) [18].

The peak concentration of boron atoms enormously increased from 4.97×10^{21} to 1.17×10^{22} atoms/cm^3 at a depth of ~ 6 nm as the diffusion enhanced by irradiated with more laser pulses (see Fig. 3-10). Since the solid solubility of boron in Ge is ~ 5×10^{18} atoms/cm^3, more atoms piled up at that depth is not able to further increase B activated concentration which is just 1.41×10^{14} atoms/cm^2 [15]. Thus the incremental of mobility from 121 to 330 cm^2/Vs could be attributed to the better crystallinity.

The activation of boron atoms with 5 laser pulses and various laser fluences show better performance in both electrical characteristics and diffusion suppression (Fig. 3-11). Mobility increased from 107 to 426 cm^2/Vs due to increasing irradiated laser fluence from 28 to 35mJ/cm^2. The improvement of sheet resistance and mobility, however, could be attributed to the incremental of activated carrier concentration from 1.05×10^{14} to 5.25×10^{14} atoms/cm^2 and crystallinity improvement. The highest activation rates of the dopants here is ~ 22%. This value is slightly lower than our previous results of dopant activation in Si with implantation energy of 25 keV.

3.4 Summary

Femtosecond laser annealing (FLA) was employed for activation of P - and B -implanted silicon with negligible dopant diffusion. Preamorphization by implantation, commonly used in conventional activation schemes for minimizing the diffusion of dopant during annealing, was found not to be required. We found that dopant profiles in FLA-activated samples essentially duplicate those of as-implanted ones even for junctions

as deep as 100 nm below the surface. The measured sheet resistances and activation efficiencies of P- and B-implanted samples were in the range of 100-400 Ω/□ and 28-35 % respectively.

Moreover, thermal-energy-assisted dopant diffusion by heating was observed for substrate temperature as low as 100 °C (Fig. 3-3). The shallow activated-depth feature associated with FLA reduces the separation between end-of-range defects and high-concentration portion of dopants. This generates a steep interstitial gradient responsible for observed B and P uphill diffusion at a depth of about 60 nm below the surface.

Excellent dopant profile controlling of n-type and p-type dopants on Ge substrate by femtosecond laser annealing was demonstrated for the first time. The fast delivery of photon energy, non-thermal melting, is the key feature of such intense ultrafast laser annealing process. Significant dopant loss, which is frequently observed in RTA and laser thermal activation, can be eliminated thus. Shallow junction formation (17, 40 nm) and high mobility (425, 1410 cm^2/Vs) of BF_2- and P-implanted samples are both reached by activated with appropriate laser fluence and laser pulses. This high mobility could be attributed to the high activation rate or the improvement of crystallinity.

References

[1] S. M. Sze, Semiconductor Devices physics and Technology.

[2] A. Agarwal, H. J. Gossmann, D. J.Eaglesham, S. B.Herner, A. T. Fiory, and T. E. Haynes, "Boron-enhanced diffusion of boron from ultralow-energy ion implantation," Appl. Phys. Lett., vol. 74, pp. 2435-2437, 1999.

[3] L. S. Robertson, M. E. Law, K. S. Jones, L. M. Rubin, J. Jackson, P. Chi and D. S. Simons, "Correlation of end-of-range damage evolution and transient enhanced diffusion of boron in regrown silicon," Appl. Phys. Lett., vol. 75, pp. 3844-3846, 1999.

[4] A. Agarwal, H. J. Gossmann, D. J. Eaglesham, L. Pelaz, D. C. Jacobson, T. E. Haynes and Y. Erokhin, "Reduction of transient diffusion from 1–5 keV Si^+ ion implantation due to surface annihilation of interstitials," Appl. Phys. Lett., vol. 71, pp. 3141-3143, 1997.

[5] R. Duffy, V. C. Venezia, A. Heringa, T. W. T. Husken, M. J. P. Hopstaken, N. E. B. Cowern, P. B. Griffin, and C. C. Wang, "Boron uphill diffusion during ultrashallow junction formation," Appl. Phys. Lett., vol. 82, pp. 3647-3649, 2003.

[6] Y. F. Chong, K. L. Pey, A. T. S. Wee, A. See, L. Chan, Y. F. Lu, W. D. Song and L. H. Chua, "Annealing of ultrashallow p^+/n junction by 248 nm excimer laser and rapid thermal processing with different preamorphization depths," Appl. Phys. Lett., vol. 76, pp. 3197-3199, 2000.

[7] C. H. Poon, B. J. Cho, Y. F. Lu, M. Bhat and A. See, "Multiple-pulse laser annealing of preamorphized silicon for ultrashallow boron junction formation," J. Vac. Sci. B, vol. 21(2), pp. 706-709, 2003.

[8] C. H. Poon, L. S. Tan, B. J. Cho, A. See and M. Bhat, "Boron Profile Narrowing in Laser-Processed Silicon after Rapid Thermal Anneal," Journal of The Electrochamical Society, vol. 151(1), pp. G80-G83, 2004.

[9] H. C. H. Wang, C. C. Wang, C. S. Chang, T. Wang, P. B. Griffin,and C. H. Diaz, "Interface induced uphill diffusion of boron: an effective approach for ultrashallow junction," IEEE Electron Device Lett., vol. 22, pp. 65-67, 2001.

[10] V. Privitera, C. Spinella, G. Fortunato and L. Mariucci, "Two-dimensional delineation of ultrashallow junctions obtained by ion implantation and excimer laser annealing," Appl. Phys. Lett., vol. 77, pp. 552-554, 2000.

[11] S. Baek, T. Jang and H. Hwang, "Two-dimensional delineation of ultrashallow junctions obtained by ion implantation and excimer laser annealing," Appl. Phys. Lett., vol. 80, pp. 2272-2274, 2002.

[12] S. Whelan, A. L. Magna, V. Privitera, G. Mannino, M. Italia,C. Bongiorno, G. Fortunato and L. Mariucci, "Dopant redistribution and electrical activation in silicon following ultra-low energy boron implantation and excimer laser annealing," Phys. Rev. B, vol. 67, pp. 075201-1 - 075201-8, 2003.

[13] L. Shao, X. Wang, I. Rusakova, H. Chen, J. Liu, J. Bennett, L. Larson, J. Jin, P. A. W. van der Heide and W. K. Chu, "Stability studies of ultrashallow junction formed by low energy boron implant and spike annealing," J. Appl. Phys., vol. 92, pp. 5788-5792, 2002.

[14] J. M. Shieh, Z. H. Chen, B. T. Dai, Y. C. Wang, A. Zaitsev, and C. L. Pan, "Near-infrared femtosecond laser-induced crystallization of amorphous silicon," Appl. Phys. Lett., vol. 85, pp. 1232-1234, 2004.

[15] S. K. Sundaram, and E. Mazur, "Inducing and probing non-thermal transitions in semiconductors using femtosecond laser pulses," Nature Materials, vol. 1, pp. 217-224, 2002.

[16] A. Rousse, C. Rischel, S. Fourmaux, I. Uschmann, S. Sebban, G. Grillon, Ph. Balcou, E. Förster, J. P. Geindre, P. Audebert, J. C. Gauthier, and D. Hulin, "Non-thermal melting in semiconductors measured at femtosecond resolution," Nature, vol. 410, pp.

65-68, 2001.

[17] H. Shang, K. -L. Lee, P. Kozlowski, C. D. Emic, I. Babich, E. Sikorski, M. Ieong, H. -S. P. Wong, "Self-aligned n-channel germanium MOSFETs with a thin Ge oxynitride gate dielectric and tungsten gate," IEEE Electron Device Lett., vol. 25, pp. 135-137, 2004.

[18] C. H. Poon, L. S. Tan, B. J. Cho, and A. Y. Du, "Dopant loss mechanism in n^+/p germanium junctions during rapid thermal annealing," J. Electrochem. Soc., vol. 152, pp. G895-G899, 2005.

[19] A. Satta, T. Janssens, T. Clarysse, E. Simoen, M. Meuris, A. Benedetti, I. Hoflijk, B. D. Jaeger, C. Demeurisse , and W. Vandervorst, "P implantation doping of Ge: diffusion, activation, and recrystallization," J. Vac. Sci. Technol. B, vol. 24, pp. 494-498, 2006.

[20] J. Huang, N. Wu, Q. Zhang, C. Zhu, A. A. O. Tay, G.Chen, and M. Hong, "Germanium n^+/p junction formation by laser thermal process," Appl. Phys. Lett., vol. 87, pp. 173507-173509, 2005.

[21] A. Rousse, C. Rischel, S. Fourmaux, I. Uschmann, S. Sebban, G. Grillon, Ph. Balcou, E. Förster, J. P. Geindre, P. Audebert, J. C. Gauthier, and D. Hulin, "Non-thermal melting in semiconductors measured at femtosecond resolution," *Nature*, **410**, 65-68 (2001)

[22] R. Duffy, V. C. Venezia, J. Loo, M. J. P. Hopstaken, M. A. Verheijen, G. C. J. Maas, Y. Tamminga, T. Dao and C. Demeurisse, "Low-temperature diffusion of high-concentration phosphorus in silicon, a preferential movement toward the surface," Appl. Phys. Lett., vol. 86, pp. 81917-81919, 2005.

[23] J. Xu, V. Krishnamoorthy, K. S. Jones and M. E. Law, "A comparison of boron and phosphorus diffusion and dislocation loop growth from silicon implants into silicon," J. Appl. Phys., vol. 81, pp. 107-111, 1997.

[24] S. Matsumoto and T. Niimj, “Concentration dependence of a diffusion coefficient at phosphorus diffusion in germanium,” Electrochem. Soc., vol. 125, pp. 1307- 1309, 1978.

[25] C. O. Chui, L. Kulig, J. Moran, W. Tsai and K. C. Saraswat, “Germanium n-type shallow junction activation dependences,” Appl. Phys. Lett., vol. 87, pp. 0919091-0919093, 2005.

[26] S. Uppal, A. F. W. Willoughby, J. M. Bonar, N. E. B. Cowern, T. Grasby, R. J. H. Morris, and M. G. Dowsett, “Diffusion of boron in germanium at 800 – 900°C,” J. Appl. Phys., vol. 96, pp. 1376-1380, 2004.

Figures

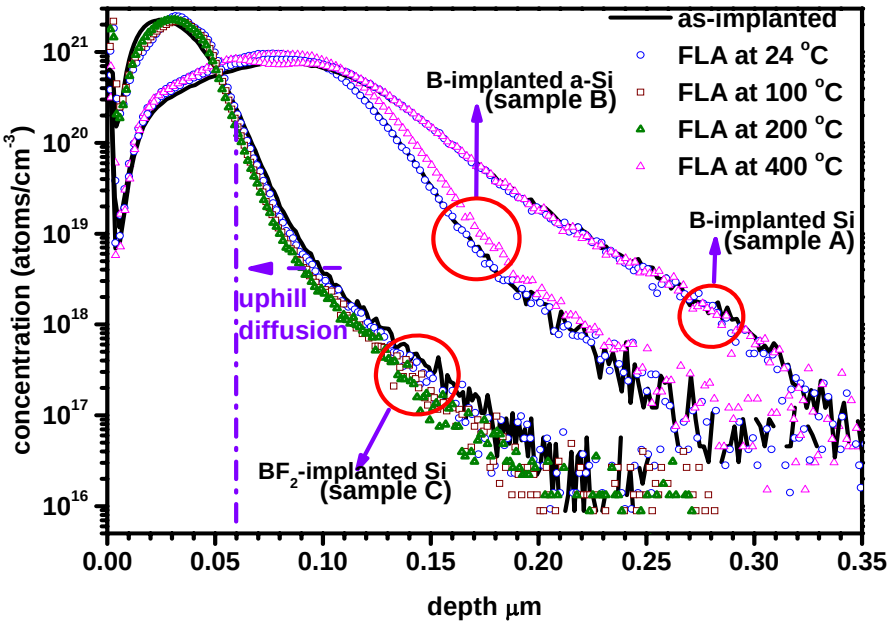

Fig. 3-1 SIMS profiles of as implanted B-doped samples, with (sample A) and without PAI (sample B) as well as BF_2^+-implanted samples (sample C). SIMS profiles for all B-doped layers activated by FLA at different substrate temperature are also shown.

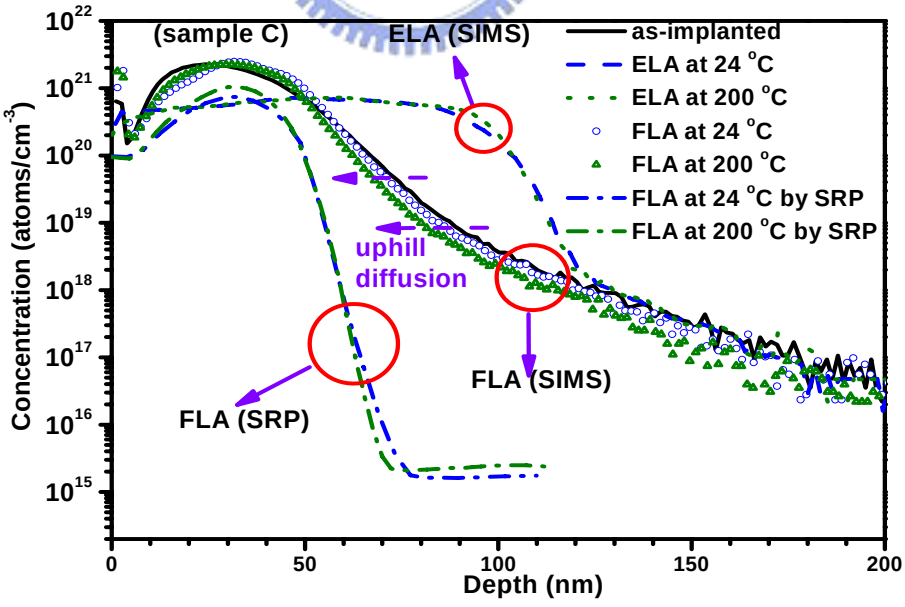

Fig. 3-2 SIMS profiles for BF_2^+-implanted layers activated by either FLA or ELA at different substrate temperatures. SRP profiles for BF_2^+-implanted layers activated by FLA at different temperature are also shown.

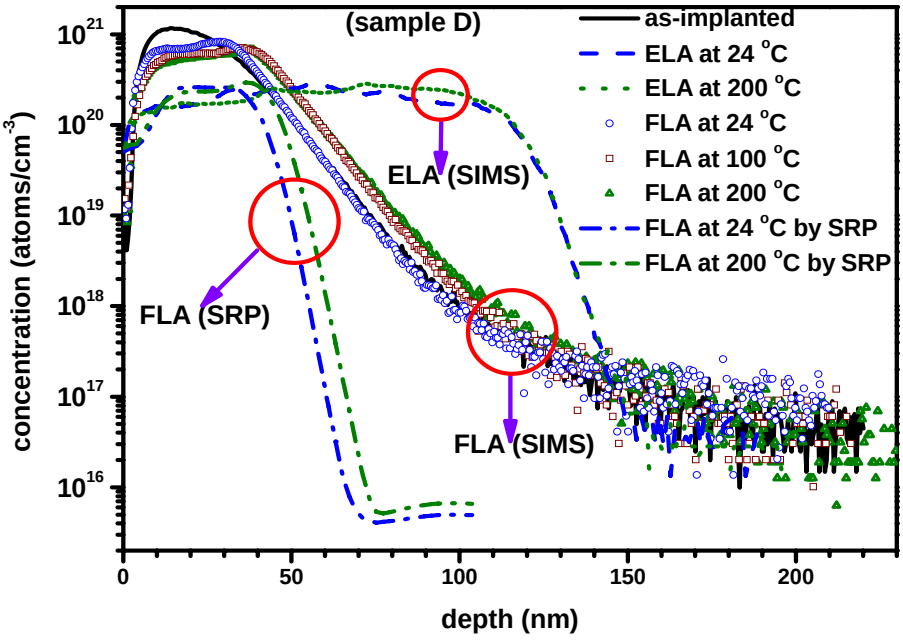

Fig. 3-3 SIMS and SRP profiles for P-implanted layers activated by FLA at different substrate temperatures. SIMS profiles for P-implanted layers activated by ELA at different substrate temperatures are also shown. The dopant depth was designed to be the same as for BF_2^+-implanted samples.

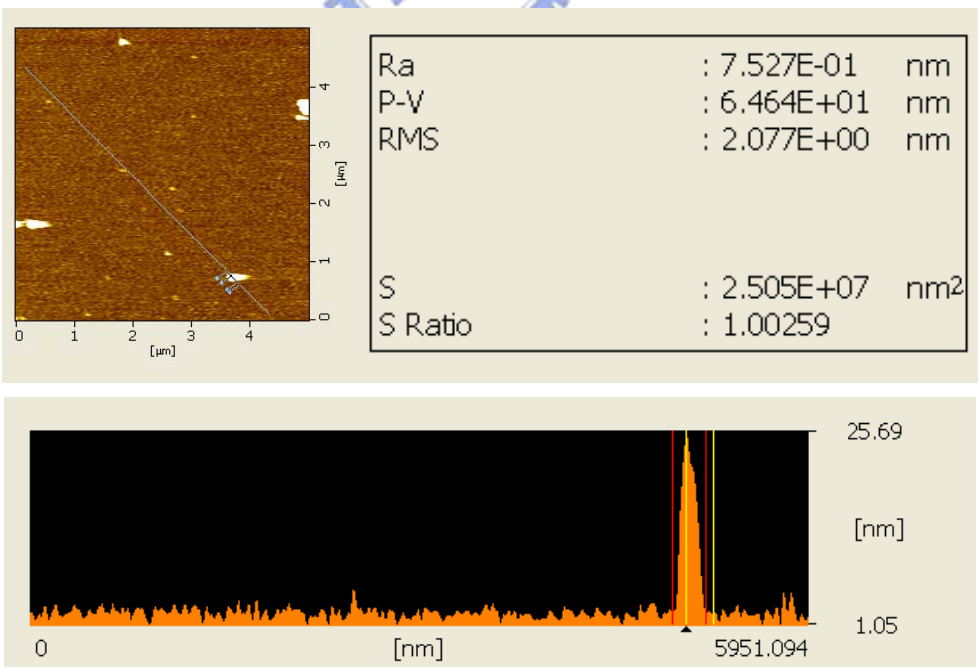

Fig. 3-4 AFM result of FLA-activated B-implanted Si.

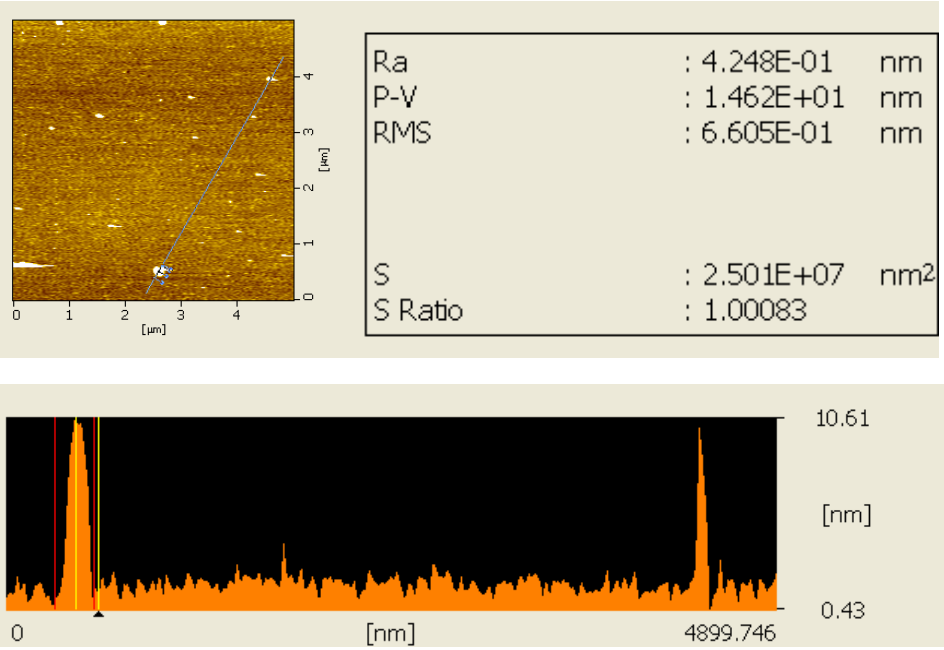

Fig. 3-5 AFM result of FLA-activated P-implanted Si.

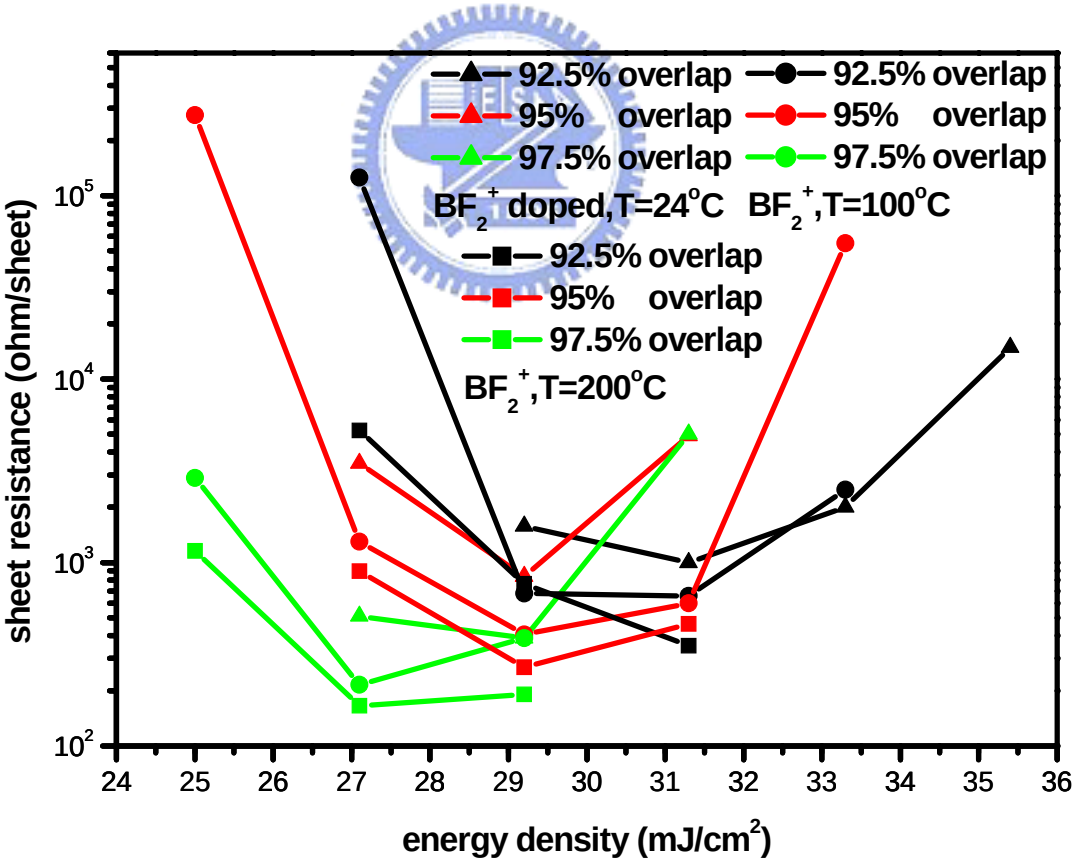

Fig. 3-6 Sheet resistance of sample C activated with different overlapping of neighboring pulses and different substrate temperature.

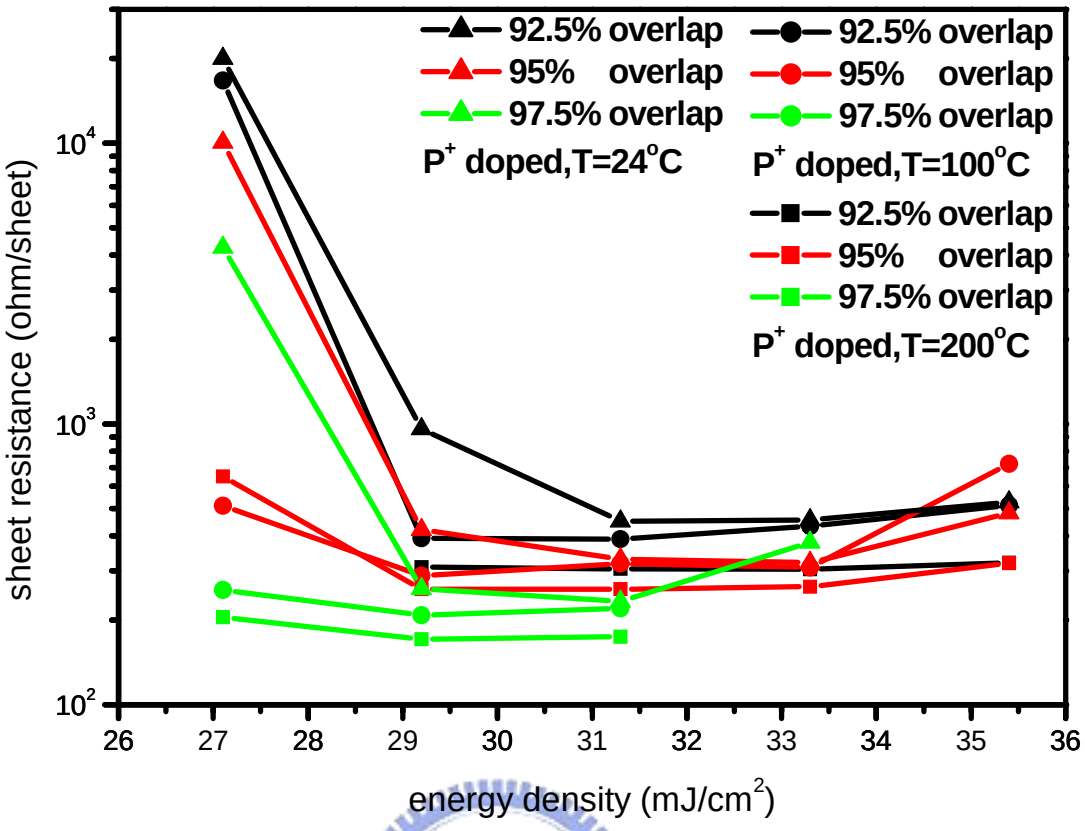

Fig. 3-7 Sheet resistance of sample D activated with different overlapping of neighboring pulses and different substrate temperature.

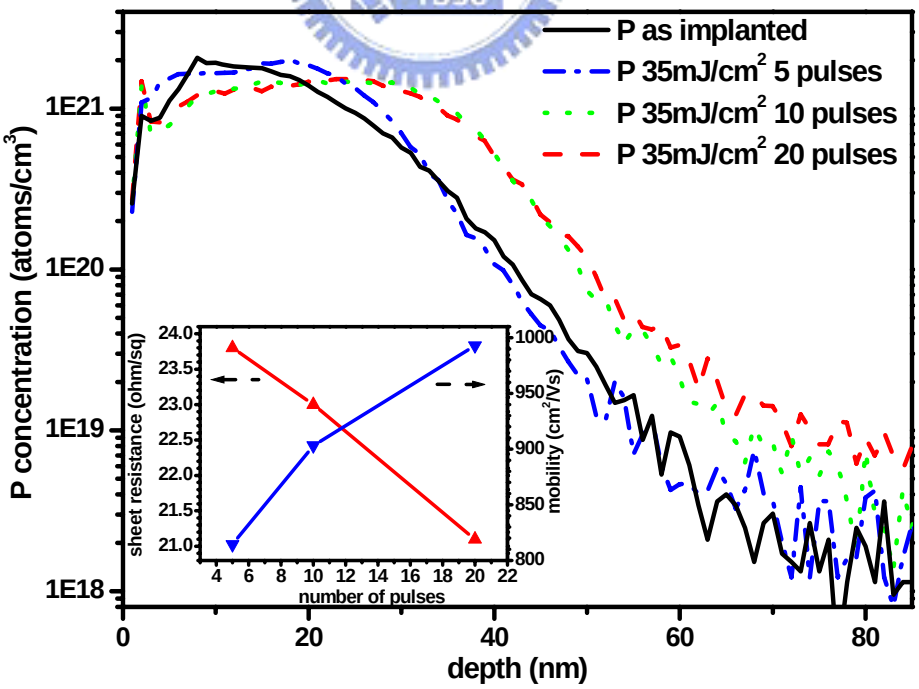

Fig. 3-8 Phosphorous SIMS profiles of the samples annealed with different number of laser pulses. The inset shows the corresponding sheet resistance and mobility of the samples.

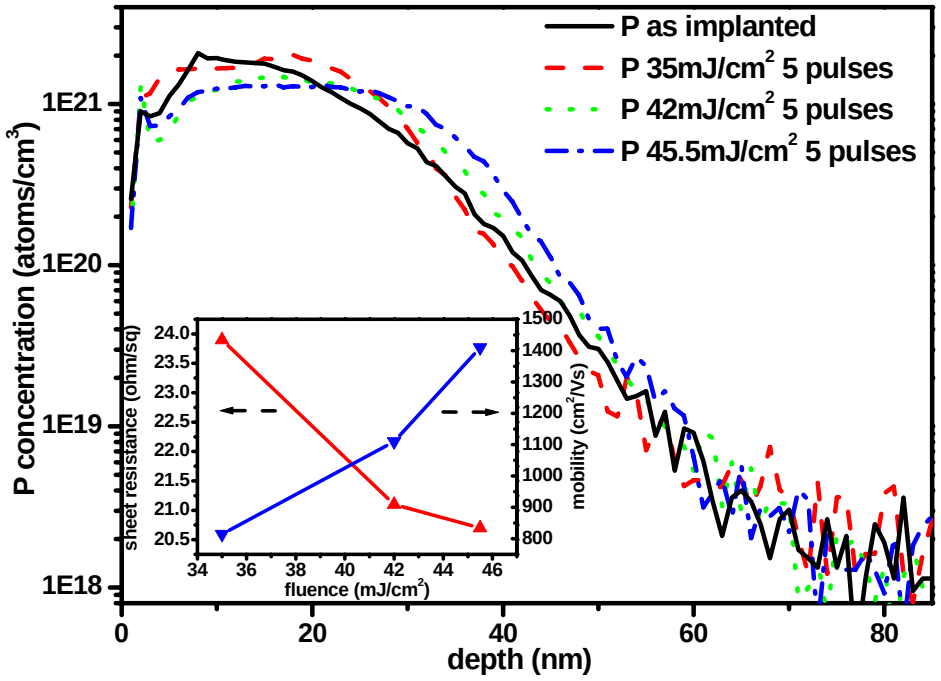

Fig. 3-9 Phosphorous SIMS profiles of the samples annealed with various laser fluences. The inset shows the corresponding sheet resistance and mobility of the samples.

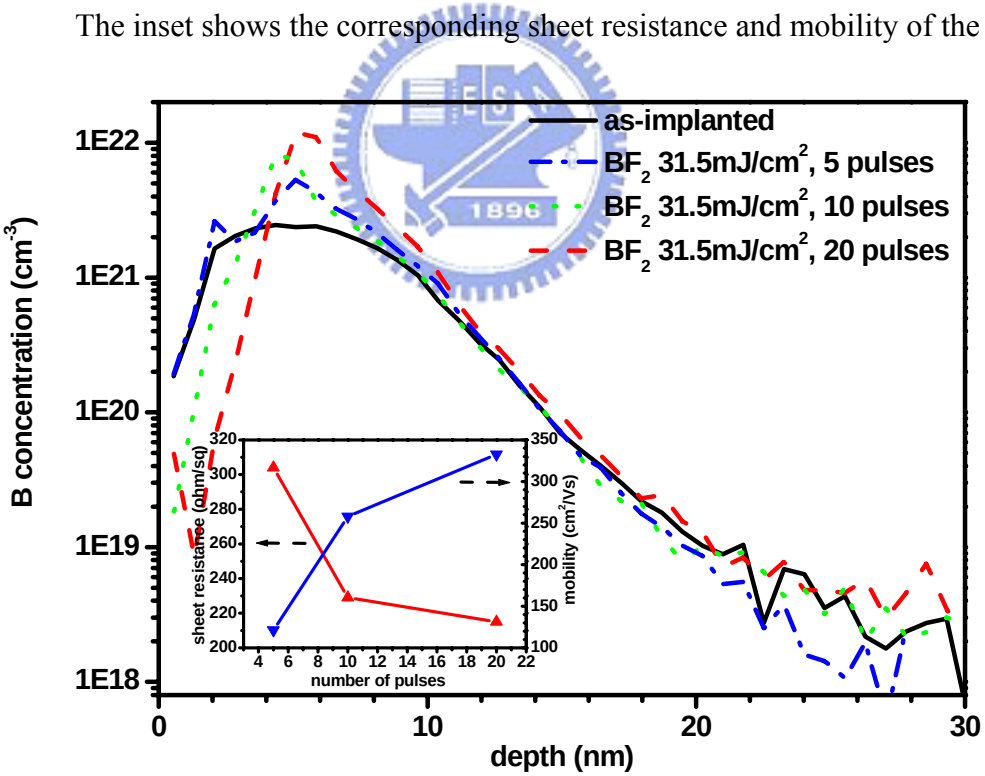

Fig. 3-10 Boron SIMS profiles of the samples annealed with various number of laser pulses. The inset shows the corresponding sheet resistance and mobility of the samples.

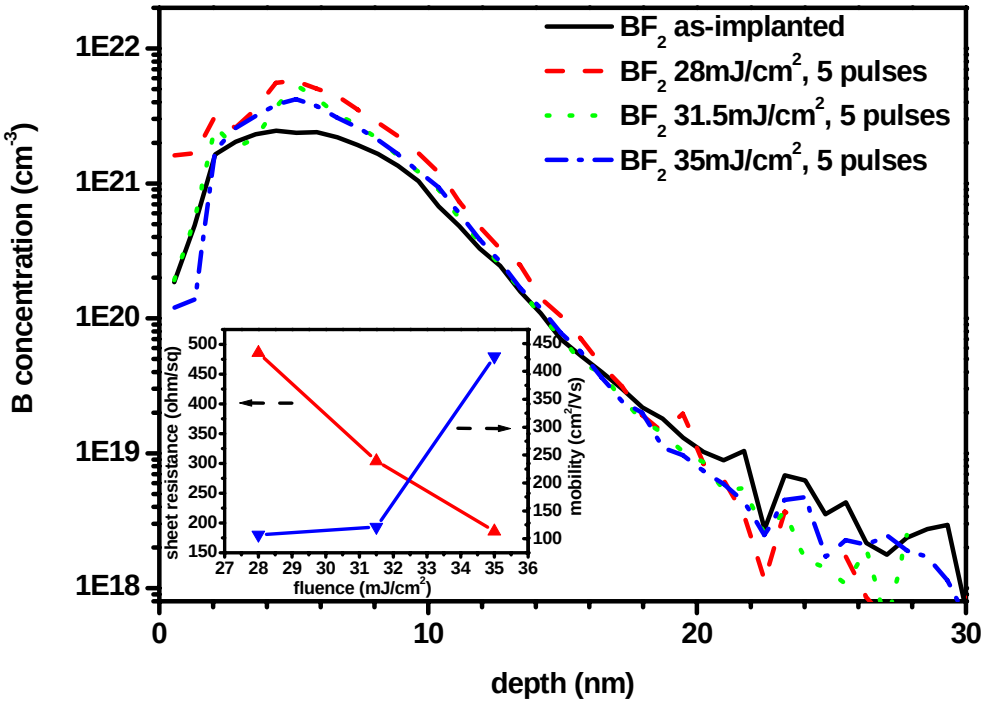

Fig. 3-11. Boron SIMS profiles of the samples annealed with various laser fluences. The inset shows the corresponding sheet resistance and mobility of the samples.

Tables

	B-implanted a-Si (without PAI)	B-implanted Si (with PAI)	BF_2^+-implanted Si	P-implanted Si
Si PAI parameters		**50 KeV $5\times10^{15}/cm^2$**		
Dopant Implantation parameters	**20 keV $5\times10^{15}/cm^2$**	**20 keV $5\times10^{15}/cm^2$**	**25 keV $5\times10^{15}/cm^2$**	**15 keV $5\times10^{15}/cm^2$**
Fluence used for FLA (ELA) (mJ/cm^2)	**37-39**	**30-34**	**27-29 (250)**	**31-33 (250)**
Number of laser shots for FLA (ELA)	**20**	**20**	**20 (20)**	**20 (20)**
Junction depth (as-implanted) (nm)	**~ 270**	**~ 200**	**~ 100**	**~ 100**
Sheet resistance of FLA activated samples (Ω/)	**100-250**	**200-400**	**225-450**	**225-325**
Sheet resistance of RTA activated samples (Ω/)		**280-300 (ref. 6)**		
Sheet resistance of ELA activated samples (Ω/)		**190-300 (ref. 6,7,11)**	**180 (this work)**	**160 (this work)**

Table. 3-1 Implantation parameters, FLA-activation and ELA-activation conditions for three B-doped and P-doped layers. Sheet resistance for doped layers activated by FLA with those activated by ELA methods in this work and reported in Refs. 6, 7 and 11 are listed for comparison. Dopant depth is defined as the distance from the surface, at which the dopant concentrations drop to $10^{18}/cm^3$.

	Fluence used for FLA (mJ/cm^2)	Sheet resistance of FLA activated samples ($\Omega/\square$)	Mobility (cm^2/Vs)	Activated carrier Concentration (activation rate) ($atoms/cm^2$)	Junction depth (nm)
BF_2-implanted Ge	**~ 32-37**	**~ 182-304**	**~ 122-427**	**~1.05×10^{14}-5.25×10^{14} (~22%)**	**~ 17**
P-implanted Ge	**~ 35-49**	**~ 22-24**	**~ 814-1410**	**~2.42×10^{14}-3.01×10^{14} (~7%)**	**~ 40**

Table.3-2 Activation fluence and electrical characteristics of B-doped and P-doped layers activated by FLA.

Chapter 4

Time-Resolved THz Spectroscopy of Femtosecond-Laser-Annealed Amorphous Silicon

4.1 Introduction

With the demand of larger display area and high pixel density of thin film transistor liquid crystal display (TFT-LCD), high mobility TFTs are required for the pixel driver of TFT-LCD in order to shorten the charging time of pixel electrodes. Low temperature poly silicon (LTPS) technology has been studied for the purpose of driver integration at periphery of active matrix liquid crystal display [1]. Because of its better crystalline quality than a-Si, especially the grain size, poly-Si attracted great attention for last two decades [2-5]. TFTs fabricated by poly-Si show higher carrier mobility and better electrical characteristics.

The defects, such as dangling-bond defects in grain boundary or strained defects of poly-Si [6], can reduce the carrier transition speed and lead to the leakage current, which in turn degenerates the performance of TFTs [6-7]. Typical channel length of TFTs are about 5-10 μm, which ideally should be close to or smaller than the grain size of poly-Si in order to leave a single grain in the channel area [8-9]. Laser- or furnace-annealed LTPS fabrications have been employed to obtain larger grain sizes of poly-Si [5]. Since the grain size of poly-Si is one of the key features to affect electrical characteristics of TFTs such as mobility, it is important to examine the grain size of poly-Si before TFT-fabrication. Traditionally, the grain size is examined by SEM. However, a destructive sample preparation, such as Secco etching is required for SEM. Besides, SEM is limited for the observation of tiny area and is not easy to offer the information about the uniformity of poly-Si in large area. Although Hall

measurements can measure the mobility of semiconductors, however, it is also not easy to measure the mobility of intrinsic poly-Si.

Recently, the spectroscopic technique using pulsed THz radiation, called ”terahertz time-domain spectroscopy (THz-TDS)”, has been developed, by taking advantage of short pulses of broadband THz radiation. And THz-TDS is a non-destructive method to measure the carrier concentration and mobility of doped semiconductotrs. Many researches have been performed on a variety of gases, liquids, dielectric materials and semiconductors by THz-TDS. For example, in 1990, D. Grischkowsky et al. studied the THz-TDS with the dielectric materials, such as quartz and sapphire, and semiconductors, like silicon and GaAs. They discovered that different carrier concentrations affect the absorption characteristics of the samples in the THz frequency range. The Drude Model could be used to link the frequency-dependent dielectric response to the material’s free-carrier dynamics properties [10].

In this chapter, the carrier mobility of FLA poly-Si is measured by optical-pump–THz-probe (OPTP) technique [11]. We also measured the temporal evolution of far-infrared conductivity and refractive index of FLA poly-Si. This technique is contact-free, therefore, damage-free. The quality of poly-Si samples annealed at various pump fluence was directly identified by the OPTP technique.

4.2 Generation and Detection of Terahertz Radiation

4.2.1 Surge Current

4.2.1.1 Surface Depletion Field

In semiconductors with a wide bandgap, such as GaAs (E_g = 1.43 eV) or InP (E_g = 1.34 eV), the surface bands of a semiconductor lie within its energy bandgap, and thus Fermi-level pinning occurs, leading to band bending and formation of a depletion region,

where the surface built-in field exists [12]. When a laser beam excites the semiconductor surface, the photo-generated electrons and holes are accelerated in opposite directions under the surface-depletion field, so that a surge current is formed in the direction normal to the surface.

The direction and magnitude of the surface depletion field depend on the dopants, impurity species and the position of the surface states relative to the bulk Fermi level. Generally, the energy band of n-type semiconductors bends upward (Fig. 4-1(a)) and the energy band bends downward for *p*-type semiconductors (Fig. 4-1(b)). The surface built-in field in the p-type semiconductor drives the photogenerated carriers, which is the transient surge current. In the n-type semiconductor, the transient surge current is driven in the opposite direction compared to the p-type semiconductor, as shown in Fig. 4-1(a). In the far-field approximation, the emitted THz-radiation-field amplitude, $E_{THz}(t)$, is proportional to the time derivative of the surge current, $J(t)$:

$$E_{THz}(t) \propto \frac{\partial J(t)}{\partial t}. \quad (1)$$

The unambiguous evidence for distinguishing the main mechanism of THz emission from the semiconductor surface is the polarity of the THz waveform between the n-type and p-type semiconductor. When the surface depletion field is the dominant mechanism for the surge current, the polarity of the THz waveform is opposite between the *n*-type and *p*-type semiconductors.

4.2.1.2 Photo-Dember Effect

The narrow-bandgap InAs and InSb are very interesting materials because of their high electron mobilities: ≈ 30000 cm^2/Vs for InAs and ≈ 76000 cm^2/Vs for InSb, respectively. Recently, InAs attracts much attention as an efficient THz emitter since a significant enhancement of THz emission from InAs has been observed under magnetic fields [13]. The

effect of surface depletion field is not so large for the narrow-bandgap semiconductors because of their small bandgap energies.

The absorption depth of a narrow bandgap semiconductor surface photoexcited by near infrared light ($h\nu$=1.5 eV) is very thin ($\approx$100 nm) [14], and the excess energy of the photoexcited carrier is very large. THz generation from the narrow-bandgap semiconductors is mainly due to the Photo-Dember effect, which is known to generate current or voltage in semiconductors attributed to the difference of the electron and hole diffusion velocities.

The diffusion current due to the Photo-Dember effect after photoexcitation near a semiconductor surface is illustrated in Fig. 4-2. Because the electron mobility is always larger than the hole mobility, the direction of diffusion current induced by the Photo-Dember effect is in the same way for each kind of semiconductor and irrespective of the doping type (n or p). Therefore, the THz waveform emitted from the surface surge current due to the Photo-Dember effect will show the same polarity for *n*-type and *p*-type semiconductors.

The diffusive currents of the electrons (J_n) and holes (J_p) are, respectively, described by the following equations [15],

$$J_n \propto -eD_e \frac{\partial \Delta n}{\partial x}, \tag{2}$$

$$J_p \propto eD_h \frac{\partial \Delta p}{\partial x}, \tag{3}$$

where e is the electron unit charge, Δn and Δp are the density of photocreated electrons and holes, D_e and D_h are the diffusion coefficient of electrons and holes, respectively. The diffusion coefficient D is defined by the Einstein relation, $D = k_b T\mu / e$, where k_b is the Boltzman constant, T is the temperature of the corresponding carrier, and μ is the mobility of electrons or holes. The THz radiation from the Dember current $J_{dif} = J_n + J_p$ is proportional to the difference in the mobility for the electrons and holes, and the gradient of the carrier density.

Narrow bandgap semiconductors should have the ability to create a large Photo-Dember field due to the large electron mobility and large excess carrier energies. Moreover, the Photo-Dember field in the narrow bandgap semiconductors is further enhanced by the small absorption depth.

4.2.2 Free Space Electro-Optics Sampling

The coherent detection of a THz-pulse beam with EO crystal is based on the linear EO effect (Pockels effect) [16]. The incident THz-pulse beam modifies the refractive index ellipsoid (or birefringence) of the EO crystal giving rise to a phase retardation of the linearly polarized optical probe beam. By monitoring the phase retardation, the field strength of the THz pulse is detected. A pellicle beam splitter combines the THz beam and the probe beam so that both may copropagate. The polarization of both the THz and optical probe beams are aligned parallel to the [1, −1, 0] direction of a (110) oriented ZnTe sensor crystal. Following the sensor crystal, a quarter-wave plate is used to afford a $\pi/4$ optical bias to the probe beam, which allows the system to be operated in the linear range. A Wollaston polarizer is used to convert the THz-radiation-field induced phase retardation of the probe beam into an intensity modulation between the two mutually orthogonal linearly polarized beams. A pair of Si p-i-n photodiodes connected in a balanced circuit is used to detect the optical intensity modulation.

The difference signal of p-i-n photodiodes is fed to a lock-in amplifier referenced at a frequency at which the pumping optical beam is chopped to generate the THz radiation. Because of the instantaneous response of the Pockels effect, the EO crystal acts well as a sampling detector. Hence, this method is called EO sampling. The detection with an EO crystal is becoming popular due to its broad-bandwidth capability and ease of implementation. In the EO detection there is a clear trade-off between the sensitivity and frequency response that is determined by the choice of crystal and its thickness. A thicker

crystal produces a greater interaction length, but on the other hand it reduces the detection bandwidth due to group-velocity mismatch between THz beam and probe beam. In addition, the EO technique is very sensitive to the laser noise and to low-frequency mechanical and acoustical disturbances.

The pumping optical beam to generate THz radiation is partly divided to use for a probe beam. The output signal from the lock-in amplifier versus time-delay scanning of the probe beam reveals the THz-pulse waveform.

4.3 Experiments

The sample preparation and the setup of laser annealing system is the same as the system we mentioned in chapter 2. The samples in this experiment are a-Si layers irradiated with 95% interpulse overlapping of laser pulses at two different laser fluences, 35 and 45 mJ/cm^2. In order to verify the grain size of poly-Si in this study, the SEM pictures of annealed areas are obtained by delineating defects using Secco etching. The system setup of THz-TDS and OPTP system will be mentioned as below.

4.3.1 Terahertz Time Domain Spectroscopy

The experimental setup of THz-TDS system is shown in Fig. 4-3. An amplified Ti:Sapphire laser source generating 50 fs, 800 nm, 2 mJ pulses at a repetition rate of 1 kHz is divided into pump and probe beams by a beam splitter. The first s-polarized 800 nm beam transmits a half-wave plate, turns to p-polarization, and then impinges on [100] p-type InAs surface in order to generate terahertz pulse predominantly by the Photo-Dember effect. The second 800 nm beam is used to detect the electric field of the terahertz pulses using free-space electro-optic sampling in 2 mm-thick (110) ZnTe crystal.

The 800 nm beam reflects from the InAs surface is blocked by a black polyethylene sheet which has high transmission in the far-infrared. Gold-coated parabolic mirrors are used to collimate and focus the terahertz beam onto the sample. The probe beam, of which the time delay can be tuned by a motorized stage, is guided to the ZnTe crystal collinearly with the terahertz pulse. The transmitted probe laser pulse with polarization changed by the electro-optical effect is separated into two beams with orthogonal polarizations by the Wollaston beam splitter. These two beams are coupled to a balanced detector connecting to a lock-in amplifier. Signal from the lock-in amplifier can be easily analyzed by a computer. The chopper is set up in a frequency of about 160 Hz in order to get the best signal to noise ratio of THz.

In order to reduce the absorption of THz signal by water vapor, the THz-TDS system is covered with an acrylic box which is continuously purged with pure nitrogen. The humidity can rapidly decrease to about 5% in tens of minutes. Owing to the more stable atmosphere and temperature in the acrylic box, the THz system becomes more stable.

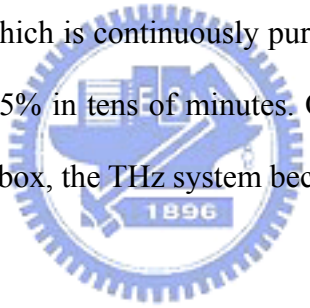

4.3.2 Optical-Pump-Terahertz-Probe System

The extension of THz-TDS to OPTP is quite simple as shown in Fig. 4-4. Let the laser beam pass through a beam splitter; the reflected beam will incident into the THz-TDS system and the transmitted beam will be taken as the optical pump beam. The optical pump beam is frequency doubled to 400 nm by a BBO crystal and is used to excite the sample. The optical pump beam induces a variation of carrier concentration in the sample and the resulted changing of terahertz transmission will be measured.

Both the THz pump beam and the optical pump beam pass through a small pinhole placed between two parabolic mirrors. The sample is fixed on another small pinhole and the incident angle of optical pump beam on the sample is fixed to be about 5°. The spot size of the 400 nm pump beam on the sample is about 3 mm. The mounting of our sample, as

shown in Fig. 4-5, has a 2-mm-diameter aperture for uniform illumination of the sample with the pump beam and ensures the good overlapping of the pump beam and the THz probe beam. Time domain electric field of THz in our system is shown in Fig. 4-6(a) and the corresponding amplitude spectrum is shown in Fig. 4-6(b).

The main advantage of OPTP is the direct measurement of the far-infrared conductivity and refractive index variation in comparison to the optical pump-probe method. Besides, we are also able to obtain the variation of complex conductivity by OPTP. Because the pulse duration of THz is approximately 1 ps, OPTP has lower sensitivity and lower temporal resolution in comparison to the optical pump-probe method.

There are two methods to acquire data from the OPTP experiment. The first method is to measure the carrier dynamics by setting the time delay of the optical pump pulse at a certain value corresponding to the temporal position where the main peak of THz pulse locates at the sample. Then the dynamics are measured by scanning of the optical pump delay line to map out the dynamics. This one-dimensional method measures the dynamics averaged over the frequency contents of the THz pulse. The transmission, T, of the amplitude of main peak of THz pulse was measured by lock-in amplifier as the time delay between THz pulse and the 400 nm pump pulse. The differential transmission, $\Delta T/T_0 = (T - T_0)/T_0$ where T_0 is the transmission of the peak amplitude of the THz pulse at negative time delays before the sample has been excited by optical pump pulse.

The second data acquisition method for the OPTP experiments is a two-dimensional technique. We set the delay of the optical pump line at a fixed time delay, and then scan the THz waveform by THz-TDS. By measuring this waveform at different optical pump delay, it will be able to observe the evolution of the induced changes in the amplitude and phase of the THz electric field.

4.4 Extraction of Optical Constant by Terahertz Time Domain Spectroscopy

We study the complex conductivity and optical constant from 0.4 to 2 THz by using THz-TDS system at certain optical pump time delay. The Drude model is used to fit the complex conductivity and optical constant.

We show the schematic of sample in Fig.4-7, where $E_0(\omega)$ is the incident electric field of THz, $E_{ref}(\omega)$ is the transmitted THz field of the substrate, $E_{film}(\omega)$ is the transmitted electric field of the film, d is the optical-pumped depth of the film (the penetration depth of 82nm for crystalline silicon at 400nm). n_1, n_2 and n_3 are the refractive indices. In our sample, n_1=1, n_3=3.41 is the refractive index of the silicon. The complex refractive index of the film is $n_2 + i\kappa_2$, where n_2 is the real refractive index and κ_2 is the extinction coefficient.

$E_{ref}(\omega)$ can be expressed as:

$$E_{ref}(\omega) = t_{13} \exp(\frac{i\omega d}{c}) E_0(\omega), \tag{4}$$

Considering the multiple reflections in the film, the $E_{film}(\omega)$ can be expressed as:

$$E_{film}(\omega) = \frac{t_{12}t_{23} \exp(\frac{in_2\omega d}{c})}{1 - r_{21}r_{23} \exp(\frac{i2n_2\omega d}{c})} E_0(\omega), \tag{5}$$

where c is the speed of the light in vacuum, the r_{ij} and t_{ij} are the reflection and transmission coefficient from i to j interface. We suppose that $\left|\frac{n\omega d}{c}\right|$<<1, because of our thin film sample. We can simplify equation (5) as:

$$\frac{E_{film}(\omega)}{E_{ref}(\omega)} = 1 + \frac{i\omega d}{c(n_1 + n_3)}[(n_2 + i\kappa_2)^2 + n_1 n_3 - n_1 - n_3], \tag{6}$$

Equation (6) is expressed as $\frac{E_{film}(\omega)}{E_{ref}(\omega)} = \mathrm{A}\exp(-i\Delta)$, where A and Δ are obtained from the Fourier transformed reference and signal THz pulses [16]. By using $\varepsilon^{'} + i\varepsilon^{"} = (n_2 + i\kappa_2)^2$, the real and imaginary part of equation (4), (5) can be represented as:

$$\varepsilon^{'} = \frac{c}{\omega d}(n_1 + n_3)A\sin\Delta - n_1 n_3 + n_1 + n_3, \tag{7}$$

$$\varepsilon^{"} = (n_1 + n_3)\frac{(1 - A\cos\Delta)c}{\omega d}, \tag{8}$$

Owing to the equation $\varepsilon^{'} + i\varepsilon^{"} = (n_2 + i\kappa_2)^2$, the conductivity, real refractive index and the extinction coefficient can be deduced by:

$$n_2 = \frac{1}{\sqrt{2}}[\varepsilon^{'} + \sqrt{\varepsilon^{'2} + \varepsilon^{"2}}]^{1/2}, \tag{9}$$

$$\kappa_2 = \frac{1}{\sqrt{2}}[-\varepsilon^{'} + \sqrt{\varepsilon^{'2} + \varepsilon^{"2}}]^{1/2} \tag{10}$$

$$\sigma = \omega\varepsilon_0[\varepsilon^{"} + i(\varepsilon^{'} - \varepsilon_\infty)], \tag{11}$$

where ε_∞ is the contribution of the bound electrons. The complex conductivity is deduced from Maxwell equation, assuming there exists a flowing current, $\vec{J} = \sigma\vec{E}$. The formula can be represented by:

$$\begin{aligned} \nabla \times \vec{H} &= \vec{J} + \frac{\partial \vec{D}}{\partial t} = \vec{J} + i\omega\varepsilon_0\varepsilon_\infty\vec{E} \\ &= i\omega\varepsilon_0\left[\varepsilon_\infty + \frac{\sigma}{i\omega\varepsilon_0}\right]\vec{E} = i\omega\varepsilon_0\varepsilon\vec{E} \\ \varepsilon &= \varepsilon_\infty + \frac{\sigma}{i\omega\varepsilon_0} \end{aligned} \tag{12}$$

While the measured complex conductivity and complex refractivity index are obtained by considering of multiple reflections, it is useful to use Drude model to describe transient conductivity.

4.5 Determination of Mobility and Conductivity from Drude Model

The Drude model was developed in the 1900s by Paul Drude. The Drude model explains the transport properties of electrons in materials. It treats conduction electrons as free to move under the influence of an applied field. The Drude model can also predict conductivity as a response to time-dependent electric field with an angular frequency ω, which can be expressed as

$$\sigma(\omega) = \frac{\varepsilon_0 \omega_p^2 \tau_0}{1 - i\omega\tau_0}, \quad . \tag{13}$$

The plasma frequency (ω_p) is defined as $\omega_p = Ne^2/\varepsilon_0 m^*$, where N is the carrier concentration, e is the electronic charge, m* is the effective carrier mass and τ_0 is the carrier scattering time. We can use the complex conductivity by the Drude model to fit the measured complex conductivity. The two fitting parameters are carrier concentration, N, and carrier scattering time ($\tau_0 = \mu m^*/e$, where μ is mobility). The fitting method is to find the least mean square between $\sigma_{multiple}$ and σ_{Drude} in the frequency 0.4 – 2 THz, which can be represented as:

$$\sum(\sigma_{multiple} - \sigma_{Drude})^2 = error, \tag{14}$$

The best fitting of Drude model will be obtained when error is in minimum.

4.6 Results and Discussions

In the OPTP system, the frequency doubled (400 nm) pump pulses with a spot size of 3 mm were used to excite free carriers in poly-Si and THz probe is generated from photoexcited InAs surface as shown in Fig. 4-4 [11]. Relatively weak 800 nm probe beam is used for free-space electro-optic detection of THz. The focused spot size of THz beam on

the sample is approximately 2 mm. In order to investigate the carrier dynamics, the peak amplitude of THz waveform of terahertz time domain spectroscopy (**THz-TDS**) is measured as a function of delay time between the THz probe and optical pump pulse. The temporal evolution of the refractive index and the extinction coefficient of the sample are investigated by measuring the THz waveform at a certain delay time in THz-TDS [17].

To verify the grain size of FLA-annealed samples, SEM pictures of annealed areas are obtained by delineating defects using Secco etching. Figure 4-8 shows the laser fluence dependence of the grain size. The average grain sizes of poly-Si annealed at the fluence of 45 and 34 mJ/cm^2 are 500 (large-grain size poly-Si) and 50 nm (small-grain size poly-Si), respectively. The grain size and corresponding TFT performance have been discussed in our previous study.

4.6.1 Optical-Pump-Terahertz-Probe Measurements

Figure 4-9 shows the normalized differential transmission of large- and small-grain size poly-Si at the optical pump fluence of 636 μJ/cm^2. The corresponding ejected carrier density at this fluence is about 3.4×10^{19} cm^{-3}. Differential transmission is defined as $-\Delta T/T_0 = -(T - T_0)/T_0$, where T_0 is the transmitted THz pulses through the unexcited sample. Both curves show subpicosecond onset of transmission drop followed by a long-term recovery. The decay trend can be fitted by double exponential function:

$$\Delta T/T_0 = \Delta T_{\max} * [a * \exp(-t/\tau_a) + (1-a) * \exp(-t/\tau_b)], \quad (15)$$

where both τ_a and τ_b are band-to-band carrier recombination time and carrier trapping time, respectively [18]. The fitting parameters are summarized in Table 4-1.

As soon as intense 400 nm pumping pulses arrive, free carriers are generated in the poly-Si and they affect the THz probe pulses arriving later with a time delay. The recovery of THz transients, therefore, is determined by recombination and trapping of the thermalized

carriers. Similar THz transient behavior has been observed for microcrystalline silicon (μc-Si) pumped by regeneratively amplified Ti:sapphire oscillator [18]. For μc-Si, the grain size (10-15 nm) is much smaller than that of FLA annealed poly-Si. Larger grain sizes of FLA annealed poly-Si implies that there are fewer grain boundaries and dangling bonds.

Relatively higher defect density of μc-Si induces the fast recovery of THz transmission transients and reflected in a shorter trapping time of 0.7 ps. The observed longer relaxation time (~32.7 ps) of the large-grain size poly-Si, therefore, suggests that it has fewer defects to trap the carriers after FLA annealing (Fig. 4-9) [19]. The relaxation time of small-grain size poly-Si is slightly shorter (=~24.4 ps) than the large-grain poly-Si. An inset in Fig. 4-9 shows the THz transient of FLA annealed poly-Si at different laser fluences (318-955 $\mu J/cm^2$) and only slight change of the relaxation time (< ±1.2 ps) is observed. Higher pump fluence is supposed to excite more carriers, but the observed insensitive relaxation time to the pump fluence implies that no nonlinear Auger-recombination process is involved in the carrier relaxation for our samples injected with different carrier densities [20-21, 22]. Thus the relaxation observed in Fig. 4-9 is mainly due to the trapping of carriers by defect states in poly-Si.

In Fig. 4-9, the large-grain poly-Si shows stronger absorption of THz radiation than the small-grain poly-Si does. This implies that under the same pump fluence, the large-grain poly-Si has more photoexcited free carriers, which are actively absorbing the THz.

4.6.2 Terahertz Time Domain Spectroscopy Measurements

Since the mobility is correlated with the grain size and so does the defects, we must ensure that the carrier dynamics in our measurement is dominated by trapping of carriers in the defects. The carrier recombination process starts to be dominant in the timescale of about ten picoseconds. Therefore, in order to observe only trapping induced phenomena, we measured the THz transient at a fixed time delay, 10 ps after the pump [23].

In the THz-TDS analysis, the measured time-domain THz waveforms from FLA-poly-Si and Si substrates are Fourier transformed, and then the frequency-dependent dielectric constant of the poly-Si sample is calculated from the spectral amplitude and phase difference between the optical-pumped and un-pumped samples. The experimental results and fitting results of n and κ of these two samples are shown in Fig. 4-10.

With the given film thickness defined by the penetration depth (82nm) of crystalline silicon at 400 nm [24], the complex conductivity of the FLA annealed poly-Si (sample A and B) in THz range are shown in Fig. 4-11. The uncorrelated fluctuation of the response may be due to the laser intensity fluctuation and thin film uniformity. The Hall measurement is also employed to measure the mobility of bulk silicon for comparison. The fitted parameters and the result of Hall measurement are summarized in Table 4-2.

With the same optical pumping fluence, the conductivity and refractive index of sample A measured at different optical pump delay, from 0 ps to 150 ps, are shown in Fig. 4-12 to 4-14. This time delay is limited by the travel range of delay stage. The fitting parameters of these figures are summarized in Table 4-3 and the results are plotted in Fig. 4-15. The carrier concentration at zero time delay is in good agreement with the carrier concentration ejected by the optical pump beam. As the optical pump delay increased, the carrier concentration decreased slightly. Contrary to the carrier concentration, the mobility increased with the optical pump delay. This increasing of mobility should reach a maximum at longer time delay (steady state). The slight decreasing of the carrier concentration probably indicates that the available trapping sites are filled up (< 10 ps) and leave only carrier recombination for longer time delay. Therefore, the low mobility at zero optical pump delay induced by carrier-carrier scattering will be improved as the carrier concentration becomes lower.

Because of the high resistivity and low carrier concentration of bulk-Si, broad range of mobility was measured from the Hall measurement, but it is still consistent with the mobility measured by THz-TDS. The mobility of thin poly-Si with low carrier concentration

cannot be measured by the Hall measurement. This thin layer of poly-Si also causes the large fluctuation of mobility and plasma frequency in Table 4-2. The mobility of a-Si, radiation-damaged silicon-on-sapphire (RD-SOS), silicon-on-sapphire (SOS), and nanocrystalline poly-Si measured by other studies are also listed in the table for comparison [20-21]. It is noteworthy that the mobilities in Ref. 20-21 are obtained by the fitting of normalized differential transmission of THz, which is different from our method.

The main trapping defects in poly-Si can be distinguished into the tail states and deep states, which are known as the dangling bonds at the grain boundary and interface of thin films. Grain trap-state densities for TFTs can be examined using the field-effect conductance method by which the defects in different energy bandgap can be distinguished [7, 25]. It is well known that both leakage current and mobility of TFTs are more closely associated with the trap states located near the band edges [26-27]. This is because of the band-bending at the surface of poly-Si when a positive gate voltage was applied. Thus the tail states affect the gate bias dependence of the transconductance and drift mobility in the turn-on state of TFTs.

In this research, however, we measured the conduction mobility instead of the drift mobility so that the observed transient THz response may not be affected by the tail states. Since the penetration depth of poly-Si at 400 nm is shallower than film thickness of poly-Si, the trapping states at Si/SiO_2 interface can be neglected. Lui et al. observed the similar fast recovery of THz transmission of a-Si and nanocrystalline silicon deposited by LPCVD and the deep state defects are found to be responsible [20]. For a-Si, high deep state density (10^{18}-10^{19} cm^{-3}) which is determined by the electron-spin resonance induces the reduction of relaxation time constant [28]. Meanwhile, the tail states may dominate the trapping process in the sample with a low deep state density ($<10^{16}$ cm^{-3}).

In our previous study, we found that the poly-Si with large grain size corresponds to a slightly lower deep state density [7]. Since the deep state density of FLA crystallized poly-Si

are close to that of poly-Si crystallized by SPC and excimer laser annealing (10^{18}-10^{19} cm^{-3}), the fast recovery of THz transmission in our work may be also related to deep state trapping [7, 28-29]. The corresponding injected carrier densities of various laser fluences in our study are 1.7-5.1×10^{19} cm^{-3}, much smaller than the tail state density of FLA crystallized poly-Si (10^{22}-10^{23} cm^{-3}), and therefore these states cannot be saturated by the trapping of the photoexcited carriers [7, 22]. Consequently, the increase of mobility for large-grain size poly-Si can be mainly attributed to the reduction of deep state density.

Despite that the mobility measured by OPTP can offer the information of correlated average grain size in large area, there are some limits for the OPTP technique. Because of the diffraction limit of THz pulses, the spatial resolution of THz beam is of the order of hundreds of μm which is at least thousands times larger than the grain size of poly-Si. Thus OPTP may not be suitable for analyzing the uniformity of grain size. However, the OPTP technique still shows a high potential for commercial application of mobility measurement for poly-Si.

This is firstly due to that the average grain size of ELA-crystallized poly-Si grown by super lateral growth mechanism in commercial production is about 400 nm which is close to our sample. Thus THz-TDS analysis in this study is able to distinguish the grain quality of poly-Si. Secondly, compact light source such as fiber laser applied on THz generation has reached maturity and may be applied on simultaneous optical pumping and THz generation by antenna in the near future. Thus OPTP integrated with a fiber laser can provide a compact and inexpensive diagnosis system for the determination of grain size and mobility of poly-Si.

4.7 Summary

We use a non-contact technique to measure photoexcited carrier relaxation time and mobility of poly-Si. This technique has a high application prospect in examining the

annealing quality of low temperature poly-Si. The complex conductivity and refractive index of poly-Si are measured by THZ-TDS in the frequency range from 0.4 to 2 THz. Poly-Si with different grain sizes was distinguished by OPTP and their transient mobilities are obtained by THz-TDS. From the best fit to the Drude model, the mobilities of the large- and small-grain size poly-Si are measured to be 175±19.4 cm^2/V s and 94.5±20.2 cm^2/V s, respectively. Larger mobility of large-grain size poly-Si is closely associated with the reduction of deep state density due to improvement of crystalline quality after FLA. The THz-TDS shows a potential for future application on TFT production for grain size and mobility diagnostics without making any damage to the sample.

References

[1] K. Sera, F. okumura, H. Uchida, S. Itoh, S. Kaneko and K. Hotta, "High-performance TFT's fabricated by XeCl excimer laser annealing of hydrogenated amorphous-silicon film," IEEE Trans. Electron Devices, vol. 36, pp. 2868-2872, 1989.

[2] E. Ibok and S. Garg, "A characterization of the effect of deposition temperature on polysilicon properties," J. Electrochem. Soc., vol. 140**,** pp. 2927-2937, 1993.

[3] R. Kakkad, J. Smith, W. S. Lau, S. J. Fonash, and R. Kerns, "Crystallized Si films by low-temperature rapid thermal annealing of amorphous silicon," J. Appl. Phys., vol. 65, pp. 2069-2072, 1989.

[4] N. Kubo, N. Kusumoto, T. Inushima, and S. Yamazaki, "Characterization of polycrystalline-Si thin-film transistors fabricated by excimer laser annealing method," IEEE Trans. Electron Devices, vol. 40, pp. 1876-1879, 1994.

[5] A. T. Voutsas, "A new era of crystallization: advances in polysilicon crystallization and crystal engineering," Appl. Surf. Sci., vol. 208, pp. 250-262, 2003.

[6] M. Miyasaka and J. Stoemenos, "Excimer laser annealing of amorphous and solid-phase-crystallized silicon films," J. Appl. Phys., vol. 86, pp. 5556-5565, 1999.

[7] Y. C. Wang, J. M. Shieh, H. W. Zan and C. L. Pan, "Near-infrared femtosecond laser crystallized poly-Si thin film transistors," Opt. Express, vol. 15, pp. 6981-6986, 2007.

[8] A. Hara, F. Takeuchi, and N. Sasaki, "Selective single-crystalline-silicon at the pre-defined active regions of TFTs on a glass by a scanning CW laser irradiation," IEEE Electron Devices Society, Proc. of 2000 International Electron Device Meeting, pp. 209-212, 2000.

[9] J. S. Im, R. S. Sposili, and M. A. Crowder, "Single-crystal Si films for thin-film transistor devices," Appl. Phys. Lett., vol. 70, pp. 3434-3436, 1997.

[10] D. M. Mittleman, R. H. Jacobsen, R. Neelamani, R. G. Baraniuk and M. C. Nuss,

"Gas sensing using terahertz time-domain spectroscopy," Appl. Phys. B,, vol. 67, pp. 379-390, 1998.

[11] M. C. Beard, G. M. Turner, C. A. Schmuttenmaer, "Terahertz spectroscopy," J. Phys. Chem. B., vol. 106, pp. 7146-7159, 2002.

[12] X.-C. Zhang and D. H. Auston, "Optoelectronic measurement of semiconductor surfaces and interfaces with femtosecond optics," J. Appl. Phys., vol. 71, pp. 326-338, 1992.

[13] N. Sarukura, H.Ohtake, S. Izamida, and Z. Liu, "High average-power THz radiation from femtosecond laser-irradiated InAs in a magnetic field and its elliptical polarization characteristics," J. Appl. Phys., vol. 84, pp. 654-656, 1998.

[14] T. Dekorsy, H. Auer, H. Bakker, H. Roskos, and H. Kurz, "THz electromagnetic emission by coherent infrared-active phonons," Phys. Rev. B., vol. 53, pp. 4005-4014, 1996.

[15] S. Kono, P. Gu, M. Tani and K. Sakai, "Temperature dependence of terahertz radiation from n-type InSb and n-type InAs surfaces," Appl. Phys. B, vol. 71, pp. 901-904, 2000.

[16] Z. Lu, P. Campbell and X.-C. Zhang, "Free-space electro-optic sampling with a high-repetition-rate regenerative amplified laser," Appl. Phys. Lett., vol. 71, pp. 593-595, 1997.

[16] T. -R. Tsai, S. -J. Chen, and C. -F. Chang, "Terahertz response of GaN thin films," Opt. Express, vol. 14, pp. 4898-4907, 2006.

[17] P. U. Jepsen, W. Schairer, I. H. Libon, U. Lemmer, N. E. Hecker, M. Birkholz, K. Lips and M. Schall, "Ultrafast carrier trapping in microcrystalline silicon observed in optical pump-terahertz probe measurements," Appl. Phys. Lett., vol. 79, pp. 1291-1293, 2001.

[18] M. C. Beard, G. M. Turner and C. A. Schmuttenmaer, "Subpicosecond carrier

dynamics in low-temperature grown GaAs as measured by time-resolved terahertz spectroscopy," J. Appl. Phys., vol. 90, pp. 5915-5923, 2001.

[19] K. P. H. Lui, and F. A. Hegmann, "Fluence-and temperature-dependent studies of carrier dynamics in radiation-damaged silicon-on-sapphire and amorphous silicon," J. Appl. Phys., vol. 93, pp. 9012-9018, 2003.

[20] D. G. Cooke, A. N. MacDonald, A. Hrysiw, J. Wang, Q. Li, A. Meldrum and F. A. Hegmann, "Transient terahertz conductivity in photoexited silicon nanocrystal films," Phys. Rev. B, vol. 73, pp. 193311-193314, 2006.

[21] A. Esser, K. Seibert, H. Kurz, G. N. Parsons, C. Wang, B. N. Davidson, G. Lucovsky, and R. J. Nemanich, , "Ultrafast recombination and trapping in amorphous silicon," Phys. Rev. B., vol. 41, pp. 2879-2884, 1990.

[22] S. K. Sundaram, and E. Mazur, "Inducing and probing non-thermal transitions in semiconductors using femtosecond laser pulses," Nature Materials, vol. 1, pp. 217-224, 2002.

[23] F. Gao, L. Carr, C. D. Porter, D. B. Tanner, G. P. Williams, C. J. Hirschmugl, B. Dutta, X. D. Wu, and S. Etemad, "Quasiparticle damping and the coherence peak in $YBa_2Cu_3O_{7-\delta}$," Phys. Rev. B., vol. 54, pp. 700-710, 1996.

[24] G. Fortunato and P. Migliorato, "Determination of gap state density in polycrystalline silicon by field-effect conductance," Appl. Phys. Lett., vol. 49, pp. 1025-1027, 1986.

[25] T. J. King, M. G. Hack and I. W. Wu, "Effective density-of-states distributions for accurate modeling of polycrystalline-silicon thisn film transistors," J. Appl. Phys., vol. 75, pp. 908-913, 1994.

[26] M. Miyasaka and J. Stoemenos, "Excimer laser annealing of amorphous and solid-phase-crystallized silicon films," J. Appl. Phys., vol. 86, pp. 5556-5565, 1999.

[27] A. M. Johnson, D. H. Auston, P. R. Smith, J. C. Bean, J. P. Harbison and A. C. Adams, "Picosecond transient photocurrents in amorphous silicon," Phys. Rev. B., vol. 23, pp.

6816-6819, 1981.

[28] N. H. Nickel, G. B. Anderson and R. I. Johnson, “Grain-boundary defects in laser-crystallized polycrystalline silicon,” Phys. Rev. B., vol. 56, pp. 12065-12068, 1997.

Figures

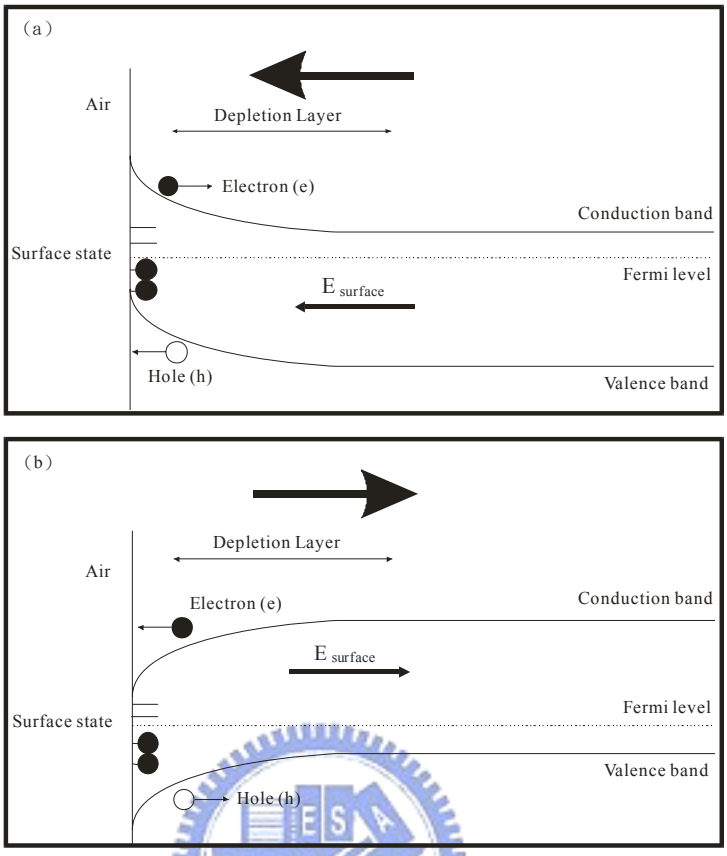

Fig. 4-1 Band picture and the schematic flow of drift current (a) for n-type and (b) for p-type.

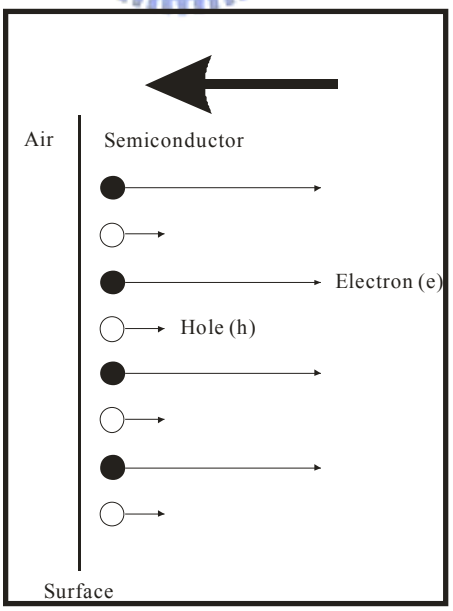

Fig. 4-2 The schematic flow of diffusion current near the surface of semiconductor which is induced by photoexcited carriers.

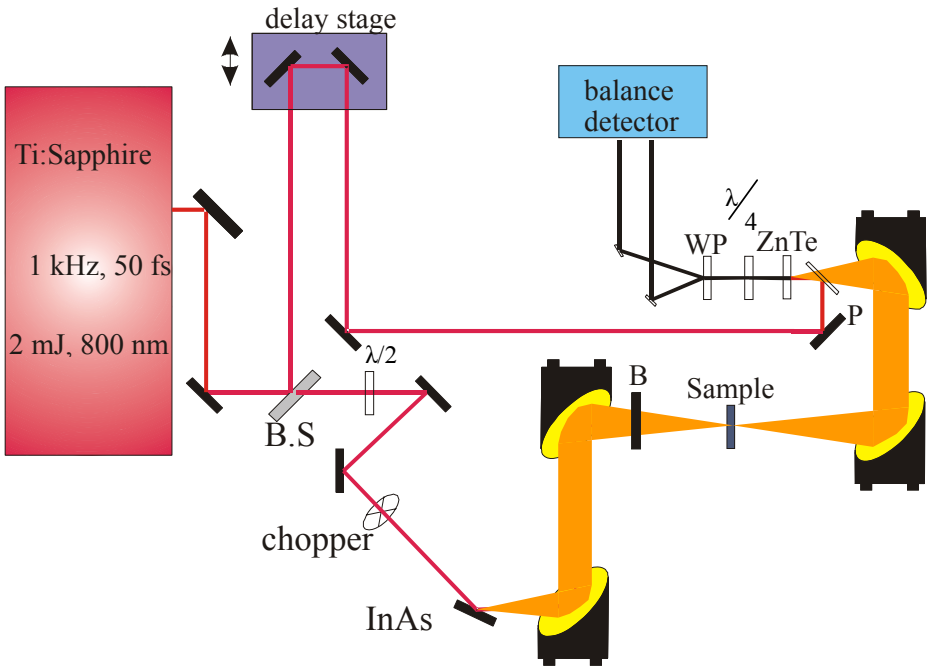

Fig. 4-3 The scheme map of the THz-TDS system. BS: beam splitter; B: polyethylene visible beam block; F: blue filter; WP: Wollaston prism; P: pellicle.

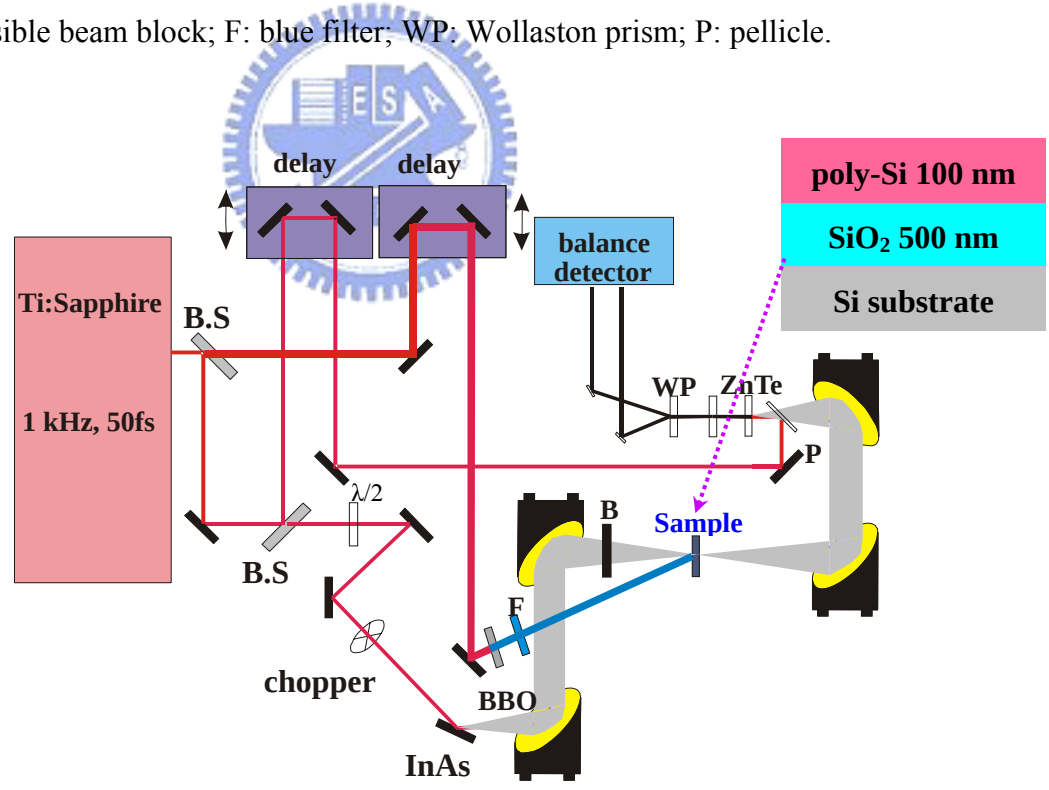

Fig. 4-4 Sample structure of a-Si and scheme of the OPTP system. BS: beam splitter; B: polyethylene visible beam block; F: blue filter; S: sample; WP: Wollaston prism; P: pellicle.

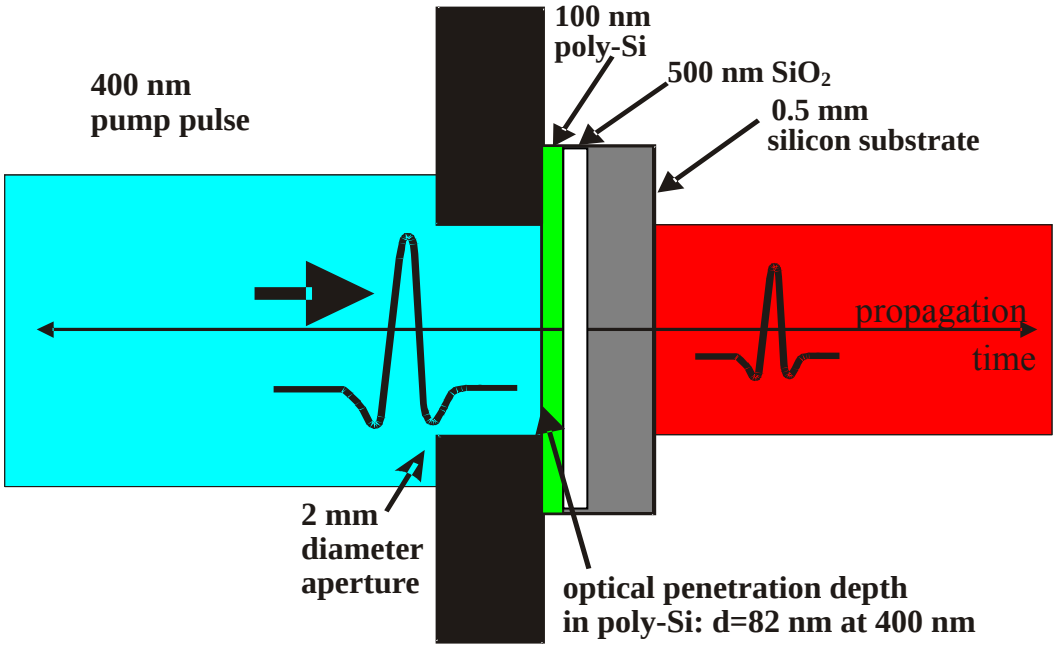

Fig. 4-5 The scheme of poly-Si and sample mount with 2mm-diameter aperture for OPTP and THz-TDS measurements.

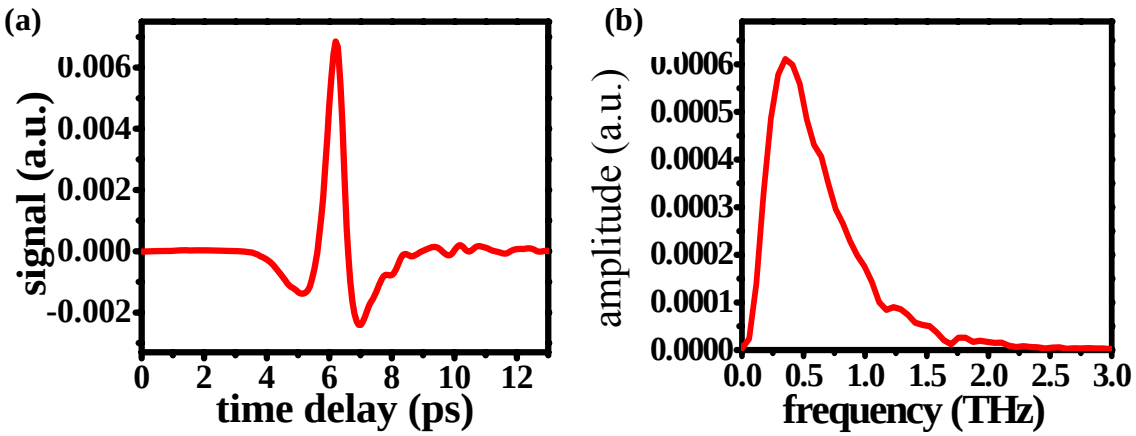

Fig. 4-6 (a) Time domain electric field of THz. (b) Amplitude spectrum for the THz pulse in (a).

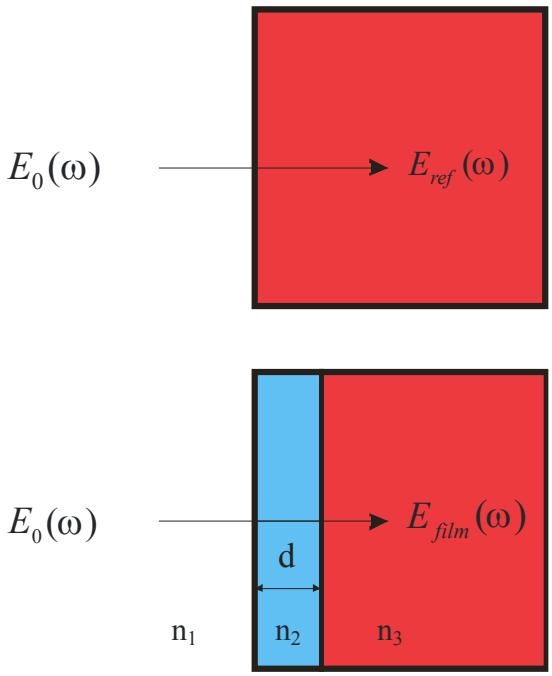

Fig. 4-7 The schematic sample between pump and unpump. n_1, n_2, n_3 is the refractive indices. $E_0(\omega)$ is the incident THz field. $E_{ref}(\omega)$ and $E_{film}(\omega)$ are the reference (without optical-pumping beam) and sample (with optical-pumping beam).

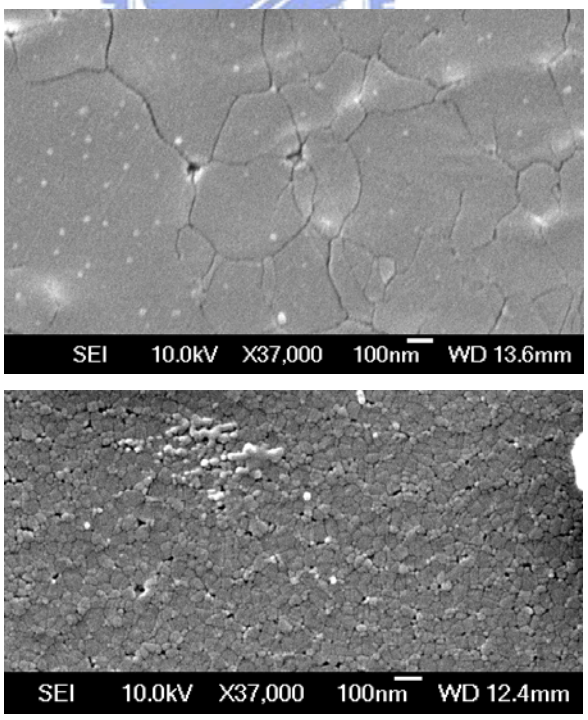

Fig. 4-8 SEM pictures of pc-Si samples annealed by FLA with (a) 45, (b) 34 mJ/cm^2.

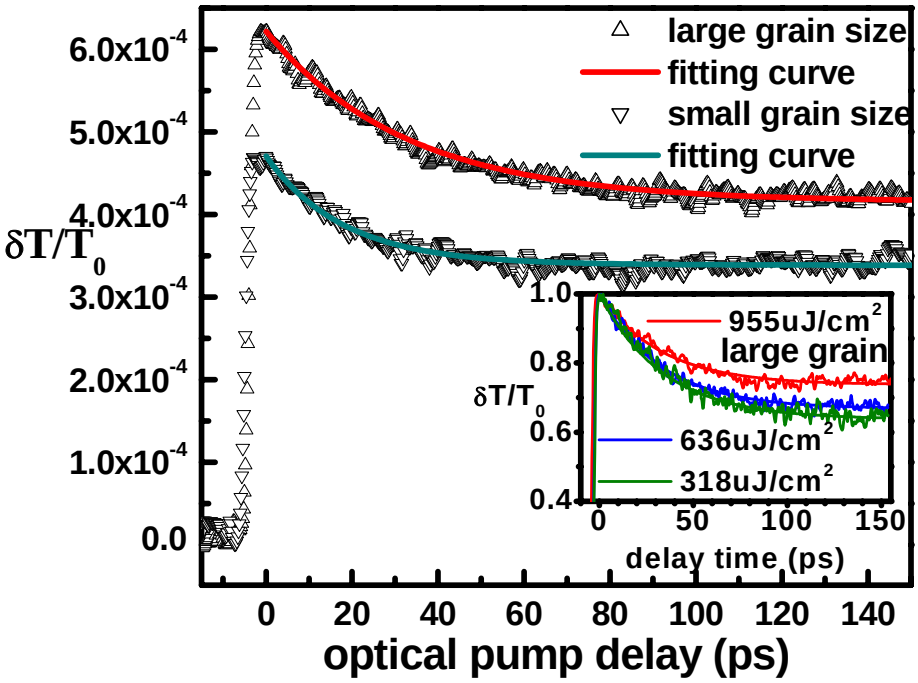

Fig. 4-9 Differential transmission at the peak of the THz pulse for different grain sizes of poly-Si.

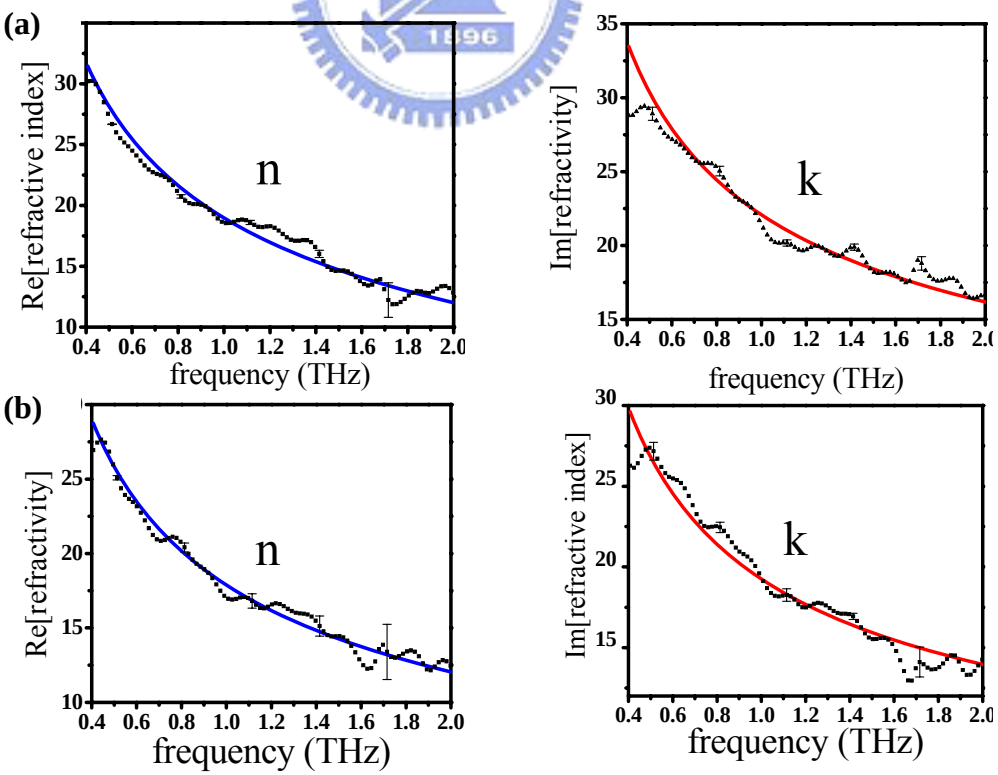

Fig. 4-10 The experimental results and fitting results of n and κ of (a) sample A and (b)sample B.

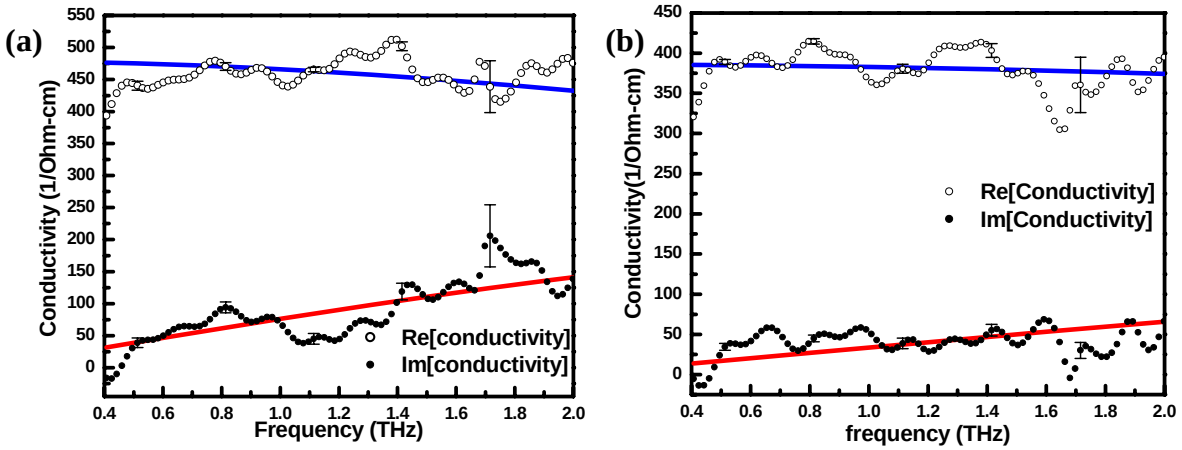

Fig. 4-11 THz conductivity spectra of (a) poly-Si with larger grain size and (b) poly-Si with smaller grain size.

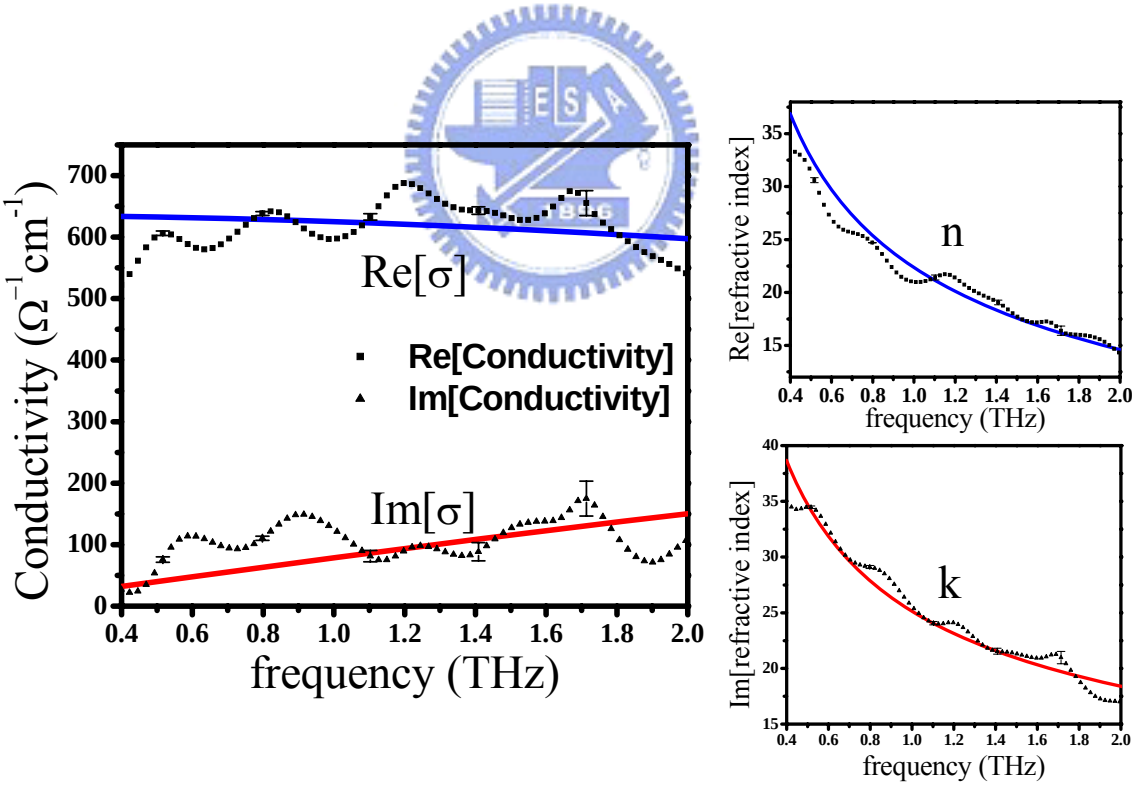

Fig. 4-12 The experimental results and fitting results of conductivity and refractive index of sample A (optical pump delay : 0 ps).

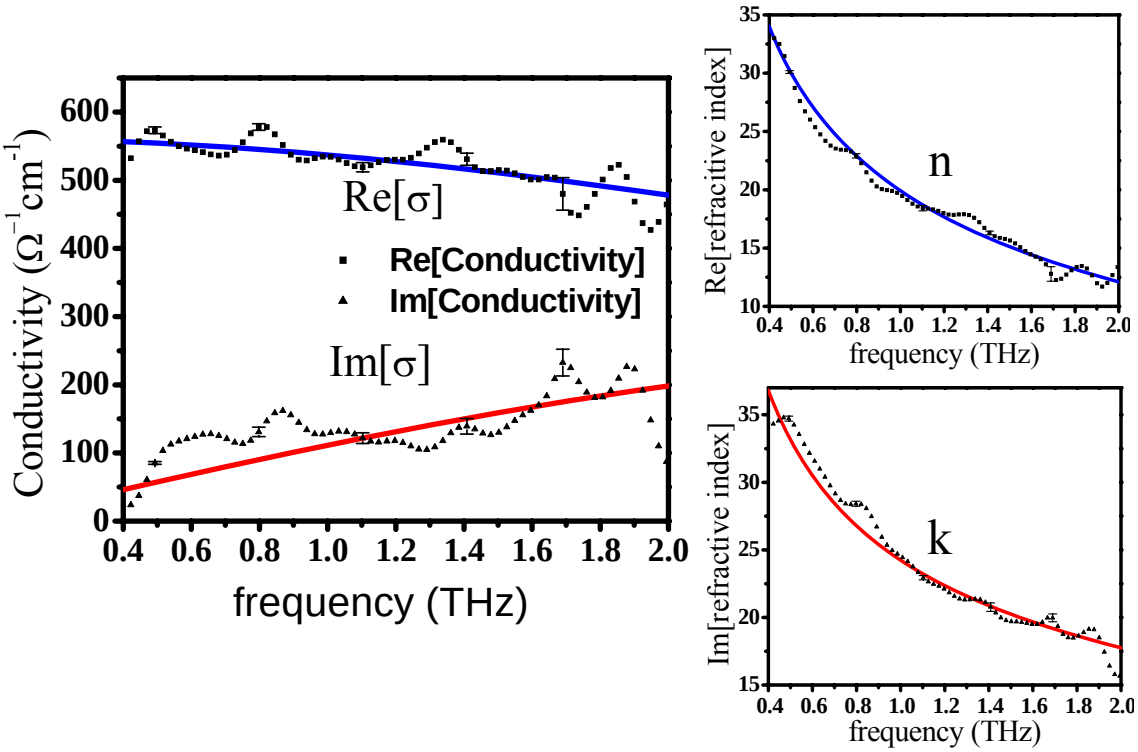

Fig.4-13 The experimental results and fitting results of conductivity and refractive index of sample A (optical pump delay : 100 ps).

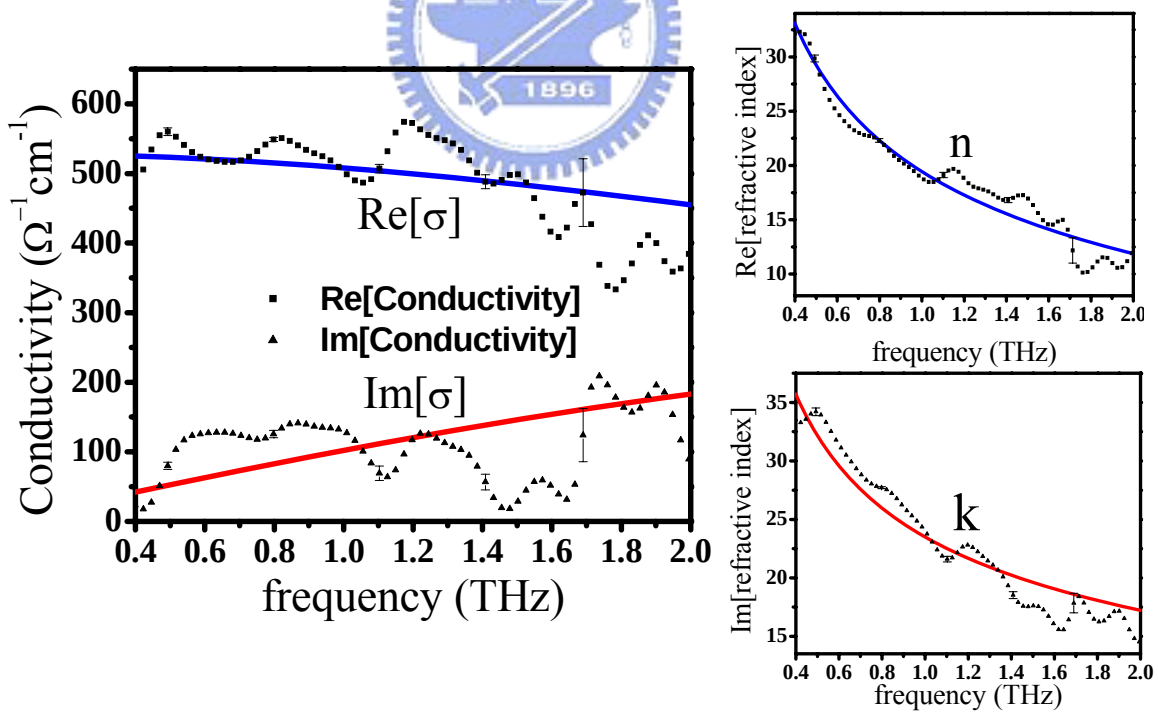

Fig.4-14 The experimental results and fitting results of conductivity and refractive index of sample A (optical pump delay : 150 ps).

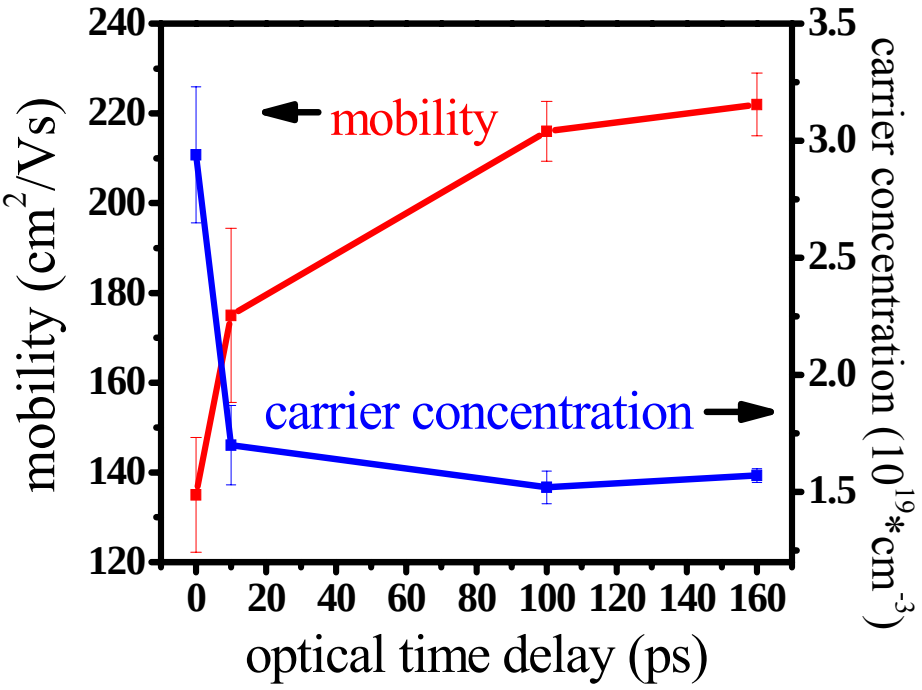

Fig.4-15 The mobility and carrier concentration variation of sample A due to the different optical pump delay.

Tables

	Small grain	Large grain
a	0.713	0.668
τ_a(ns)	92	88
τ_b(ps)	24.43	32.69

Table. 4-1 Fitting parameters of THz differential transmission curves in Fig. 4-9.

Sample	Average grain size (nm)	μ (cm^2/Vs)	Plasma frequency (10^{13} Hz)
Bulk-Si (Hall measurement)		158-299	
Bulk-Si (THz-TDS)		162±6.5	8.29±0.21
Poly-Si with large grain size (THz-TDS)	~ 500	175±19.4	7.26±0.36
Poly-Si with small grain size (THz-TDS)	~ 50	94.5±20.2	7.20±0.04
a-Si [10]		4.4±0.7	
RD-SOS [10]		44±11-383±94	
SOS [11]		240±7	
Poly-nc-Si [11]	~ 15-25	30±3	

Table. 4-2 Fitting parameters of conductivity curves in Fig. 4-10 by Drude model. For comparison, mobility of Bulk-Si is also measured by Hall measurement.

Sample A	τ_0 (fs)	μ (cm^2/Vs)	Plasma frequency (THz)	Carrier concentration (10^{19} cm^{-3})
At 0 ps	2.0±0.19	135±12.8	95.5±4.6	2.94±0.29
At 10 ps	2.6±0.28	175±19.4	72.6±3.6	1.70±0.17
At 100 ps	3.2±0.10	216±6.70	68.7±1.0	1.52±0.07
At 160 ps	3.3±0.10	222±7.00	69.7±0.8	1.57±0.03

Table. 4-3 The fitting parameters of conductivity curves from Fig. 4-11 to 4-14 by Drude model.

Chapter 5

Summary and Conclusions

In this thesis, a novel FLA process applied on recrystallization, dopant profile engineering and fabrication of TFTs has been studied. In order to identify the grain quality of FLA-processed poly-Si, we use time-resolved THz spectroscopy to verify the poly-Si with different grain size.

In Chapter 2, FLA assisted by line-scanning of laser strip spot efficiently crystallizes a-Si films with large average grains of 800 nm, using laser fluence as low as ~45 mJ/cm^2, and low number of laser shots (20 shots). Moreover, FLA exhibit a significant operating window for laser-fluence (45-60 mJ/cm^2, or, equivalently, ~30% variations), which makes it possible to implement suggested method in TFT fabrication. The FLA-annealed poly-Si channels exhibit low tail-state, deep-state, and midgap-state densities of grain traps of ~1×10^{21}, ~5×10^{18}, and ~9×10^{17} eV^{-1}cm^{-3}. The process window for annealing laser fluences, 37-50 mJ/cm^2, was confirmed by examining the changes in electrical parameters for transistors with various channel dimensions.

In Chapter 3, FLA was also employed for activation of P - and B -implanted silicon with negligible dopant diffusion. We find dopant profiles in FLA-activated samples essentially duplicate those of as-implanted ones even for junctions as deep as 100 nm below the surface. The measured sheet resistances were lower than 400 Ω/□ and the activation efficiencies of P- and B-implanted samples are 28-35 % respectively. The shallow activated-depth feature associated with FLA reduces the separation between end-of-range defects and high-concentration portion of dopants. This generates a steep interstitial gradient responsible for observed B and P uphill diffusion at a depth of about 60 nm below the surface.

Excellent dopant profile controlling of n-type and p-type dopants on Ge substrate by FLA is also demonstrated in this chapter. Shallow junction formation (17, 40 nm) and high mobility (425, 1410 cm^2/Vs) of BF_2- and P-implanted samples are both reached by activated with appropriate laser fluence and laser pulses.

In Chapter 4, we use OPTP technique to measure photoexcited carrier relaxation time and mobility of poly-Si. The complex conductivity and refractive index of poly-Si are measured by THZ-TDS in the frequency range from 0.4 to 2 THz. Poly-Si with different grain sizes was distinguished by OPTP and their transient mobilities are obtained by fitting the experimental results of THz-TDS to the Drude model. The larger mobility of large-grain size poly-Si is concluded to be corresponding with the reduction of deep state density due to improvement of crystalline quality after FLA. Besides, THz-TDS shows a highly potential for future application on TFT production for grain size and mobility diagnostics with non-contact and undamage to the sample.

The study of FLA is not finished in this thesis. Especially, the mechanism of femtosecond laser annealing requires further study. The sub-picosecond annealing process requires a real-time measurement, which could be powerful in the study of annealing mechanism. However, traditional SEM cannot work for the real time measurement because of its limitation from the electron source. If the electron source could be replaced by photoelectron pulses generated by ultrashort laser pulses, it will be able to study the changes of the structure during FLA process by electron microscopy. The sub-picosecond annealing process could thus be realized.

Recently, applying femtosecond laser pulses to the cathode to generate short pulses of photoelectrons has been published. The combination of the high spatial resolution and temporal resolution turns SEM to a powerful technique for the study of nonequilibrium dynamics. This technique has been used to study the nonequilibrium phase transitions in cuprates and nonequilibrium dynamics of nanometer-scale structures. By measuring the

sample with ultrafast electron microscopy, Bragg Spot evolution and lattice change with time are able to be analyzed. Herein, we would like to apply this technique on the study of recrystallization process in FLA. The excitation pulse will be used to anneal amorphous silicon. A small transition stage will be installed in the chamber for the purpose of sample-scanning. The scanning speed will be controlled by computer to correspond to appropriate inter-pulse overlapping. Then, we can obtain the diffraction image of annealing process at different time delay by this time-resolved measurement and therefore the mechanism of recrystallization in FLA could be studied. By repeat our previous work of FLA on a-Si in this setup, we will be able to clarify the influence of annealing parameters (laser fluence, irradiated laser shots and substrate temperature) to the grain growth of poly-Si. In the future, we might be able to apply these results on the improvement of grain quality in FLA.